Stapp Car Crash Journal, Vol. 68, pp. 104-154

Comparison of Bending Properties in Paired Human Ribs with and without Costal Cartilage

Rose Schaffer[1], Yun-Seok Kang[1], Angelo Marcallini Jr[1], Bengt Pipkorn[2], John H Bolte IV[1], Amanda M Agnew[1]

[1]Injury Biomechanics Research Center, The Ohio State University, USA

[2]Autoliv Research, Sweden

ABSTRACT – Thoracic injuries, most frequently rib fractures, commonly occur in motor vehicle crashes. With an increased reliance on human body models (HBMs) for injury prediction in various crash scenarios, all thoracic tissues and structures require more comprehensive evaluation for improvement of HBMs. The objective of this study was to quantify the contribution of costal cartilage to whole rib bending properties in physical experiments. Fifteen bilateral pairs of 5th human ribs were included in this study. One rib within each pair was tested without costal cartilage while the other rib was tested with costal cartilage. All ribs were subjected to simplified A-P loading at 2 m/s until failure to simulate a frontal thoracic impact. Results indicated a statistically significant difference in force, structural stiffness, and yield strain between ribs with and without costal cartilage. On average, ribs with costal cartilage experienced a lower force but greater displacement with a longer time to fracture compared to isolated ribs. Comparisons were complicated by varying levels of calcification between costal cartilages and varying geometry with the inclusion of the costal cartilage. This study highlights the important effects of costal cartilage on rib properties and suggests an increased focus on costal cartilage in HBMs in future work.

KEYWORDS – costal cartilage, frontal impact, thorax, rib fracture

INTRODUCTION

Injuries from motor vehicle crashes (MVCs) remain common despite continual advances in safety regulations and technology. Globally, 1.19 million people are killed in MVCs every year (WHO, 2023). The thorax, the critical region protecting internal organs such as the heart and lungs, is the most commonly injured body region in frontal crashes, even with modern protective equipment in vehicles (Brumbelow and Zuby 2009). This is often due to the high magnitudes and rate of loads placed on the thorax during frontal crashes (Lien *et al.* 2009; Pattimore *et al.* 1992). Among thoracic injures, rib fractures are the most common and are often indicators of overall trauma because of the associated increase in mortality and morbidity rates due to intrathoracic injuries (Ekambaram *et al.* 2019; Kent *et al.* 2008; Lee *et al.* 2015). Both rib fractures and costal cartilage fractures are common in high-energy blunt impacts like car crashes, and multiple rib fractures often occur simultaneously with costal cartilage fractures (Nummela *et al.* 2018).

Costal cartilage (CC) is an integral part of the thoracic skeleton and provides a flexible interface between the bony ribs and sternum. The costal cartilage attaches ribs 1-7 directly to the sternum while the costal cartilage for ribs 8-10 indirectly attaches to the sternum via the seventh rib's costal cartilage. Costal cartilage is made up of an inner solid of hyaline cartilage that is surrounded by a layer of connective tissue called the perichondrium (Zeng *et al.* 2021). The costal cartilage itself is composed of chondrocytes and the extracellular matrix, which is mainly composed of water, collagen fibers, and proteoglycans (Weber *et al.* 2021). The ribs and costal cartilage comprise an

Address correspondence to: **Amanda Agnew, PhD**
The Ohio State University, 333 W 10th Ave, Columbus, OH 43210
E-mail: amanda.agnew@osumc.edu

important anatomical functional unit for both ventilation and protection of the thorax, and therefore it is important to study their properties.

Common testing on costal cartilage includes indentation and coupon testing to calculate material properties. Lau *et al.* (2008) and Forman and Kent (2011; 2014) performed indentation testing to identify the stiffness of ageing costal cartilage with varying results on the effect of age. Indentation testing was also used to determine the elastic modulus for costal cartilage, ranging from 8.7 to 12.6 MPa (Forman and Kent 2011). Guo *et al.* (2007) investigated age and sex related biomechanical properties using coupon tensile testing and found that children had higher tensile strength than adults. Albert and colleagues (personal communication) are currently undertaking a large study to explore the effects of age, sex, loading rate, strain mode, and presence of the perichondrium on costal cartilage material properties. While these studies investigated the material properties of costal cartilage, it is unknown how the variance in costal cartilage material affects properties of the thorax.

A few studies investigated mechanical properties of costal cartilage using various loading scenarios. Cantilever bending (Forman *et al.* 2010; Forman and Kent 2011, 2014) and bending, tension, and torsion tests (Gradischar *et al.* 2022) were performed on post-mortem human subject (PMHS) costal cartilage units. Roy *et al.* (2004) tested porcine costal cartilage segments in three-point bending to find the elastic modulus (7.06 MPa) and Kohles (2021) conducted similar tests to identify the tensile elastic moduli (6.13 MPa). However, these three-point bending tests did not involve testing the costal cartilage and rib unit and only included the isolated costal cartilage. Similarly, many studies have quantified mechanical properties of isolated ribs without the costal cartilage. Charpail *et al.* (2005) presented a novel test methodology that performed dynamic structural tests on intact, isolated ribs and reported force and displacement at failure. They found that rib geometry affected structural properties, and that mineral linear density correlated well with rib stiffness. Using the same methodology, Kindig *et al.* (2011) examined the mechanical loading of the entire rib, examining a greater number of rib levels than Charpail *et al.* (2005) and included the strain-time history behavior of all ribs. Agnew *et al.* (2018) included geometric variables to explore the variation in rib structural properties, also using the methodology by Charpail *et al.* (2005) and Kindig *et al.* (2011) but on a much larger dataset.

Testing on the anatomical functional unit of the ribs and costal cartilage have been rare. Kindig *et al.* (2010) loaded individual "rib rings" that consisted of the left and right ribs, their associated costal cartilages, a section of sternum, and the fixed vertebral body. The in-situ rib ring was supported by a bottom plate while a second plate applied a displacement directly into the section of sternum. They established that rib rings were generally less stiff compared to the intact ribcage and that the stiffness decreased with increasing rib number. Evaluating the biomechanical response of the thorax is common, yet it is rarer to find studies explore the properties of only the rib cage to understand contributions of rib and costal cartilage. Vezin and Berthet (2009) conducted tests on PMHS rib cages to study the deformation of the whole rib cage during dynamic loading but focused mostly on rib rotation and costovertebral joint kinematics without specific reference to the role of costal cartilage in their findings. Some studies on the rib cage have tried to determine its contribution to the stability of the thoracic spine (Brasiliense *et al.* 2011; Sis *et al.* 2016; Mannen *et al.* 2018) while other studies have quantified differences in global responses between different thoracic tissue states (Kent 2008; Murach *et al*. 2018). Although these previous studies were important to explore the effect of the superficial tissue and viscera on the response of the thorax, they did not identify the role of the costal cartilage, specifically. No experiments have yet been performed on the anatomical functional unit of only the ribs and the costal cartilage.

Current injury prevention tools, anthropomorphic test devices (ATDs) and human body models (HBMs), often do not specifically consider the unique structural contributions of costal cartilage to thoracic injury risk (Forman and Kent 2014). The current frontal ATDs do not include costal cartilage and have a limited number of steel ribs for the thorax (Humanetics 2024). Numerous approaches for how to model the costal cartilage in HBMs have been suggested. Costal cartilage has been modeled as elastic shells and solids (Zeng *et al.* 2021), as isotropic, homogenous linear elastic material (Pipkorn and Kent 2011), and as isotropic, homogenous, linear pseudo-elastic material (Forman and Kent 2011). Also, the range of costal cartilage modulus varies greatly in whole-body models (Forman and Kent 2011). These differences could affect the thoracic responses and injury prediction capabilities of HBMs. Even without these unknowns, costal cartilage has been found to affect the loading of the rib cage. Larsson *et al.* (2023) found that the costal cartilage contributed to load distribution among the individual ribs in the SAFER HBM (Pipkorn *et al.* 2023). Similarly, Murakami *et al.* (2006) established that the lower costal cartilage sustained most of the load when induced via diagonal belts. There remains a need to tease out the specific

effects of costal cartilage in order to improve HBMs, in particular, especially as vehicle safety ratings increasingly rely on HBMs in their programs. For example, Euro NCAP (European New Car Assessment Program) will incorporate virtual testing with rib fracture assessments by 2030 (Euro NCAP 2022). Therefore, understanding the contribution of costal cartilage to rib properties is critical and was the focus of this study.

METHODS

General Approach

Tissue specimens were ethically obtained from anatomical donors through The Ohio State University Body Donation Program and Lifeline of Ohio. All isolated ribs or ribs with costal cartilage were treated identically; wrapped in normal saline soaked gauze and frozen at -20°C until testing. Each specimen was dynamically impacted at 2 m/s in a 2D simplified anterior-posterior bending scenario to mimic that of a frontal thoracic impact (Agnew *et al.* 2018). Ribs were cleaned of external soft tissue including careful removal of the periosteum where strain gages were applied. In ribs with costal cartilage, the perichondrium was intentionally left intact on the costal cartilage and across the costochondral junction as the perichondrium is known to contribute to structural stiffness (Forman *et al.* 2010). The vertebral and sternal ends were potted (referred to as a "pot") in Bondo Body Filler (Bondo Corporation, Atlanta, GA). Uniaxial strain gages (CEA-06-062UW-350, Vishay Micro-Measurement, Shelton, CT, USA) were placed on the periosteal surface of the cutaneous and pleural cortices of the rib at 30% and 60% of the rib's total curve length relative to the vertebral end (Figures 1-2). Strain gages measured strain throughout the event and were used to determine fracture timing. After placing the rib in the test fixture (Figures 3-4), points were drawn on the rib for subsequent video analysis. A 6-axis load cell (Humanetics, CRABI neck load cell, IF-954, Plymouth, MI) positioned behind the vertebral end of the rib and a linear potentiometer (AMETEK, Rayelco P-20A, Berwyn, PA) attached to the sternal end of the rib measured force and displacement, respectively, in the primary loading direction (-X). Pot rotation was measured using rotational potentiometers (Servo Instrument Co, Model # 14CB1, Baraboo, WI) at the center of vertebral and sternal pots (Figure 3).

Trial Outcomes

Eight preliminary trials were conducted to explore ideal boundary conditions for inclusion of costal cartilage in this test series (Table 1, Table A1). The first trial was conducted on one rib with costal cartilage (rib+CC) to mimic exactly the boundary conditions established in Agnew *et al.* (2018) in which both ends of the rib were allowed to freely rotate. In this trial, the costal cartilage exhibited extremely ductile behavior, bent immediately, and interacted with the fixture at the sternal end. Because of this excessive early cartilage bending, the sternal rib end at the costochondral joint (CCJ) continued to be loaded until the bone subsequently failed (see Figure A1). Both the F-D diagram and the strain time histories showed two distinct responses: 1) the costal cartilage prematurely bending and then being loaded unnaturally against the fixture, and 2) the bony rib being loaded (Figure A2). In this first trial, the sternal pot rotation steadily increased until the costal cartilage hit the fixture (38 ms) and then held constant as it was unable to continue rotating. At this time, the vertebral pot began to rotate, and the rib bent until ultimate failure. This preliminary test of the rib plus costal cartilage created a response dissimilar to those isolated rib tests reported in Agnew *et al.* (2018) and Kang *et al.* (2021). Therefore, an additional five rib+CC tests were conducted (Table 1, Table A1) where the sternal end was constrained from rotation about the z-axis utilizing 3D printed PLA filament wedges (Dremel, Racine, WI) (Figure 4). This approach was devised to ensure more realistic bending of the entire unit and to establish that the test setup was repeatable and comparable between ribs with and without costal cartilage. F-D responses from these tests (Figure A3) were similar to standard rib only tests with no constraint on the sternal pot (see Agnew *et al.* 2018 and Kang *et al.* 2021), and the test setup was deemed repeatable and comparable. Since these responded similarly to the ribs without costal cartilage, two additional ribs without costal cartilage were tested to explore the possibility of restricting the sternal pot from rotating for direct comparison with the rib+CCs. Both ribs fractured early in the event on the pleural surface precisely at the sternal pot because of the added localized stress due to the rotational constraint on the sternal pot. This was unlike previous testing of ribs which generally displayed bending behavior and then fractured anterolaterally (Agnew *et al.* 2018). The F-D diagram of these two ribs shows erratic behavior until ultimate failure (Figures A4-A5) when compared to the typical responses shown in Kang *et al.* (2021). Based on the results from all eight preliminary tests (Table 1, Table A1), it was determined to conduct matched pair testing of isolated ribs without costal cartilage with no sternal rotational constraint and ribs with costal cartilage (rib+CC) with the sternal rotational constraint.

Table 1. Rib Trial Test Matrix

Test ID	Component	Boundary Condition	Outcome: Reason
Hrb469	Rib+CC	Baseline (sternal rotation allowed)	Failure: CC behavior unrealistic
Hrb511	Rib+CC	Sternal rotation constrained	Success: Rib+CC behavior realistic
Hrb512			
Hrb513			
Hrb514			
Hrb515			
Hrb516	Rib	Sternal rotation constrained	Failure: Rib behavior unrealistic
Hrb517			

Primary Sample

After all trials in which the boundary conditions were finalized, the primary sample for this study was selected to include 15 bilateral pairs of 5th ribs. Fifth ribs represent mid-thoracic ribs with a direct connection to the sternum (*i.e.,* "true" ribs) with a relatively large amount of costal cartilage present for evaluation, which is generally straighter than lower true ribs, so were deemed ideal for this study. Ribs were chosen from individuals spanning the adult age spectrum (30 – 96 years) and such that males and females were matched within age decades when possible (Table 2). Pairs were ordered with the youngest individual in Pair 1 and the oldest in Pair 15 to allow for observations of potential age trends.

Table 2. Demographics for Rib Pairs

Pair ID	Age (yrs)	Sex	Height (cm)	Weight (kg)
1	30	M	172.7	83.5
2	54	F	162.6	76.2
3	54	F	163.0	93.0
4	55	M	182.9	85.7
5	57	F	174.0	87.5
6	59	M	185.4	72.6
7	60	M	186.7	88.5
8	61	M	176.5	60.1
9	67	F	165.1	64.4
10	71	F	144.8	79.8
11	72	M	177.8	62.4
12	81	M	175.3	69.2
13	83	F	165.1	95.5
14	96	M	172.7	72.4
15	96	F	158.8	40.1

Primary Data Collection and Analysis

The left rib within each pair was isolated (*i.e.,* "rib" only), while the right side consisted of the rib with intact costal cartilage ("rib+CC") with the assumption that structural behavior would be similar between the left and right ribs (Yoganandan and Pintar 1998). The same boundary conditions that were determined from the preliminary trials were used for the ribs and rib+CC. Specifically, in all tests, the vertebral end (*i.e.,* rib head) was free to rotate about the z-axis (see Figure 3), but in the rib+CC tests the sternal pot was constrained to not allow rotation. Rotation was calculated as the difference between the initial and end angle (*i.e.,* at fracture) for each vertebral and sternal pot. A positive rotation indicated the pot rotated clockwise and a negative rotation indicated the pot rotated counterclockwise (Figures 1-2). All force, displacement, and rotational data were filtered using Channel Frequency Class (CFC) 180 (SAE 2007, J211) while the strain were unfiltered. Structural stiffness (K) was calculated as the slope of the linear portion of the force-displacement curve, and yield point was generally determined as the intersection of the F-D curve with a 0.1% displacement offset line from the same portion of the curve. All data treatment, calculation of structural properties, as well as the rib span length and the rib height (Y-distance) in the test fixture (Figures 1-2) were consistent with Agnew *et al.* (2018).

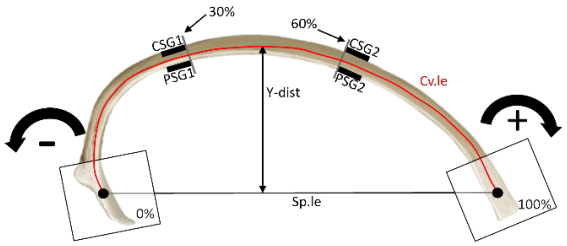

Figure 1. Diagram of potted rib illustrating the baseline preparation

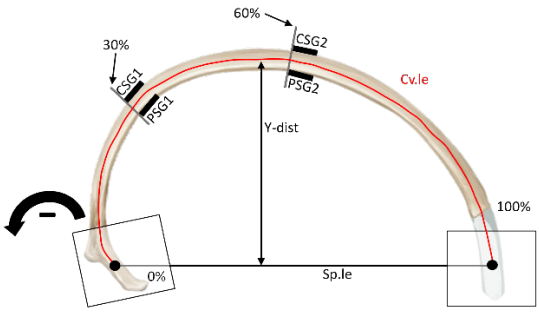

Figure 2. Diagram of potted rib+CC illustrating the altered preparation and constrained sternal pot

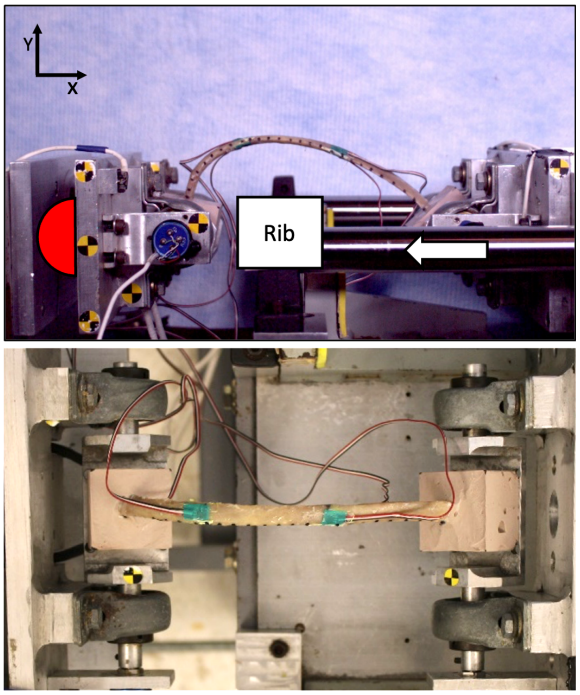

Figure 3. Exemplar test set-up for "rib" only condition (Pair 10) showing left rib position at time zero (top) and initial position of sternal pot from an overhead view (bottom). Load cell indicated by red half circle.

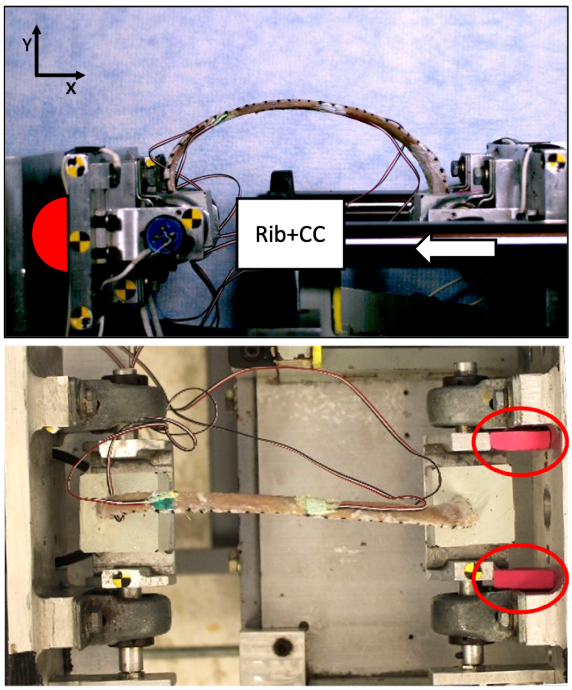

Figure 4. Exemplar test set-up for "rib+CC" condition (Pair 10) showing right rib position at time zero (top) and initial position of sternal pot from an overhead view with wedges (circled) inserted to restrict rotation (bottom). Load cell indicated by red half circle.

After testing, standard radiographs were taken with an inferior to superior projection (50–55 kVp, 2–5 mAs) to categorize costal cartilage calcification as none, minimal, moderate (medium), or maximal as defined by Michelson (1934) and Barchilon *et al.* (1996). Fracture locations were measured as a percentage of the total rib curve length from the head to the sternal rib end and were categorized by general anatomical location: posterior (0 – 29.9 %), middle (30 – 70.9 %), or anterior (71 – 100 %) (Agnew *et al.* 2018), excluding the costal cartilage to ensure direct comparability between ribs and rib+CCs. The lengths of costal cartilages were also measured and are included in Table B1.

For comparisons of properties between rib without costal cartilage, "rib", and rib with costal cartilage, "rib+CC", percent differences were calculated as:

$$\%\,Diff = \frac{'Rib' - 'Rib+CC'}{0.5 \times ('Rib' + 'Rib+CC')} \times 100 \qquad \text{[Eq. 1]}$$

Since most data were not normally distributed, Mann-Whitney (MW) tests were used to assess differences in medians between each testing condition group, while Wilcoxon Signed Rank (WSR) tests were used to assess the differences in medians of rib properties within each rib pair (*i.e.,* rib versus rib+CC). Statistical tests were conducted in JMP v16, and an alpha level was set *a priori* to 0.05 to establish statistical significance.

RESULTS

Images of all 15 pairs of ribs with and without costal cartilage at time 0 and at time of fracture are shown in Figs. B1-B15 for visual comparison. Number and location of fractures were compared between ribs and rib+CCs (Table B1). No significant differences were identified in number of fractures within pairs (Marginal Homogeneity test, p=0.48). Of the 15 pairs, 11 (73%) had at least one fracture occur in both ribs of the pair in the same anatomical region (Fig. 5). Alternatively, 9 of 15 pairs (60%) had at least one fracture occur in both ribs in different regions. Isolated ribs (4/15) were more likely to have more than one fracture than ribs with costal cartilage (3/15), however if also considering fractures to the costal cartilage, multiple fractures were more common in ribs with costal cartilage (6/15). Of the ribs tested with costal cartilage, four experienced a fracture in the costal cartilage, and one failed at the costochondral junction (CCJ). All fractures either occurred in the middle or anterior regions. Fractures in the middle (25) were most common compared to fractures in the anterior region (13).

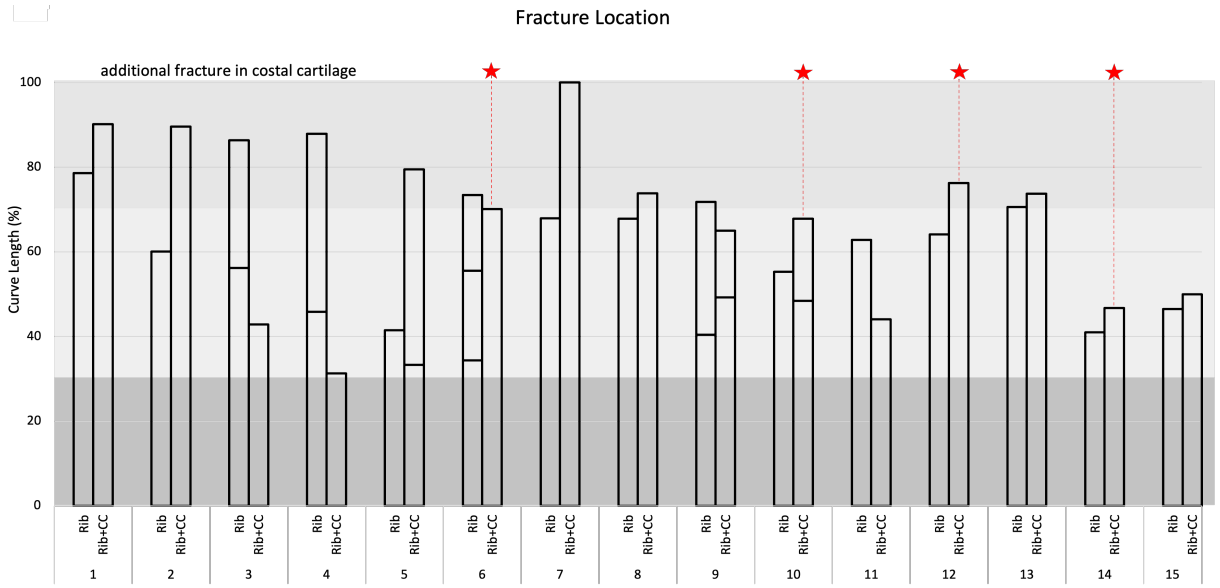

Figure 5. Number and location of fractures along the length of the rib within rib pairs. 0% = vertebral end, 100% = sternal end. Dark gray = Posterior (0-30%), light gray = Middle (31-70%), medium gray = Anterior (71-100%). Red stars indicate additional fractures in the costal cartilage.

Structural property calculations for each rib are included in Table C1 and descriptive statistics with statistical comparisons between test conditions are presented in Table 3. On average, ribs with costal cartilage fractured later (mean of 34.3 ms) than ribs without costal cartilage (mean of 31.6 ms), although this difference is not statistically significant (Figure 6). This increased duration in rib+CC tests compared to ribs occurred in 10/15 pairs (67%). Similarly, in 10/15 pairs (67%), ribs with costal cartilage displaced more before fracturing (mean of 23.7%) than isolated ribs (mean of 21.1%) (Figure 7), though also not statistically significant. In contrast, in 12/15 pairs (80%), isolated ribs experienced a greater peak force than ribs with costal cartilage, and 11/15 (73%) pairs had greater yield force in the isolated ribs compared to rib+CCs. Isolated ribs had a significantly greater peak force (median of 51.1 N) and yield force (median of 38.4 N) than those with costal cartilage (medians of 47.2 N and 27.2 N, respectively) ($p<0.015$) (Figure 8). The same trend was observed for stiffness ($p=0.007$) (Figure 9). No significant differences were found for total or plastic energy between ribs and ribs with costal cartilage (Figures 10 and C17). Differences in F-D behavior within individual pairs to illustrate some of these trends are shown in Figures C1-C15.

There was no significant difference in vertebral pot rotation between rib and rib+CC (MW, $p=1.00$; WSR, $p=0.98$) suggesting similar bending behavior within rib pairs despite the sternal end being constrained (*i.e.,* no rotation allowed) for the ribs with costal cartilage (Figures D1-D15). As intended, there was a significant difference in sternal rotation between rib and rib+CC (MW $p=<0.0001$; WSR $p=<0.0001$), since the sternal pot was constrained from rotating in the rib+CC tests (Figure 11). This finding suggests the boundary conditions, while different between rib and rib+CC, imposed similar bending behavior between the specimens. Velocity time histories also show the repeatability of the input, regardless of the sternal constraint (Figure C16).

Descriptive statistics and comparisons of yield and peak strains between rib conditions are included in Table 4, yield and peak strain calculations are included in Table E1, and strain time histories for all ribs and rib+CCs are shown in Figures E1-E15. Gages that broke during the test were excluded from analysis. Notably, this includes multiple gages from Pair 6: CSG1 and CSG2 from the rib test and CSG2 for the rib+CC test (see missing data in Figures 12-13). In general, ribs with costal cartilage experienced lower peak and yield strain compared to the ribs without costal cartilage for all strain gages (CSG1, PSG1, CSG2, and PSG2) (Figures 12-13). However, these paired differences were only significant for CSG2 and PSG2 yield strain ($p=0.025$ and $p=0.003$, respectively). Figures 12 and 13 show the peak strain magnitudes of CSG1/PSG1 and CSG2/PSG2 and an exemplar time history of strain within a pair and illustrates the extended time to fracture in the rib+CC compared to the rib.

For the ribs with costal cartilage, calcification of the costal cartilage was classified based on post-test x-rays (Figures F1-F15, Table B1). Four ribs with costal cartilage were classified as having no calcification, five had minimal calcification, one had medium calcification, and five ribs had maximal calcification. There appeared to be no trend of increasing calcification with age in this sample.

Table 3. Structural Property Summary and Comparisons

Property	Rib Condition	Mean (SD)	Mean % Diff	Median	Mann-Whitney p-value	Wilcoxon p-value
Time of Fracture (ms)	Rib	31.6 (11.0)	-8.3	31.1	0.237	0.182
	Rib+CC	34.3 (9.3)		34.2		
Time at Yield (ms)	Rib	21.9 (4.1)	4.4	22.1	0.407	0.670
	Rib+CC	21.0 (5.4)		20.5		
Stiffness (N/mm)	Rib	1.99 (1.3)	28.2	1.54	0.407	**0.010**
	Rib+CC	1.50 (0.7)		1.38		
Peak Force (N)	Rib	65.0 (39.1)	22.7	51.1	0.361	**0.016**
	Rib+CC	51.7 (27.5)		47.2		
Yield Force (N)	Rib	43.7 (20.0)	36.6	38.4	**0.046**	**0.018**
	Rib+CC	30.2 (17.8)		27.2		
Displacement (%)	Rib	21.1 (8.5)	-11.7	20.3	0.384	0.222
	Rib+CC	23.7 (8.2)		23.2		
Yield Displacement (%)	Rib	12.5 (4.3)	10.1	13.5	0.263	0.551
	Rib+CC	11.3 (5.9)		10.3		
Total Energy (N*mm)	Rib	1967 (2180)	16.6	1101	1.000	0.798
	Rib+CC	1666 (1500)		1253		
Plastic Energy (N*mm)	Rib	1366 (2139)	7.6	515.3	0.678	0.410
	Rib+CC	1265 (1568)		769.0		
Plastic Energy (%)	Rib	41.4 (38.2)	-33.0	42.0	0.151	0.078
	Rib+CC	57.8 (40.3)		84.2		

Bold p-values = statistically significant

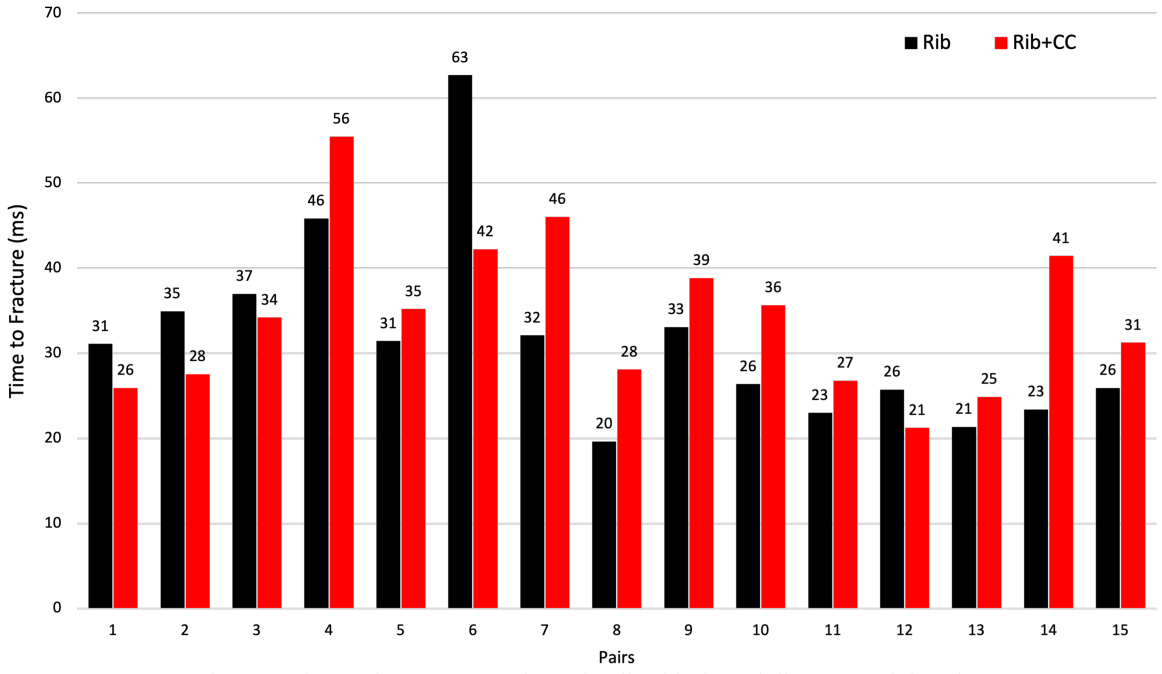

Figure 6. Time to fracture comparisons for ribs (black) and rib+CCs (red) in pairs.

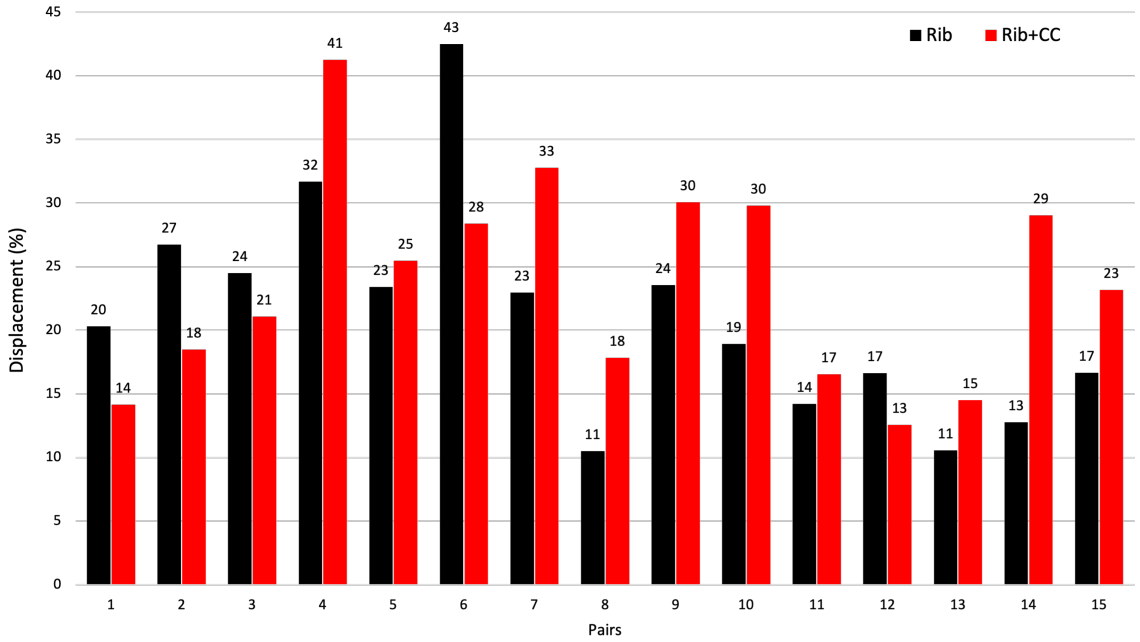

Figure 7. Displacement comparisons for ribs (black) and rib+CCs (red) in pairs.

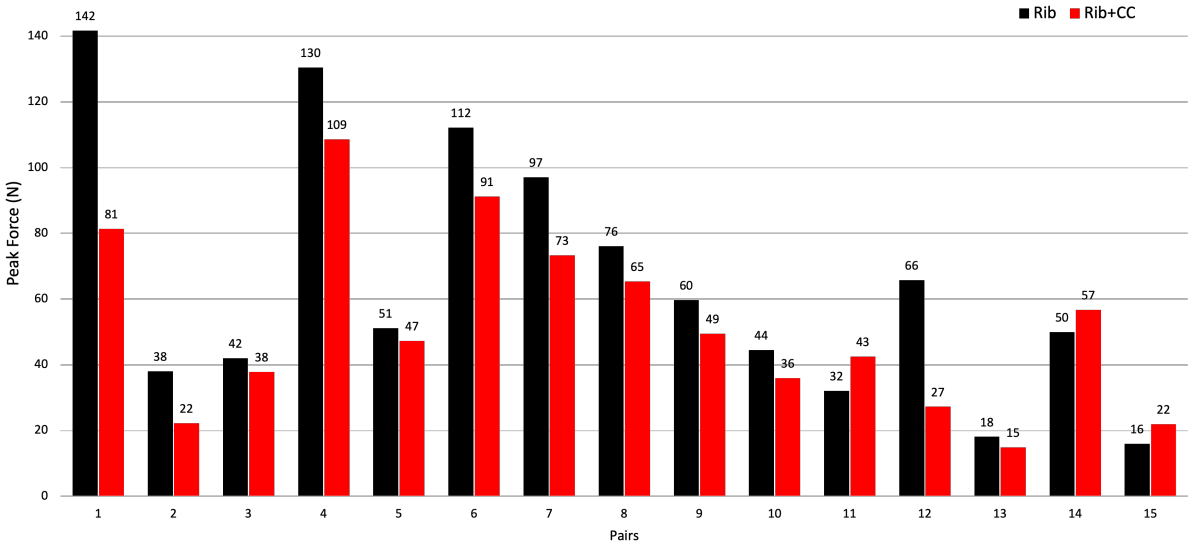

Figure 8. Peak force comparisons for ribs (black) and rib+CCs (red) in pairs.

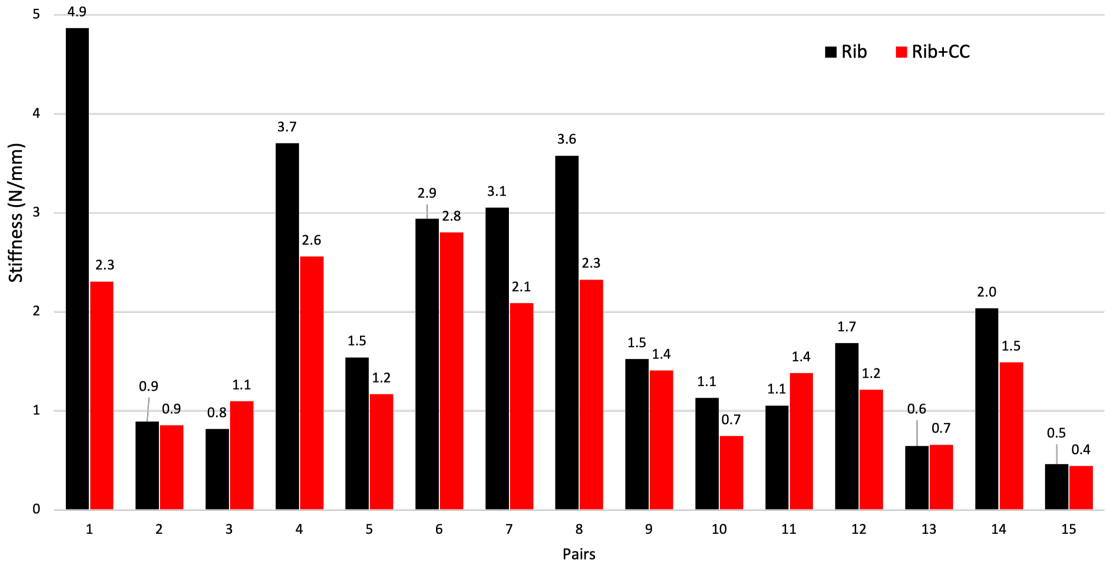

Figure 9. Stiffness comparisons for ribs (black) and rib+CCs (red) in pairs.

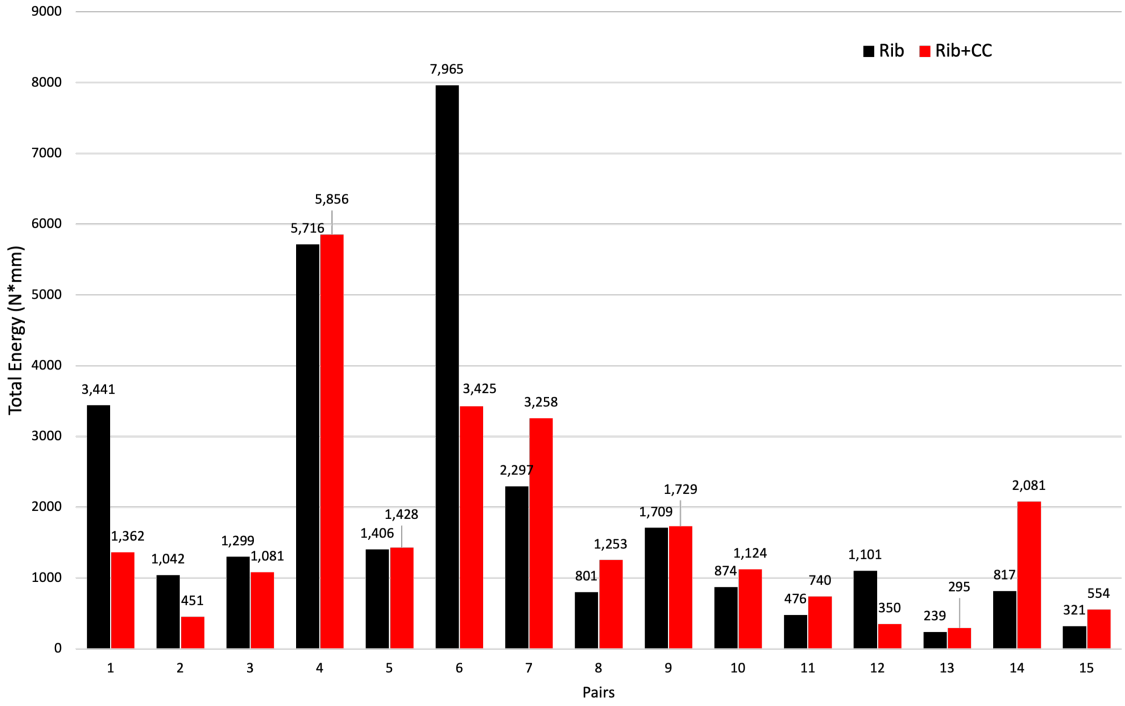

Figure 10. Total energy comparisons for ribs (black) and rib+CCs (red) in pairs.

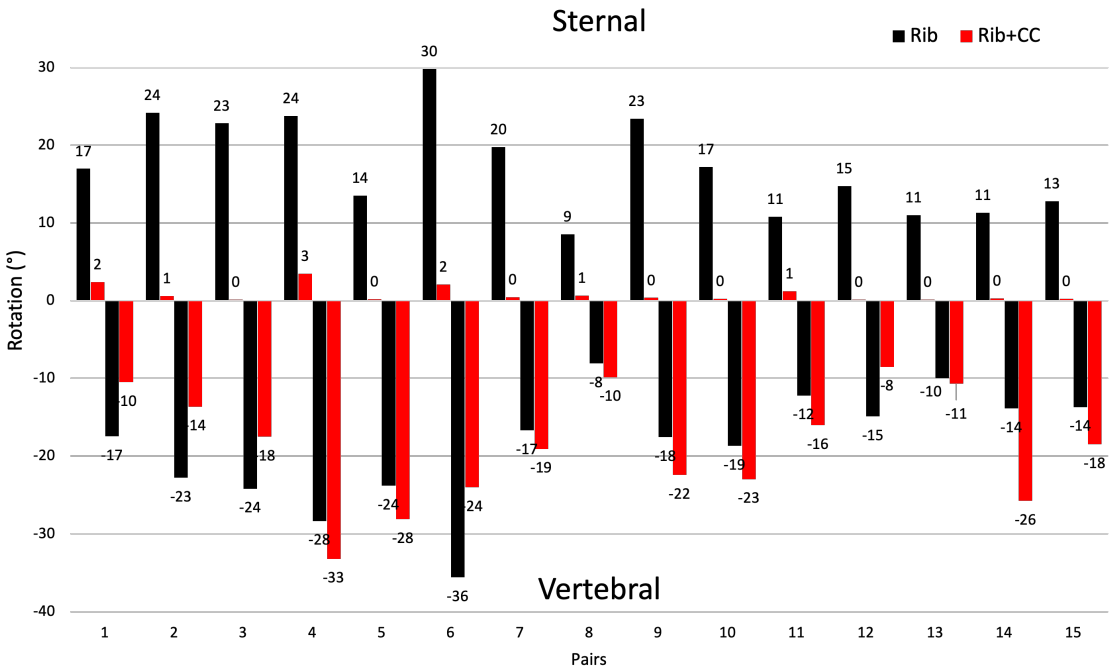

Figure 11. Rotation of vertebral and sternal pots from time zero to time of fracture for ribs (black) and rib+CCs (red) in pairs.

Table 4. Strain Data Summary and Comparisons

	Rib Condition	Mean (SD)	Mean % Diff	Median	Mann-Whitney p-value	Wilcoxon p-value
CSG1 Peak Strain (µs)	Rib	8346 (3634)	4.2	7481	0.597	0.754
	Rib+CC	8003 (4248)		7214		
CSG2 Peak Strain (µs)	Rib	9193 (3216)	7.3	8656	0.476	0.414
	Rib+CC	8543 (3463)		7556		
PSG1 Peak Strain (µs)	Rib	-8348 (3198)	8.5	-7707	0.407	0.293
	Rib+CC	-7667 (3844)		-6826		
PSG2 Peak Strain (µs)	Rib	-9193 (5051)	21.2	-9192	0.361	0.244
	Rib+CC	-7430 (3135)		-7710		
CSG1 Yield Strain (µs)	Rib	5212 (1478)	24.2	5228	0.085	0.069
	Rib+CC	4086 (2101)		3117		
CSG2 Yield Strain (µs)	Rib	5953 (2067)	32.3	5634	0.057	**0.028**
	Rib+CC	4298 (2153)		4086		
PSG1 Yield Strain (µs)	Rib	-5306 (1602)	30.6	-4989	**0.038**	0.074
	Rib+CC	-3898 (1899)		-3698		
PSG2 Yield Strain (µs)	Rib	-5829 (1912)	47.0	-5280	**0.003**	**0.006**
	Rib+CC	-3610 (1671)		-3594		

Bold p-values = statistically significant

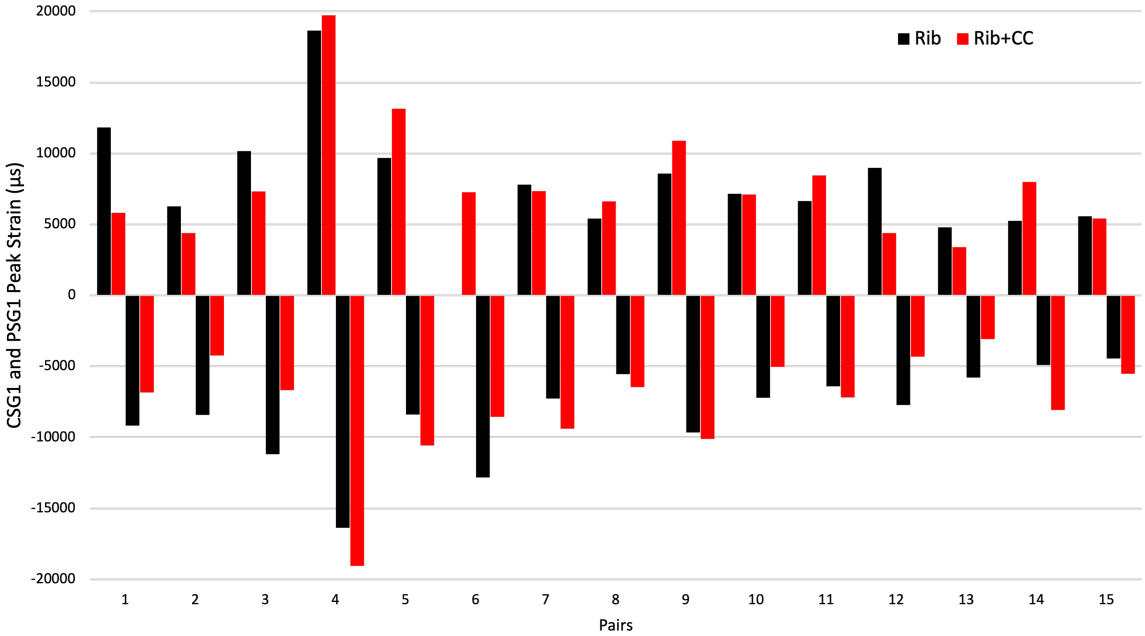

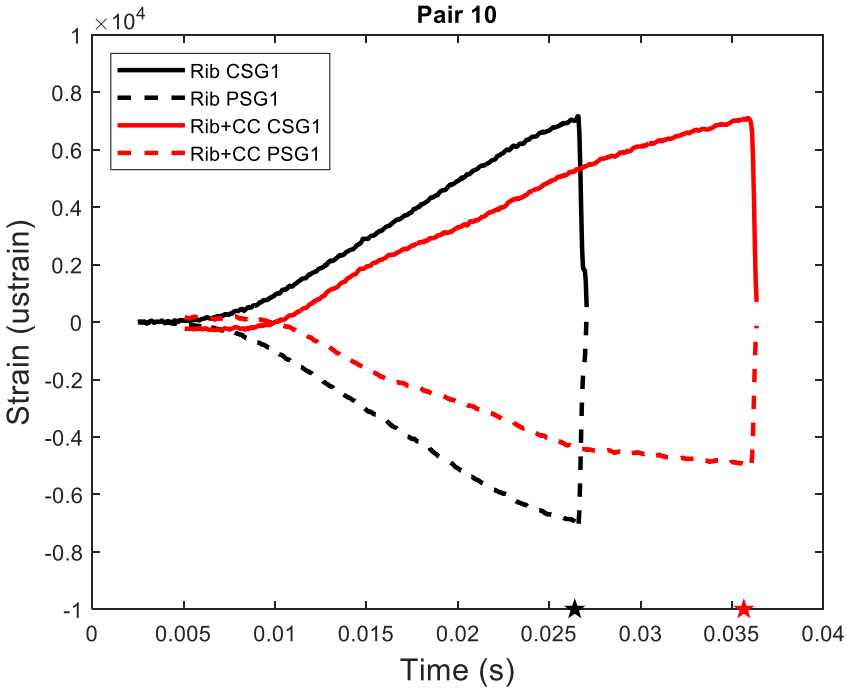

Figure 12. Peak strain magnitudes of CSG1 (positive) and PSG1 (negative) (30% site) for all pairs (top) and exemplar strain-time history plot (bottom) for the same gages. Stars indicate time of fracture for rib (black) and rib+CC (red). Note that CSG1 in Pair 6 rib is missing as it broke early during the test.

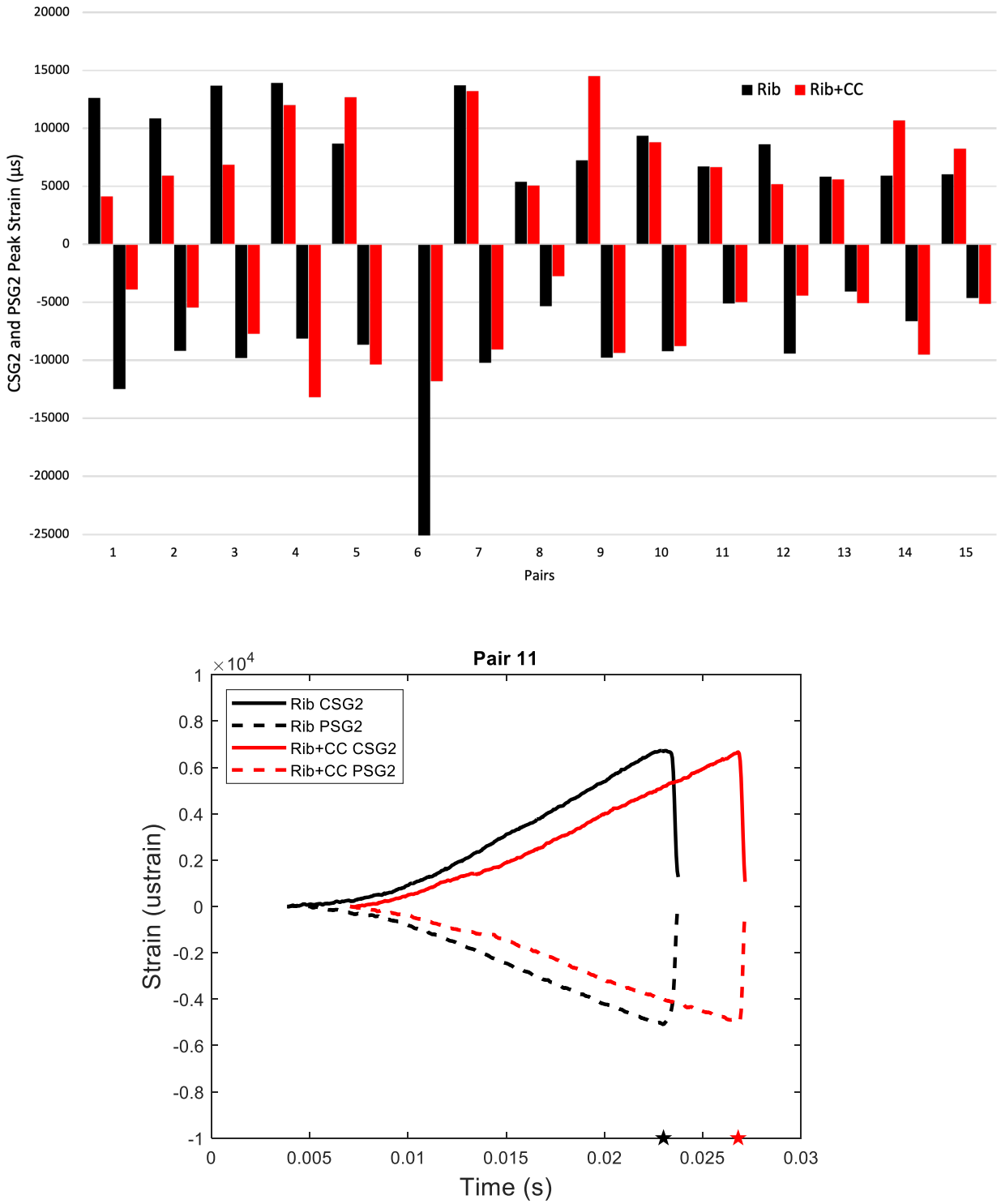

Figure 13. Peak strain magnitudes of CSG2 (positive) and PSG2 (negative) (60% site) for all pairs (top) and exemplar strain-time history plot (bottom) for the same gages. Stars indicate time of fracture for rib (black) and rib+CC (red). Note that CSG2 in Pair 6 rib and rib+CC is missing as they broke early during the test.

DISCUSSION

This study investigated the contribution of costal cartilage to the biomechanical properties of human ribs by directly comparing one isolated rib and one rib with costal cartilage intact in bilateral pairs. Costal cartilage is inherently more flexible than bone due to the vast amounts of collagen fibers in the extracellular matrix (Huwe *et al.* 2017; Lee *et al.* 2007; Stacey *et al.* 2013) and this was reflected in the response of the ribs with costal cartilage versus isolated ribs in this study.

Most bony ribs were stiffer and resisted greater loads than ribs with costal cartilage. In other words, ribs with costal cartilage, on average, were 28% less stiff and had 23% lower force than isolated ribs. Similarly, ribs with costal cartilage generally displaced further before failure (on average a 12% difference), increasing the duration of the bending event. This increase in the displacement is likely a result of the flexibility of the costal cartilage. Similarly, this ductility could also play a role in decreasing the force that the rib with costal cartilage experienced. Pair 11 was a notable exception to this trend in that the F-D curves (Figure C11) had similar shapes, but the rib+CC had a higher force and stiffness than the rib alone. This is likely because the costal cartilage in the rib+CC had maximal calcification, causing the unit to behave more like if it were all bone, but with a larger Y-distance and overall length (Cv.Le and Sp.Le) as shown in Table B1, explaining the typical greater displacement in the rib+CC in this pair. This is also the case for Pair 15.

It is possible F-D behavioral differences are due to different initial shapes and positions of the isolated ribs versus those ribs with costal cartilage. Because of the inclusion of the costal cartilage length, the rib+CCs sat higher in the fixture than the isolated ribs, i.e., had a larger Y-distance (WSR, p=0.001), as shown in Figures B1-15 and Table B1. The costal cartilage increased the height of the overall rib complex by rotating the bony portion of the rib counterclockwise in the initial position (Figure B16). If the bending behavior was then accentuated during the event, the average longer time to fracture (Figure 6) in the rib+CCs may be explained, as well as the larger normalized displacement (Figure 7). This is consistent with findings from Rampersadh *et al.* (2022) and Holcombe *et al.* (2016) in a simulation of this set-up with only isolated ribs; changing the height of the ribs influenced the force-displacement responses more than changing any other initial positioning. They found that increasing the height (Y-dist) decreased the force and increased the displacement at fracture for bony ribs (Rampersadh *et al.* 2022). In the current study, with an increased Y-distance with the addition of costal cartilage, it is unknown which of these is responsible for the generally lower force and increased displacement in the rib+CCs. Li *et al.* (2010) and Kindig (2010) imposed an offset between the sternal and vertebral ends of the rib order to account for the position of the costal cartilage but did not consider the cartilage properties in their experiments (*i.e.*, there was no cartilage with these ribs). A future study should be conducted to understand the sensitivity of rib biomechanical responses due to these positioning variables independently.

Not all pairs exhibited the same overall trend of greater displacement in the rib+CC than the rib. It is interesting to note that the exceptions to the observations were more often seen in the younger individuals in the sample. Pairs 1 (30 year-old male), 2 (54 year-old female), and 3 (54 year-old female) (Figure 7) all had the isolated rib displace further before failure than the rib+CC, also evident in the greater total energy (Figure 10) in the rib than in the rib+CC. This may be explained by an increased ductility in the bone material of these younger ribs, whereas the rest of the rib sample appears to behave more brittle. Table C1 illustrates that no "brittle" ribs were observed (*i.e.,* plastic energy = 0) in the first 7 pairs (the younger part of the sample), but are quite common in the remaining 8 pairs (the older part of the sample). Older individuals were more likely to have no plastic energy whether the rib had costal cartilage or not (Figure C17). This increasing brittleness with age aligns with previous studies on bone (Zioupos and Currey 1998). Furthermore, the calcification of costal cartilage tends to expand and increase with advancing age (Dearden *et al.* 1974, Holcombe *et al.* 2017, Semine and Damon 1975, Teale *et al.* 1989, Rejtarova *et al.* 2009, Weber *et al.* 2021) making it behave more like bone and more brittle compared to the normally flexible costal cartilage (Forman and Kent 2011; Forman and Kent 2014). Forman and Kent (2014) carried out a sensitivity analysis to study the effect of calcification on costal cartilage stiffness. They found a fourfold increase in the stiffness when changing the calcification score from zero (no calcification) to 3.5 (severe calcification).

In this study, two (Pairs 3 and 11) of the three pairs where the rib+CC had a greater stiffness than the rib had some calcification, with one (Pair 11) even having maximal calcification (Figure 9, Table B1, Figure F11). Peak force could have also been affected by calcification as three pairs (Pairs 11, 14, and 15) that had the rib+CC with a higher peak force than the rib, all three were classified with calcification (Figure 8, Table B1, Figures F11, F14, F15). Two (Pairs 11 and 15) of the three were classified with maximal calcification (Figures F11, F15). These two pairs,

which act like ribs without costal cartilage since their costal cartilage was classified as having maximal calcification. Degree of costal cartilage calcification was not entirely predictable by age in this sample (Table B1). Some "younger" individuals were maximal (*e.g.,* Pair 4, 55 years) and some older individuals had none (*e.g.,* Pair 13, 83 years) or minimal calcification (*e.g.,* Pair 14, 96 years).

Pairs 6 and 12 displayed different behavior than other pairs. The isolated rib in pair 6 had a higher force than the rib+CC and a greater displacement since it fractured later than the rib+CC. The rib+CC fractured earlier than the rib and therefore had a lower displacement than the rib as well. Upon inspection of high-speed video, the rib+CC failed first in the costal cartilage, very close to the sternal pot. This early failure point in the costal cartilage (about 10 ms before bony failure) caused a large difference in fracture timing and displacement between the rib and the rib+CC. Pair 12 also had an additional fracture in the costal cartilage for the rib+CC, but it was difficult to tell whether the costal cartilage fractured before bony failure. The early fracture time of the costal cartilage for these two pairs resulted in the isolated rib having greater time to fracture (Figure 6), displacement (Figure 7), and total energy (Figure 10) values.

On average, all four strain gages recorded a higher peak strain in the ribs without costal cartilage than ribs with costal cartilage, though differences were not statistically significant (Table 4, Figures 12-13). The same trend was observed for yield strain in the isolated ribs, although for PSG1, PSG2, and CSG2 these differences were statistically significant. It is intuitive that without the added compliance of the costal cartilage, the local displacement and strain would have been greater for isolated ribs. The positive relationship between displacement and strain can be observed in all pairs (Figures E19-E20). Iraeus *et al.* (2020) confirmed that rib arch height had an influence on the strain in a finite element model and since the Y-distance was increased in the rib+CCs, it is not surprising peak strain values were different. Furthermore, CSG2 and PSG2 had higher peak strains, on average, compared to CSG1 and PSG1, consistent with most of the fractures occurring at the middle and anterior locations of the ribs, *i.e.,* closer to CSG2 and PSG2.

There was a positive linear trend between peak strain and peak force for all 15 pairs (Figures E17-E18). Pair 1, Pair 4, and Pair 6 were common outliers in multiple strain gage locations. Pair 1 was a 30-year-old male so the higher peak force can be expected as it has been found that peak force is greatest in the young adult years (22-40 years) (Agnew *et al.* 2015, 2018). Interestingly, only the rib for pair 1 was an outlier where the rib+CC followed the trend better. The rib+CC was classified as having no calcification, so it is possible it was more ductile than the rib, explaining why the rib and the rib+CC were vastly different. Similarly, there was also a positive linear trend between peak strain and peak displacement for all 15 pairs (Figures E19-E20). The higher the peak strain, the higher the peak force and peak displacement. Similar to peak force, Pair 4 and Pair 6 are also outliers in the peak strain versus peak displacement relationship. Pair 4 was a middle adult male (55 years) that had one of the larger ribs in the sample. The rib+CC for Pair 4 was classified with having maximal calcification, so, in addition to being a middle adult male and having a larger rib, the maximal calcification could cause the costal cartilage to behave more like bone, allowing it to resist more force. Pair 6 was also a middle adult male with larger ribs able to withstand more load before eventually fracturing (Agnew *et al.* 2018). Furthermore, the larger Y-distance of these pairs suggests the rib could experience more bending and therefore more displacement and strain before failure.

Limitations

The relatively small sample size (n=15 pairs) is a limitation of this study. Further, only 5th rib pairs were investigated, and other levels could exhibit different behavior. The ribs with costal cartilage were not allowed to rotate about the z-axis at the sternal end, and the ribs without costal cartilage were allowed to rotate about the z-axis resulting in slightly different boundary conditions between comparative tests. This was necessary so the ribs with costal cartilage did not bend excessively and physically interact with the fixture at the sternal end. However, the added rotational constraint to the ribs with costal cartilage allowed ribs in both testing conditions to experience similar global bending behavior. The rib sternal pot consistently rotated clockwise while both the rib and rib+CC vertebral pots rotated counterclockwise. There was a consistent rotation of both the ribs and ribs+CC whether the sternal end was constrained or not, indicating that both the rib and the rib+CC provided consistent rotational outcomes at the vertebral end even though the sternal end was constrained for the rib+CC (see Figures D1-15). Although the boundary conditions were slightly different, the behavior of the specimens was similar and directly comparable. However, it is unknown whether this constraint influenced the outcomes in this study. Future work should consider this and build on the approach in order

to better understand the effects of costal cartilage on thoracic properties.

The amount of costal cartilage outside of the pot was not controlled for. Some ribs had more costal cartilage than others and therefore had more exposed costal cartilage between the pot and the sternal rib end. The relative length of costal cartilage could have influenced the structural properties and differences between ribs with and without costal cartilage, but it is unknown how much of a role this played in the outcomes of the study.

On average, the resulting strain rate of the ribs without costal cartilage was higher than the strain rate with costal cartilage (Figures E16) despite the same impact velocity (2 m/s). Strain gages could only be placed on the bony part of the rib and not the costal cartilage. It is possible that the costal cartilage had a higher strain rate individually compared to the bony part of the rib, but this was unable to be captured due to no strain gages being placed on the costal cartilage.

CONCLUSIONS

The objective of this study was to quantify how costal cartilage affects rib properties. Ribs with and without costal cartilage were dynamically impacted in an anterior-posterior 2D simplified bending scenario. No statistical significance was found for number of fractures between ribs with and without costal cartilage and no clear trends were identified for fracture locations within pairs. A difference in structural properties between ribs with and without costal cartilage was observed, with the ribs with costal cartilage experiencing greater displacement but lower peak force and stiffness. A difference in strain, yield strain especially, was also observed, with ribs with costal cartilage experiencing lower strain, on average, compared to ribs without costal cartilage. More work should be done in this area to further explore the effect of costal cartilage on the structural properties of the thoracic skeleton. All of these discussed differences may assist with interpretation of whole thoracic response and should be further evaluated in a broader hierarchical model similar to Murach *et al.* (2018) and Kent (2008). This research highlights the importance of the costal cartilage and shows the need to consider costal cartilage in current injury prevention techniques and safety tools (*i.e.,* HBMs).

ACKNOWLEDGMENTS

We are incredibly grateful for the anatomical tissue donors who made this research possible. This research was funded by Autoliv Research, Sweden, and all opinions are only those of the authors. Thanks to all the faculty, staff, and students of the Injury Biomechanics Research Center at The Ohio State University, especially Dr. Randee Hunter, Christopher Goden, Zachary Haverfield, Ibrahim Abuzer, and Collin Rogus.

REFERENCES

Agnew, A.M., Murach, M.M., Dominguez, V.M., Sreedhar, A., Misicka, E., Harden, A., Bolte, J.H., Stammen, J., Moorhouse, K., and Kang, Y.S. (2018) Sources of variability in structural bending response of pediatric and adult human ribs in dynamic frontal impacts. Stapp Car Crash Journal 62: 119–192.

Agnew, A.M., Schafman, M., Moorhouse, K., White, S.E., and Kang, Y.S. (2015) The effect of age on the structural properties of human ribs. Journal of the Mechanical Behavior of Biomedical Materials 41: 302-314.

Albert, D., Agnew, A.M., Kemper, A. (2024) Exploring costal cartilage material properties. *Personal communication.*

Barchilon, V., Hershkovitz, I., Rothschild, B.M., Wish-Baratz, S., Latimer, B., Jellema, L.M., Hallel, T., Arensburg, B. (1996) Factors affecting the rate and pattern of the first costal cartilage ossification. American Journal of Forensic Medicine and Pathology 17(3):239-47.

Brasiliense, L.B.C., Lazaro, B.C.R., Reyes, P.M., Dogan, S., Theodore, N., and Crawford, N.R. (2011) Biomechanical contribution of the rib cage to thoracic stability. Spine 36(26): E1686–E1693.

Brumbelow, M.L., and Zuby, D.S. (2009) Impact and injury patterns in frontal crashes of vehicles with good ratings for frontal crash protection. International Technical Conference on the Enhanced Safety of Vehicles (ESV) 21: 09-0257. Stuttgart, Germany.

Charpail, E., Trosseille, X., Petit, P., Laporte, S., Lavaste, F., and Vallancien, G. (2005) Characterization of PMHS ribs: A new test methodology. Stapp Car Crash Journal 49: 183–198

Dearden, L., Bonucci, E., and Cuicchio, M. (1974) An investigation of ageing in human costal cartilage. Cell and Tissue Research 152(3): 305–337.

Ekambaram, K., Frampton, R., and Lenard, J. (2019) Factors associated with chest injuries to front seat occupants in frontal impacts. Traffic Injury Prevention 20(S2): S37–S42.

Euro New Car Assessment Program, NCAP. (2022) Euro NCAP 2030 Roadmap. https://cdn.euroncap.com/media/74468/euro-ncap-roadmap-vision-2030.pdf

Forman, J.L., del Pozo de Dios, E., Dalmases, C.A., and Kent, R.W. (2010) The contribution of the perichondrium to the structural mechanical behavior of the costal-cartilage. Journal of Biomechanical Engineering 132(9): 094501.

Forman, J.L. and Kent, R.W. (2011) Modeling costal cartilage using local material properties with consideration for gross heterogeneities. Journal of Biomechanics 44(5): 910–916.

Forman, J.L. and Kent, R.W. (2014) The effect of calcification on the structural mechanics of the costal cartilage. Computer Methods in Biomechanics and Biomedical Engineering 17(2): 94–107.

Gradischar, A., Lebschy, C., Krach, W., Krall, M., Fediuk, M., Gieringer, A., Smolle-Jüttner, F., Hammer, N., Beyer, B., Smolle, J., and Schäfer, U. (2022) Measurement of global mechanical properties of human thorax costal cartilage. Journal of Biomechanics 142: 111242.

Guo, B., Liao, D., Li, X., Zeng, Y., and Yang, Q. (2007) Age and gender related changes in biomechanical properties of healthy human costal cartilage. Clinical Biomechanics 22(3): 292–297.

Holcombe, S., Wang, S., and Grotberg, J. (2016) The effect of rib shape on stiffness. Stapp Car Crash Journal 60: 11-24.

Holcombe, S., Ejima, S., and Wang, S. (2017) Calcification of costal cartilage in the adult rib cage. International Research Council on Biomechanics of Injury IRC-17-106: 737-744.

Humanetics website. (2024) Frontal impact ATDs https://www.humaneticsgroup.com/products/anthropomorphic-test-devices/frontal-impact

Huwe, L.W., Brown, W.E., Hu, J.C., and Athanasiou, K.A. (2017) Characterization of costal cartilage and its suitability as a cell source for articular cartilage tissue engineering. Journal of Tissue Engineering and Regenerative Medicine 12(5): 1163–1176.

Iraeus, J., Brolin, K., and Pipkorn, B. (2020) Generic finite element models of human ribs, developed and validated for stiffness and strain prediction – To be used in rib fracture risk evaluation for the human population in vehicle crashes. Journal of the Mechanical Behavior of Biomedical Materials 106: 103742.

Kang, Y.S., Kwon, H., Stammen, J., Moorhouse, K., and Agnew, A. (2021) Biomechanical response targets of adult human ribs in frontal impacts. Annals of Biomedical Engineering 49(22): 900-911.

Kent, R. (2008) Frontal thoracic response to dynamic loading: The role of superficial tissues, viscera and the rib cage. International Journal of Crashworthiness 13(3): 289–300.

Kent, R., Woods, W., and Bostrom, O. (2008) Fatality risk and the presence of rib fractures. Annals of Advances in Automotive Medicine 52.

Kindig, M.W. (2010) Tolerance to failure and geometric influences on the stiffness of human ribs under anterior-posterior loading. MS Thesis, University of Virginia.

Kindig, M.W., Lau, A.G., Forman, J.L., and Kent, R.W. (2010) Structural response of cadaveric ribcages under a localized loading: Stiffness and kinematic trends. Stapp Car Crash Journal 54: 337–380.

Kindig, M., Lau, A.G., and Kent, R.W. (2011) Biomechanical response of ribs under quasistatic frontal loading. Traffic Injury Prevention 12(4): 377–387.

Kohles, S.S. (2021) Application of flexural and membrane stress analysis to distinguish tensile and compressive moduli of biologic materials. Journal of the Mechanical Behavior of Biomedical Materials 119: 104474.

Larsson, K.J., Iraeus, J., Holcombe, S., and Pipkorn, B. (2023) Influences of human thorax variability on population rib fracture risk prediction using human body models. Frontiers in Bioengineering and Biotechnology 11: 1154272.

Lau, A., Oyen, M. L., Kent, R. W., Murakami, D., & Torigaki, T. (2008) Indentation stiffness of aging human costal cartilage. Acta Biomaterialia 4(1): 97–103.

Lee, E.L., Craig, M., and Scarboro, M. (2015) Real-world rib fracture patterns in frontal crashes in different restraint conditions. Traffic Injury Prevention 16: S115–S123.

Lee, J., Lee, E., Kim, H., and Son, Y. (2007) Comparison of articular cartilage with costal cartilage in initial cell yield, degree of dedifferentiation during expansion and redifferentiation capacity. Biotechnology and Applied Biochemistry 48(3): 149–158.

Li, Z., Kindig, M.W., Kerrigan, J.R., Untaroiu, C.D., Subit, D., Crandall, J.R., and Kent, R.W. (2010) Rib fractures under anterior–posterior dynamic loads: Experimental and finite-element study. Journal of Biomechanics 43(2): 228–234.

Lien, Y.-C., Chen, C.-H., and Lin, H.-C. (2009) Risk factors for 24-hour mortality after traumatic rib fractures owing to motor vehicle accidents: A nationwide population-based study. Annals of Thoracic Surgery 88(4): 1124–1130.

Mannen, E.M., Friis, E.A., Sis, H.L., Wong, B.M., Cadel, E.S., and Anderson, D.E. (2018) The rib cage stiffens the thoracic spine in a cadaveric model with body weight load under dynamic moments. Journal of the Mechanical Behavior of Biomedical Materials 84: 258–264.

Michelson, N. (1934) The calcification of the costal cartilage among whites and Negroes. Human Biology 6:543–557.

Murach, M. M., Kang, Y.-S., Bolte, J. H., Stark, D., Ramachandra, R., Agnew, A. M., Moorhouse, K., and Stammen, J. (2018) Quantification of skeletal and soft tissue contributions to thoracic response in a dynamic frontal loading scenario. Stapp Car Crash Journal 62: 193–269.

Murakami, D., Kobayashi, S., Torigaki, T., and Kent, R. (2006) Finite element analysis of hard and soft tissue contributions to thoracic response: sensitivity analysis of fluctuations in boundary conditions. Stapp Car Crash Journal 50, 169-189.

Nummela, M.T., Bensch, F.V., Pyhältö, T.T., and Koskinen, S.K. (2018) Incidence and imaging findings of costal cartilage fractures in patients with blunt chest trauma: A retrospective review of 1461 consecutive whole-body CT examinations for trauma. Radiology 286(2): 696–704.

Pattimore, D., Thomas, P., and Dave, S. (1992) Torso injury patterns and mechanisms in car crashes: An additional diagnostic tool. Injury 23(2): 123-126.

Pipkorn, B., and Kent, R. (2011) Validation of a human body thorax model and its use for force, energy and strain analysis in various loading conditions. International Research Council on Biomechanics of Injury IRC-11-56: 210–223.

Pipkorn, B., Jakobsson, L., Iraeus, J., and Östh, J. (2023) The SAFER HBM – A human body model for seamless integrated occupant analysis for all road users. International Technical Conference on the Enhanced Safety of Vehicles (ESV) 27: 23-0242. Yokohama, Japan.

Rampersadh, C., Agnew, A.M., Malcolm, S., Gierczycka, D., Iraeus, J., and Cronin, D. (2022) Factors affecting the numerical response and fracture location of the GHBMC M50 rib in dynamic anterior-posterior loading. Journal of the Mechanical Behavior of Biomedical Materials 136: 105527.

Rejtarová, O., Hejna, P., Soukup, T., and Kuchař, M. (2009) Age and sexually dimorphic changes in costal cartilages. A preliminary microscopic study. Forensic Science International 193(1–3): 72–78.

Roy, R., Kohles, S.S., Zaporojan, V., Peretti, G.M., Randolph, M.A., Xu, J., and Bonassar, L.J. (2004) Analysis of bending behavior of native and engineered auricular and costal cartilage. Journal of Biomedical Materials Research Part A 68A(4): 597–602.

Semine, A.A. and Damon, A. (1975) Costochondral ossification and aging in five populations. Human Biology 47(1): 101–116.

Sis, H.L., Mannen, E.M., Wong, B.M., Cadel, E.S., Bouxsein, M.L., Anderson, D.E., and Friis, E.A. (2016) Effect of follower load on motion and stiffness of the human thoracic spine with intact rib cage. Journal of Biomechanics 49(14): 3252–3259.

Society of Automotive Engineers, SAE. (2007) Instrumentation for impact test-part 1-electronic instrumentation, J211/1.

Stacey, M., Dutta, D., Cao, W., Asmar, A., Elsayed-Ali, H., Kelly, R., and Beskok, A. (2013) Atomic force microscopy characterization of collagen ‘nanostraws’ in human costal cartilage. Micron 44: 483–487.

Teale, C., Romaniuk, C., and Mulley, G. (1989) Calcification on chest radiographs: The association with age. Age and Ageing 18(5): 333–336.

Vezin, P., and Berthet, F. (2009) Structural characterization of human rib cage behavior under dynamic loading. Stapp Car Crash Journal 53: 93–125.

Weber, M., Rothschild, M.A., and Niehoff, A. (2021) Anisotropic and age-dependent elastic material behavior of the human costal cartilage. Scientific Reports 11(1): 13618.

World Health Organization. (2023) Global status report on road safety 2023. World Health Organization.

Yoganandan, N. and Pintar, F. (1998) Biomechanics of human thoracic ribs. Journal of Biomechanical Engineering 120:100-104.

Zeng, W., Mukherjee, S., Caudillo, A., Forman, J., and Panzer, M.B. (2021) Evaluation and validation of thorax model responses: A hierarchical approach to achieve high biofidelity for thoracic musculoskeletal system. Frontiers in Bioengineering and Biotechnology 9: 712656.

Zioupos, P. and Currey, J.D. (1998) Changes in the stiffness, strength, and toughness of human cortical bone with age. Bone 22(1): 57–66.

APPENDIX

Appendix A. Preliminary test/trial data

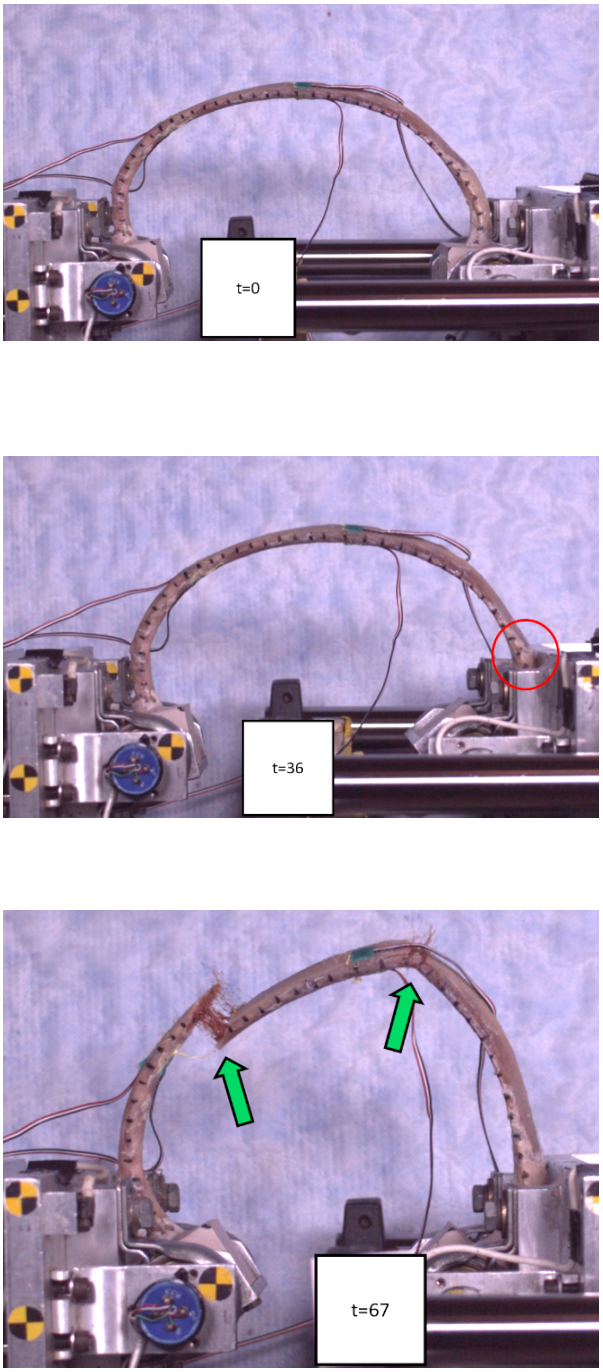

Figure A1. Hrb469 rib+CC trial without wedges at time zero (top), time when CC impacted front plate (middle), and time of fracture (bottom)

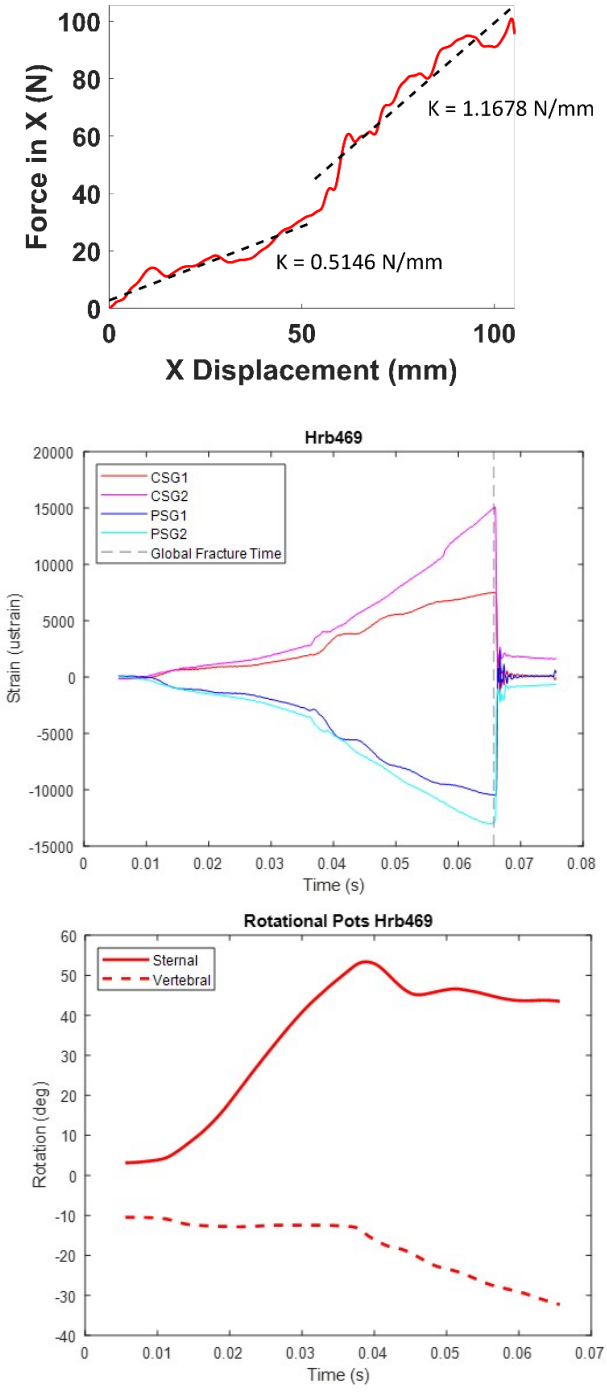

Figure A2. Hrb469 rib+CC without wedges showing F-D curve (top), strain-time histories (middle), and rotational pot data (bottom)

Table A1. Demographic and rib information for trial tests

Test ID	Age (yrs)	Sex	Height (cm)	Weight (kg)	Rib	Fracture Number	Fracture Location* (%)
Hrb469	62	M	175.3	68.5	L5+CC	1	42 (M), 66 (M)
Hrb511 (A)	54	M	172.7	59.0	R5+CC	1	63 (A)
Hrb512 (B)	57	M	172.0	55.3	R5+CC	2	43 (M), 68 (M)
Hrb513 (C)	58	M	172.7	63.3	R5+CC	1	87 (A)
Hrb514 (D)	67	M	166.4	68.0	R5+CC	1	46 (M)
Hrb515 (E)	67	M	166.4	68.0	R5+CC	1	40 (M)
Hrb516	54	M	175.3	68.5	L7	2	100 (A)
Hrb517	68	M	170.2	65.8	R6	2	100 (A)

* M=Middle, A=Anterior

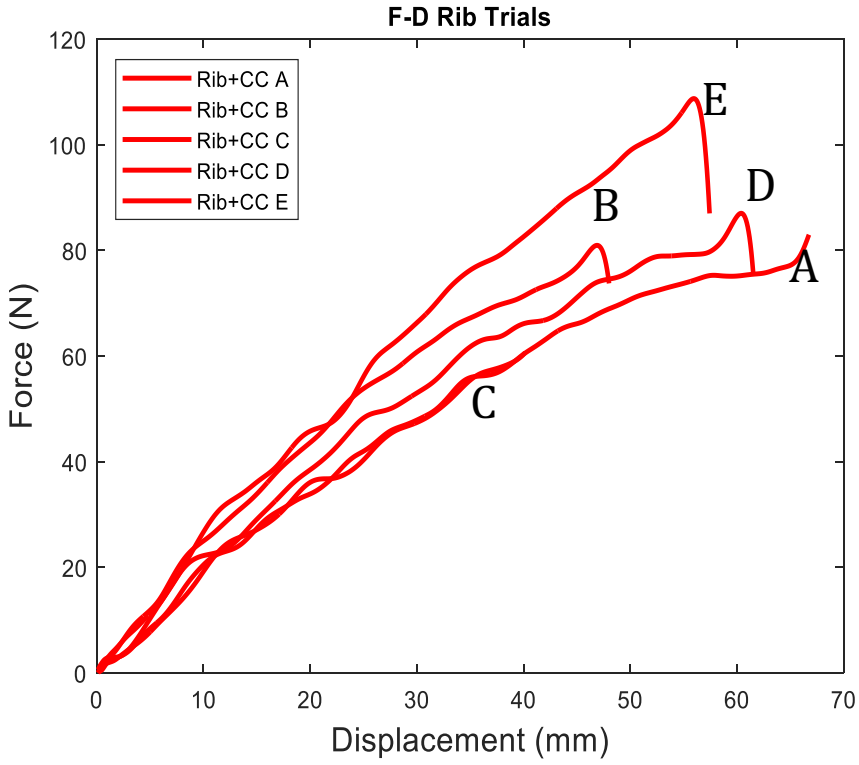

Figure A3. F-D curves for rib+CC trials with sternal wedges

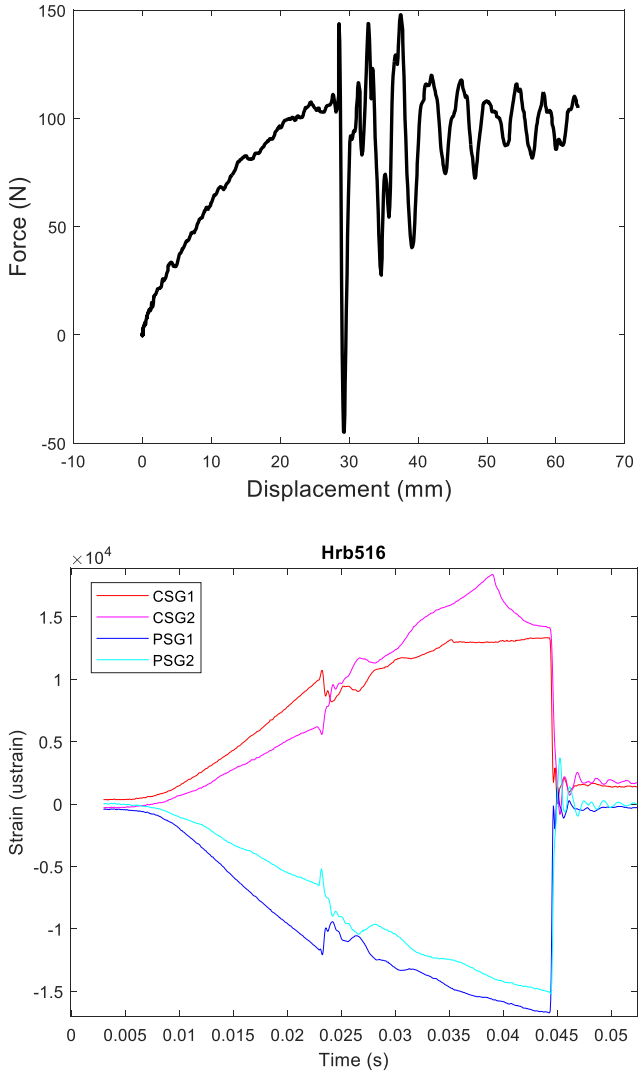

Figure A4. Hrb516 rib trial with sternal wedges F-D curve (top) and strain-time histories (bottom)

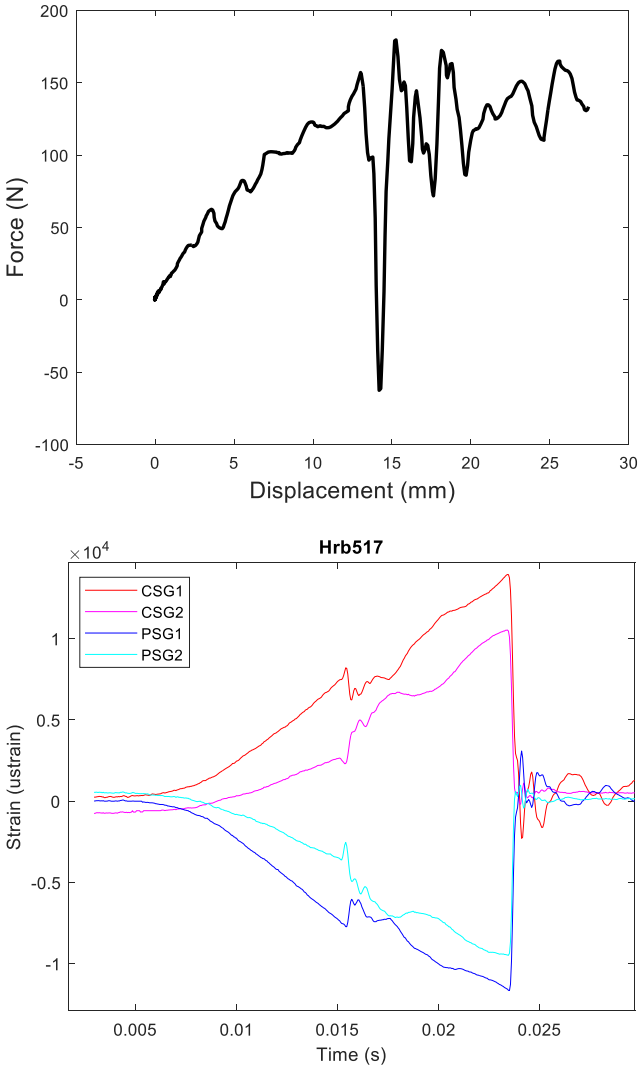

Figure A5. Hrb517 rib trial with sternal wedges F-D curve (top) and strain-time histories (bottom)

Appendix B. Rib pair fracture information

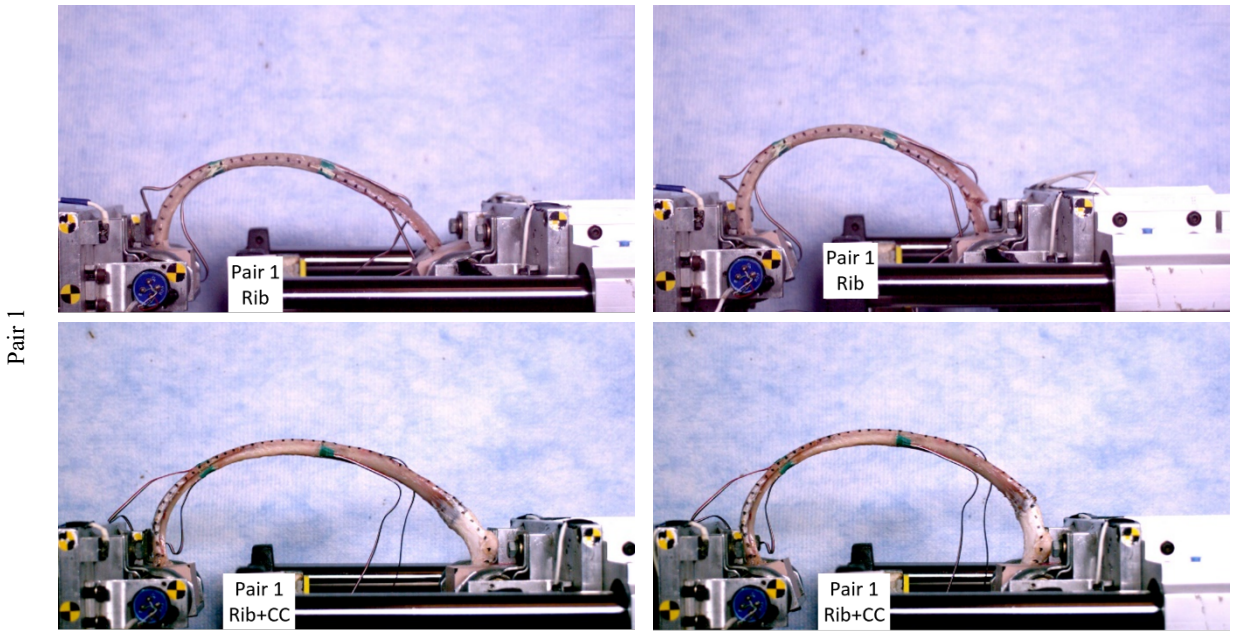

Figure B1. Rib (top) and rib+CC (bottom) comparisons at time zero (left) and at time of fracture (right)

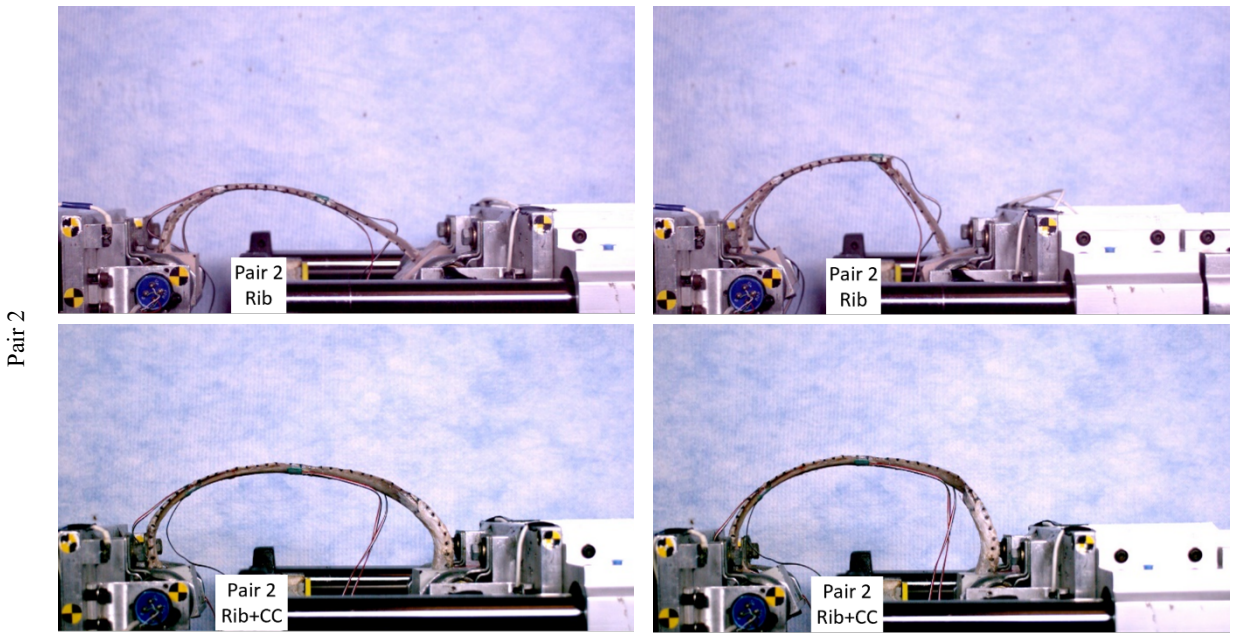

Figure B2. Rib (top) and rib+CC (bottom) comparisons at time zero (left) and at time of fracture (right)

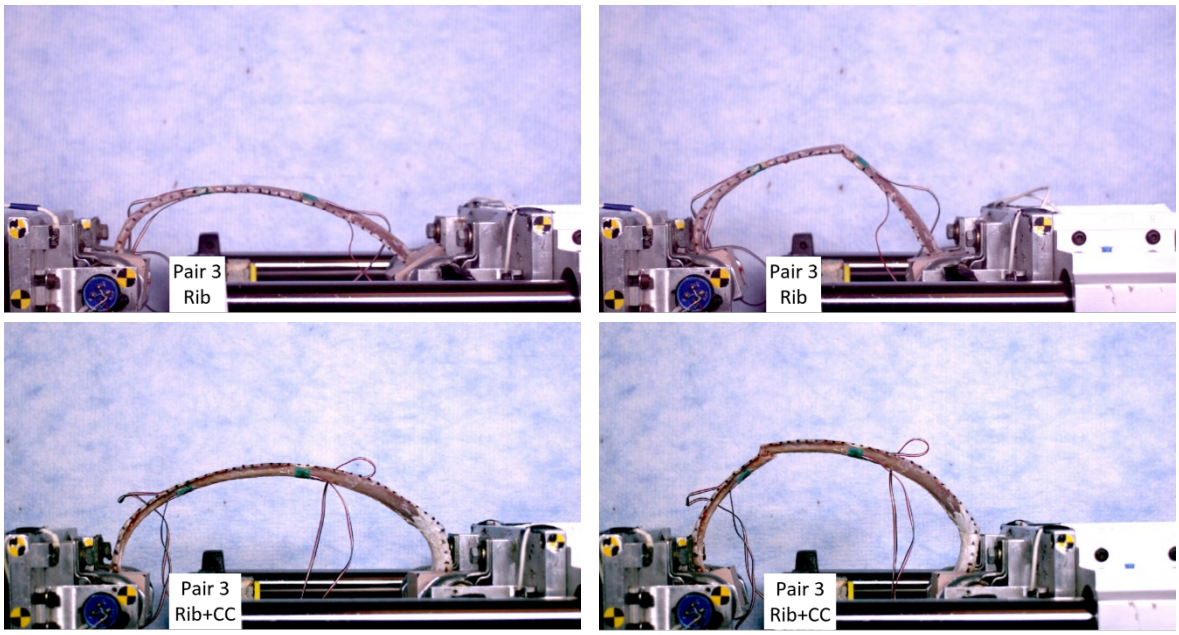

Figure B3. Rib (top) and rib+CC (bottom) comparisons at time zero (left) and at time of fracture (right)

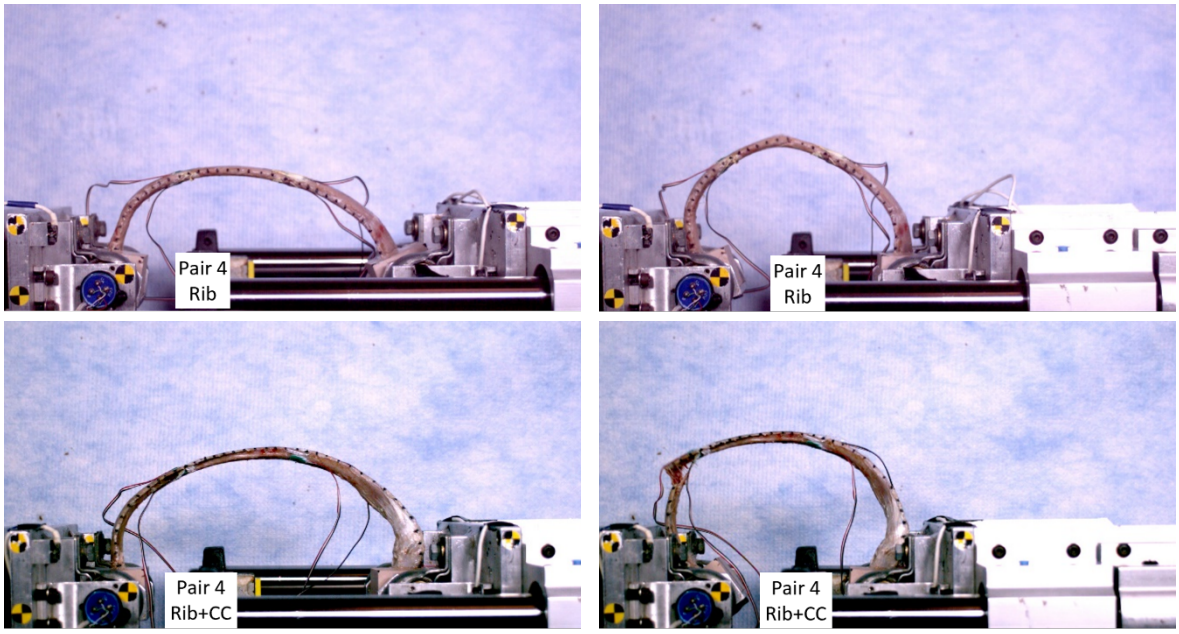

Figure B4. Rib (top) and rib+CC (bottom) comparisons at time zero (left) and at time of fracture (right)

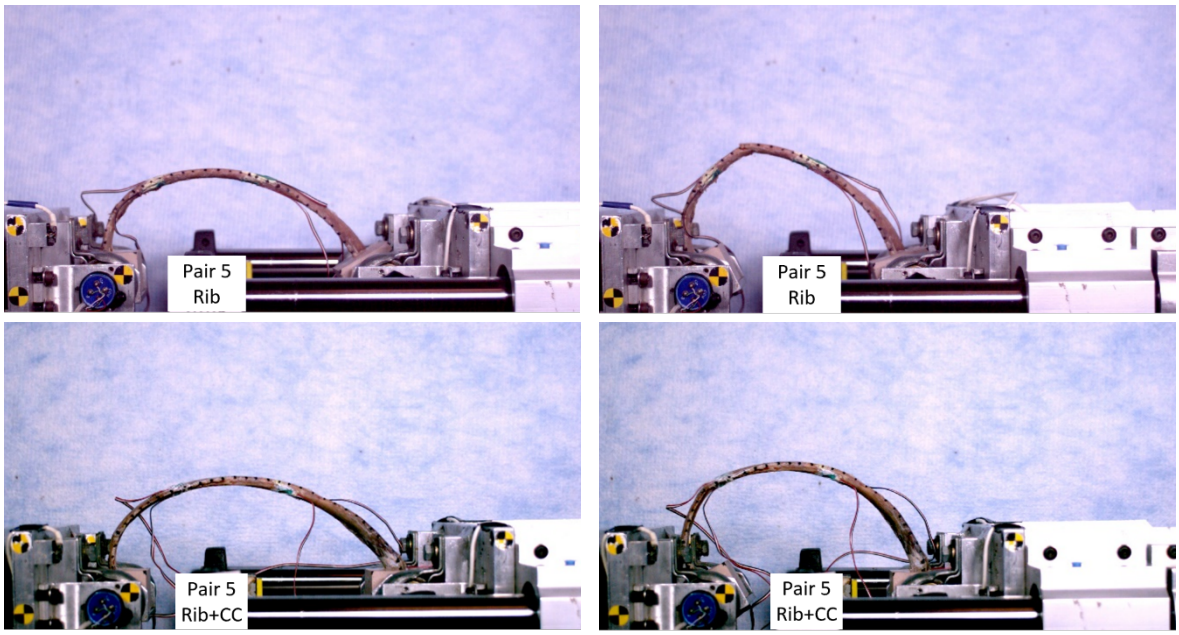

Figure B5. Rib (top) and rib+CC (bottom) comparisons at time zero (left) and at time of fracture (right)

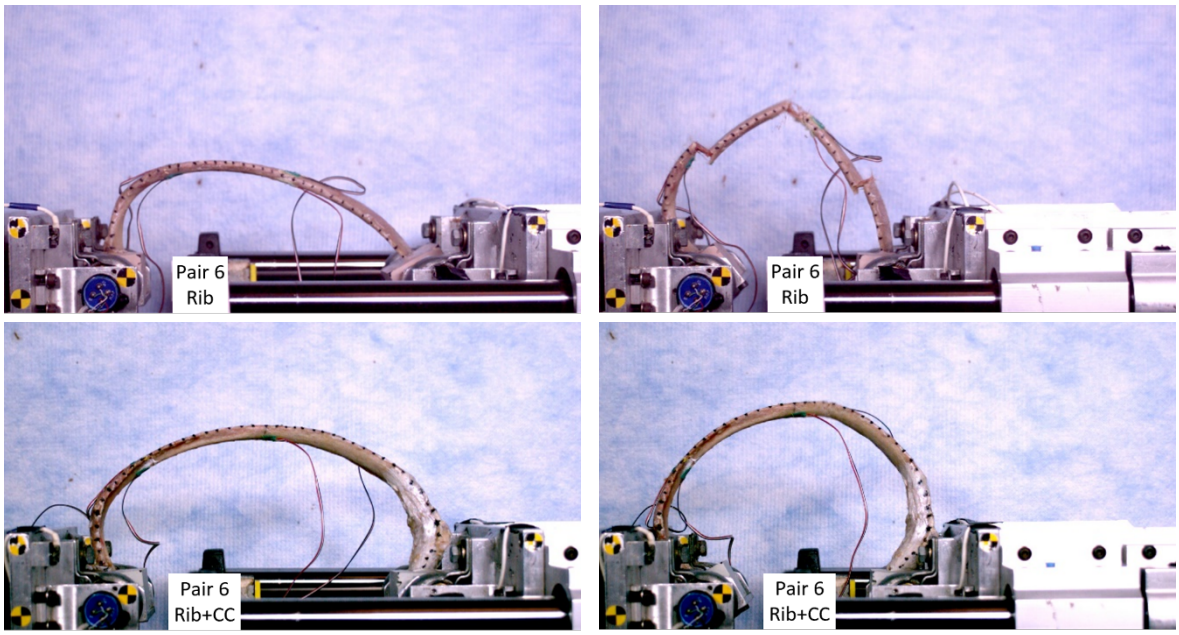

Figure B6. Rib (top) and rib+CC (bottom) comparisons at time zero (left) and at time of fracture (right)

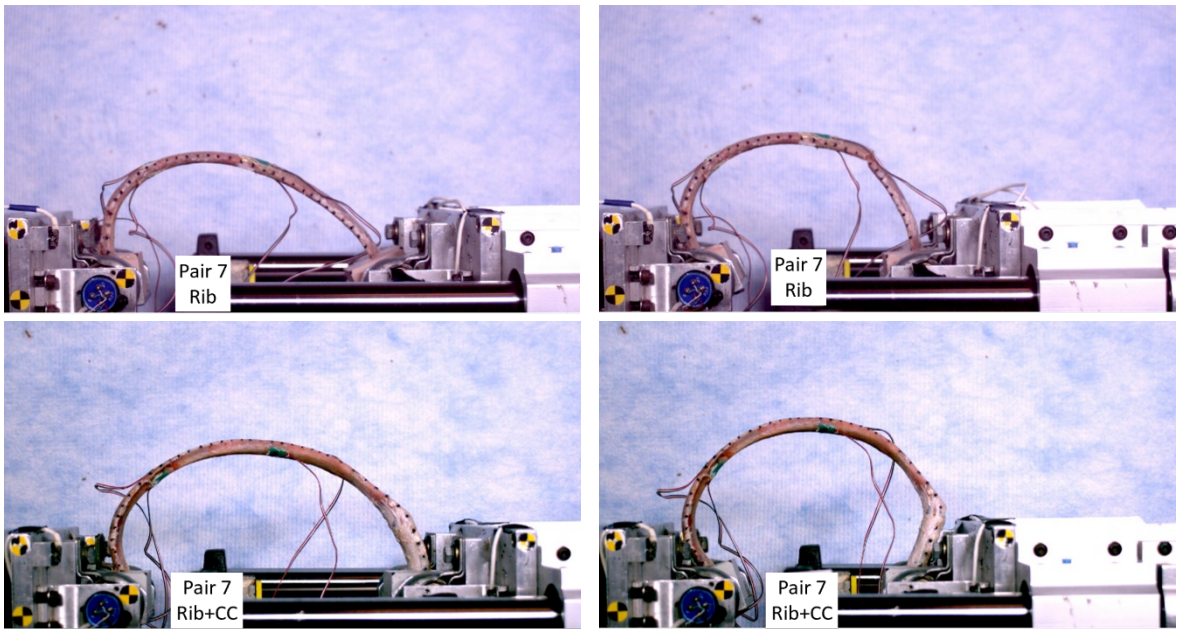

Figure B7. Rib (top) and rib+CC (bottom) comparisons at time zero (left) and at time of fracture (right)

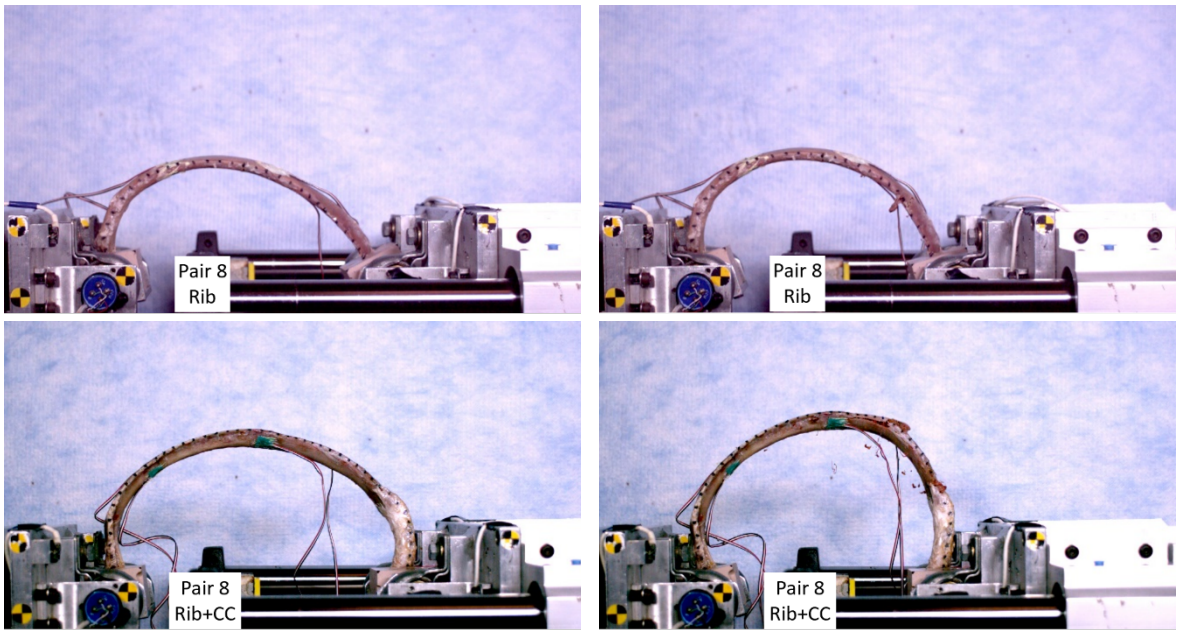

Figure B8. Rib (top) and rib+CC (bottom) comparisons at time zero (left) and at time of fracture (right)

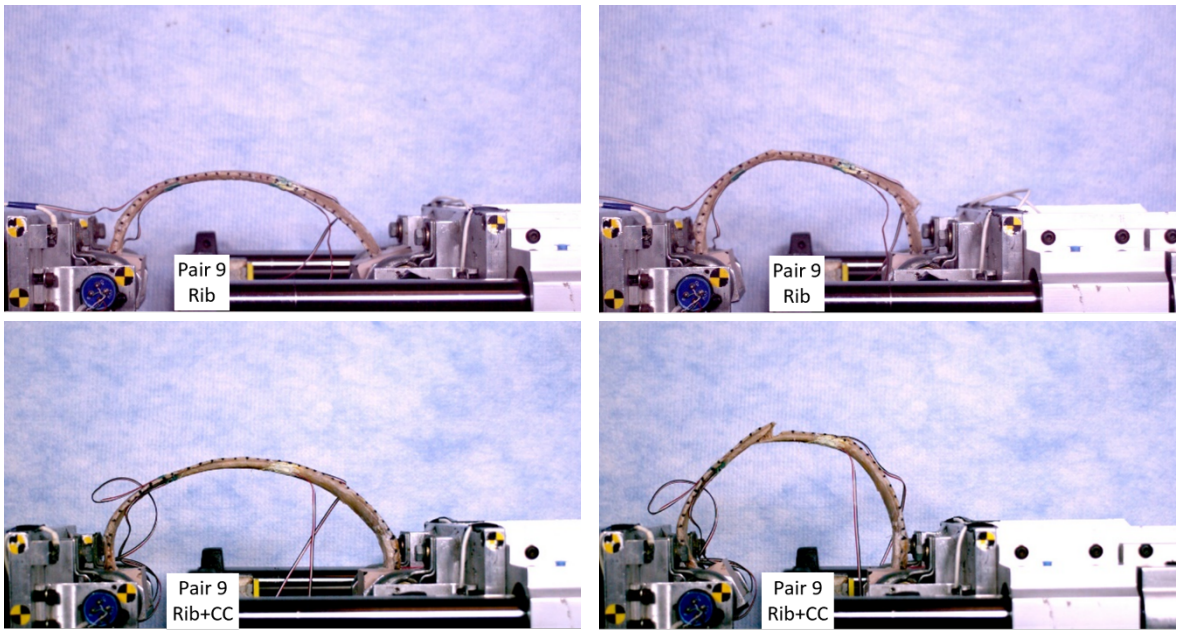

Figure B9. Rib (top) and rib+CC (bottom) comparisons at time zero (left) and at time of fracture (right)

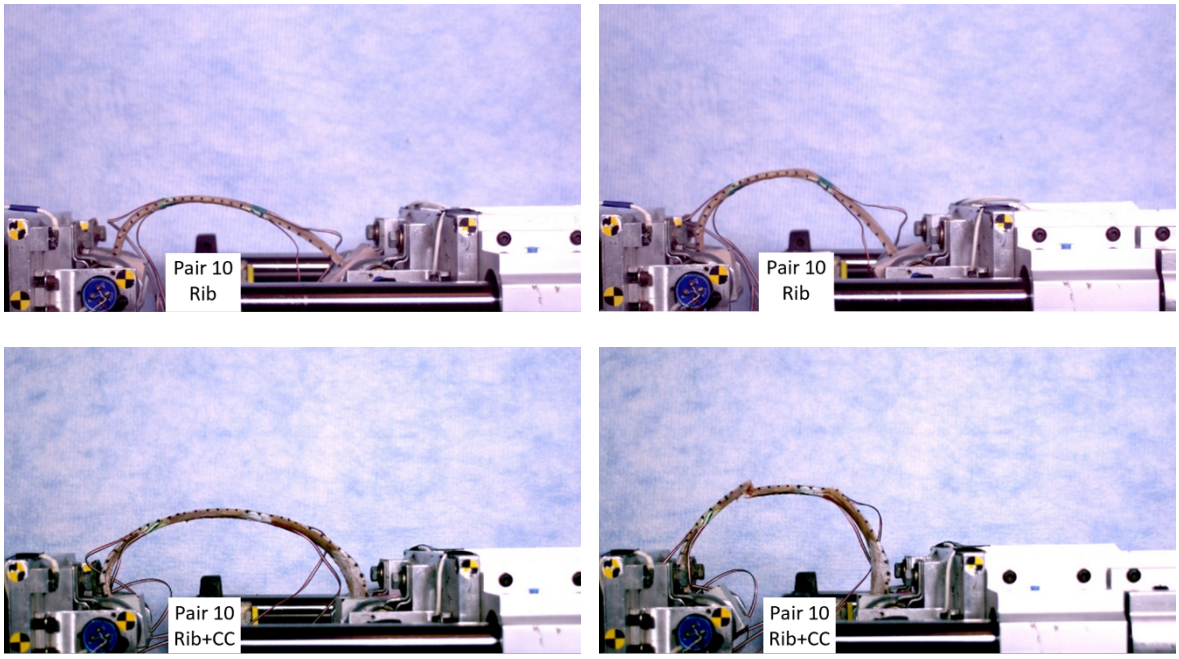

Figure B10. Rib (top) and rib+CC (bottom) comparisons at time zero (left) and at time of fracture (right)

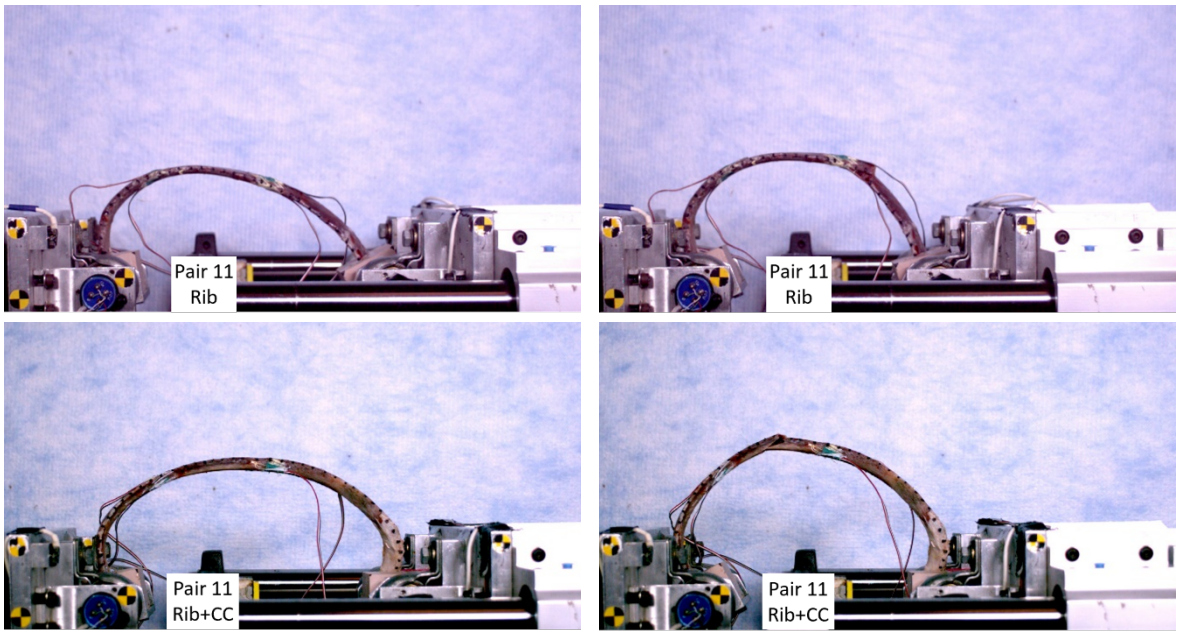

Figure B11. Rib (top) and rib+CC (bottom) comparisons at time zero (left) and at time of fracture (right)

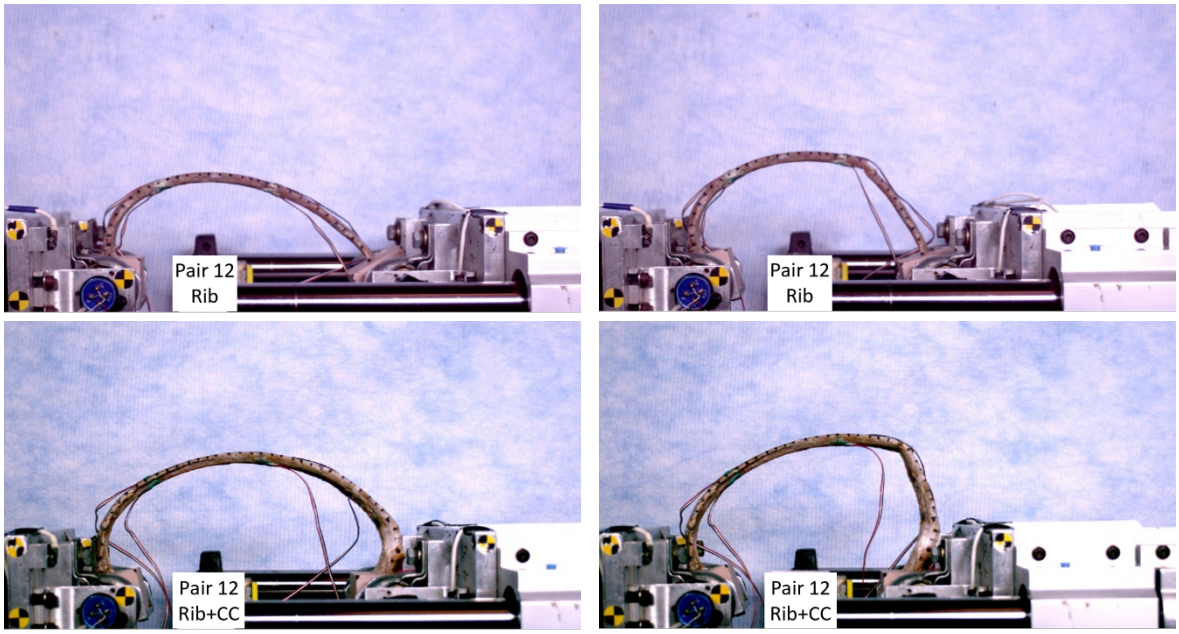

Figure B12. Rib (top) and rib+CC (bottom) comparisons at time zero (left) and at time of fracture (right)

Pair 13

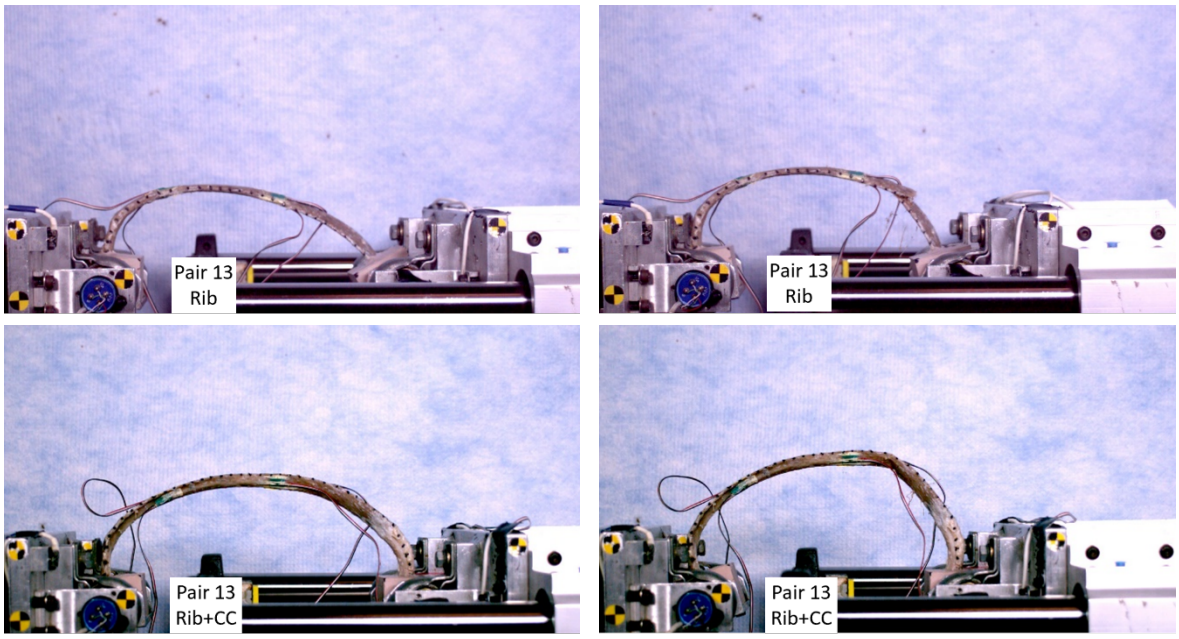

Figure B13. Rib (top) and rib+CC (bottom) comparisons at time zero (left) and at time of fracture (right)

Pair 14

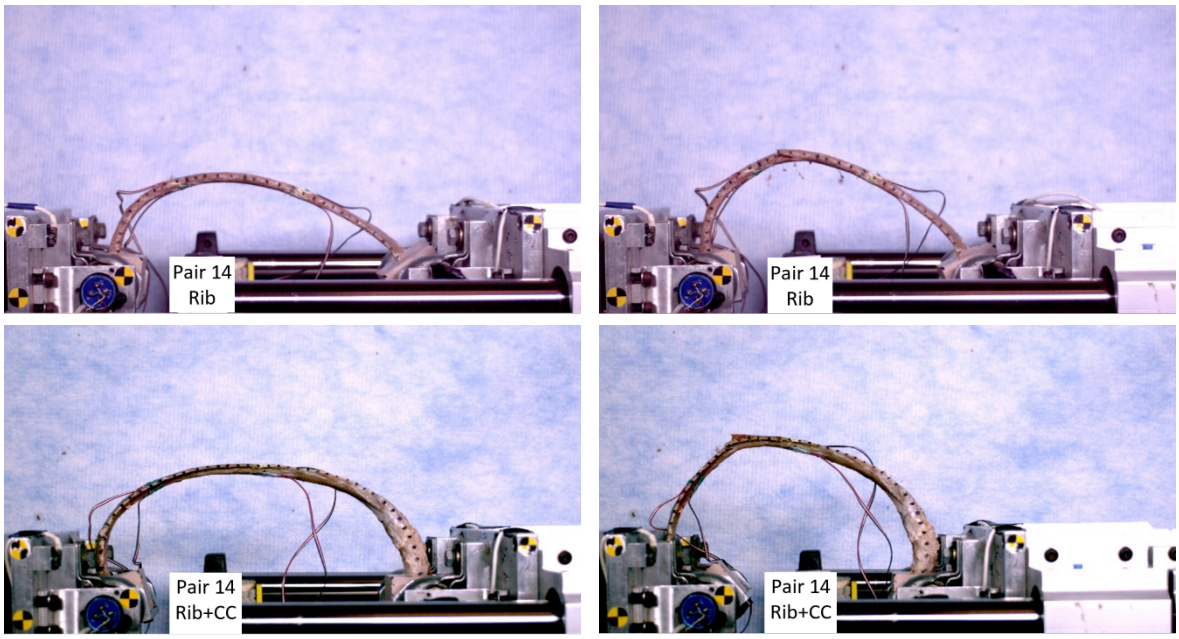

Figure B14. Rib (top) and rib+CC (bottom) comparisons at time zero (left) and at time of fracture (right)

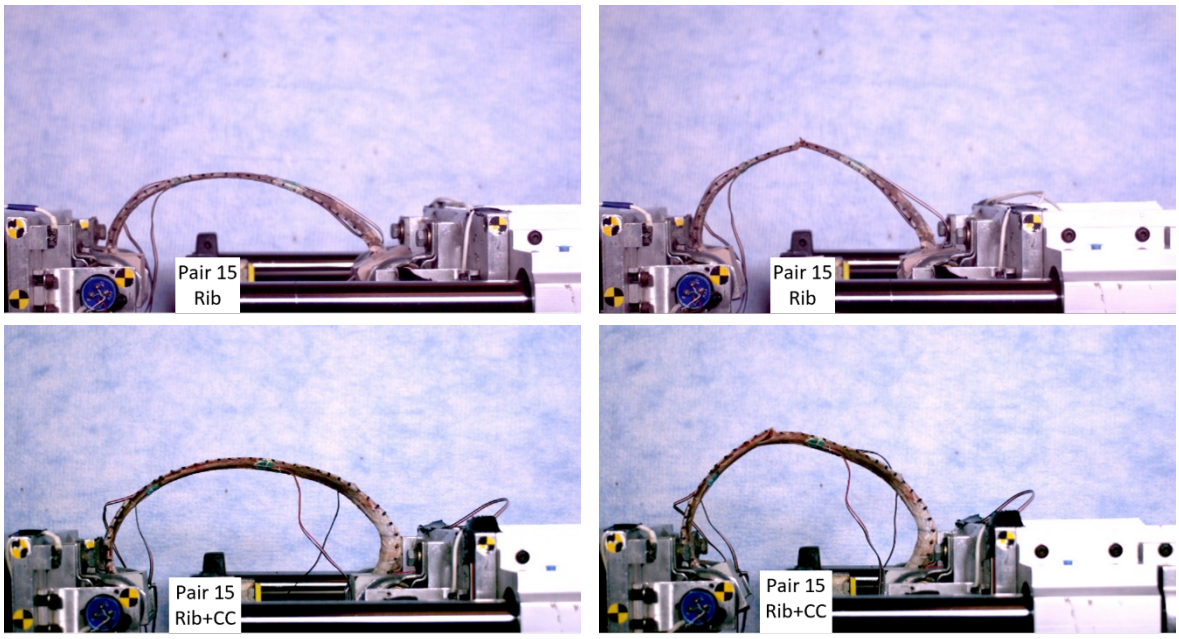

Figure B15. Rib (top) and rib+CC (bottom) comparisons at time zero (left) and at time of fracture (right)

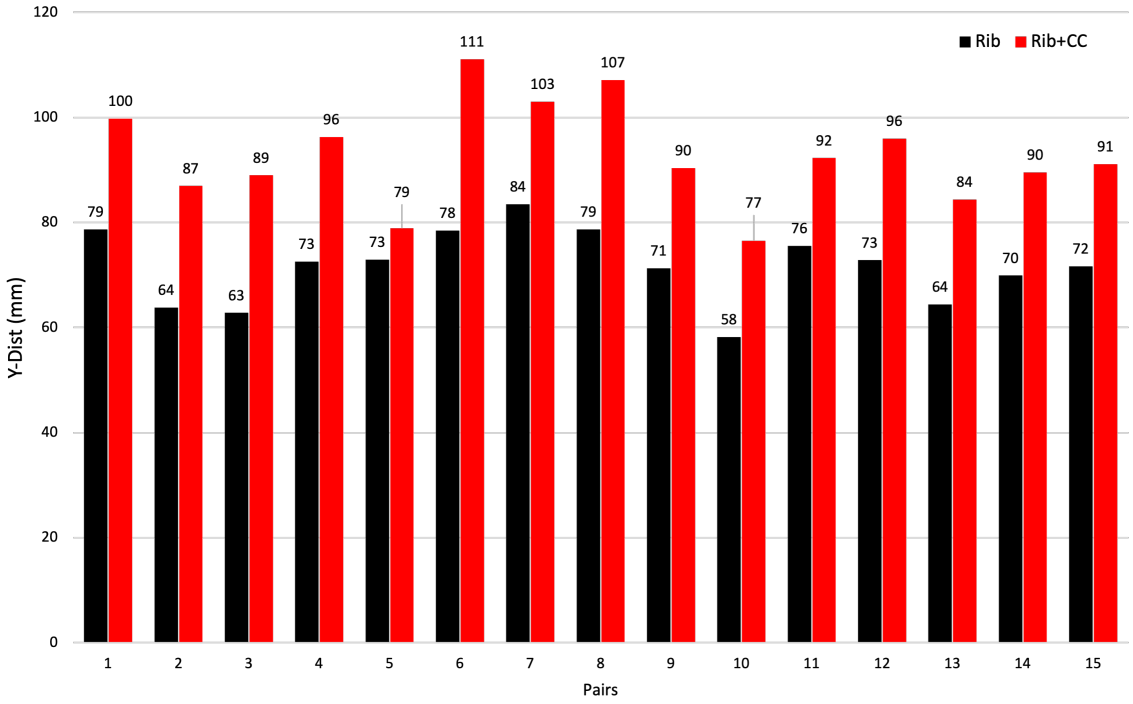

Figure B16. Y-Distance comparisons for ribs (black) and rib+CCs (red) in pairs

Table B1. Rib Data Summary for 5th Rib Pairs

Pair ID	Rib Condition	Cv.Le *(mm)*	Sp.Le *(mm)*	Y-Dist *(mm)*	CC Length *(mm)*	Fracture Number	Fracture Location *(%)*	Costal Cartilage Calcification (Barchilon et al. 1996)
1	Rib	321	201	79	*	1	79 (A)	-
	Rib+CC	385	223	100	40	1	90 (A)	None
2	Rib	286	190	64	*	1	60 (M)	-
	Rib+CC	360	196	87	40	1	90 (A)	None
3	Rib	305	221	63	*	2	56 (M) 86 (A)	-
	Rib+CC	370	230	89	25	1	43 (M)	Minimal
4	Rib	314	207	73	*	2	46 (M) 88 (A)	-
	Rib+CC	368	202	96	33	1	31 (M)	Maximal
5	Rib	297	187	73	*	1	42 (M)	-
	Rib+CC	328	197	79	9	2	33 (M) 80 (A)	Minimal
6	Rib	335	219	78	*	3	34 (M) 56 (M) 73 (A)	-
	Rib+CC	428	216	111	54	1+	70 (M) CC	Maximal
7	Rib	329	191	84	*	1	68 (M)	-
	Rib+CC	385	211	103	35	1	100 (A)	Maximal
8	Rib	313	190	79	*	1	68 (M)	-
	Rib+CC	383	203	107	40	1	74 (A)	Minimal
9	Rib	295	196	71	*	2	40 (M) 72 (A)	-
	Rib+CC	358	194	90	20	2	49 (M) 65 (M)	Medium
10	Rib	260	179	58	*	1	55 (M)	-
	Rib+CC	313	179	77	20	2+	48 (M) 68 (M) CC	None
11	Rib	315	190	76	*	1	63 (M)	-
	Rib+CC	373	195	92	30	1	44 (M)	Maximal
12	Rib	303	195	73	*	1	64 (M)	-
	Rib+CC	378	190	96	25	1+	76 (A) CC	Minimal
13	Rib	299	198	64	*	1	71 (A)	-
	Rib+CC	359	208	84	30	1	74 (A)	None
14	Rib	313	218	70	*	1	41 (M)	-
	Rib+CC	383	212	90	37	1+	47 (M) CC	Minimal
15	Rib	307	196	72	*	1	47 (M)	-
	Rib+CC	367	187	91	25	1	50 (M)	Maximal

+1 additional fracture each occurred in the costal cartilage for these tests. M=Middle, A=Anterior.

Appendix C. Structural properties

Table C1. Structural Property Data for all 5th Rib Pairs

Pair ID	Rib Condition	Time *(ms)*		Force *(N)*		Displacement *(%)*		Stiffness *(N/mm)*	Energy *(N*mm)*	
		Yield	Fracture	Yield	Peak	Yield	Fracture		Plastic	Total
1	Rib	17.2	31.1	71.7	141.7	7.4	20.3	4.9	2873.0	3440.6
	Rib+CC	25.9	26.0	81.3	81.3	14.2	14.2	2.3	0	1362.2
2	Rib	22.6	35.0	23.1	38.0	13.8	26.8	0.9	666.5	1041.9
	Rib+CC	15.4	27.6	9.8	22.3	6.0	18.5	0.9	391.0	450.9
3	Rib	28.9	37.0	31.4	42.0	17.5	24.5	0.8	515.3	1299.3
	Rib+CC	17.9	34.2	18.0	37.9	7.2	21.1	1.1	909.9	1081.3
4	Rib	17.2	45.9	53.8	130.5	7.1	31.7	3.7	5265.6	5716.2
	Rib+CC	18.2	55.5	40.8	108.6	8.3	41.3	2.6	5510.2	5856.3
5	Rib	22.1	31.5	38.4	51.1	13.5	23.4	1.5	840.2	1405.4
	Rib+CC	25.6	35.2	36.5	47.2	16.0	25.5	1.2	769.0	1427.8
6	Rib	21.3	62.7	69.2	112.2	10.9	42.5	2.9	7042.6	7964.6
	Rib+CC	15.7	55.8	29.7	91.2	5.5	28.4	2.8	3258.5	3424.7
7	Rib	15.8	32.1	36.8	97.0	6.4	23.0	3.1	2060.0	2296.9
	Rib+CC	21.3	46.1	47.5	73.3	11.0	32.8	2.1	2805.0	3258.0
8	Rib	19.6	19.7	76.1	76.1	10.5	10.5	3.6	0	801.2
	Rib+CC	14.4	28.1	20.6	65.3	4.7	17.9	2.3	1175.7	1253.2
9	Rib	26.0	33.1	49.5	59.7	16.7	23.6	1.5	717.8	1709.4
	Rib+CC	15.8	38.9	17.2	49.4	6.4	30.1	1.4	1618.8	1729.3
10	Rib	26.4	26.4	43.8	44.5	18.9	18.9	1.1	0	874.1
	Rib+CC	28.2	35.7	28.5	35.9	21.4	29.8	0.7	475.8	1124.2
11	Rib	23.0	23.0	32.1	32.1	14.2	14.2	1.1	0	476.4
	Rib+CC	26.8	26.8	39.5	42.5	16.5	16.5	1.4	0	740.2
12	Rib	25.7	25.8	65.8	65.8	16.6	16.6	1.7	0	1101.0
	Rib+CC	21.2	21.3	27.2	27.2	12.6	12.6	1.2	0	349.9
13	Rib	20.0	21.4	18.1	18.1	10.6	10.6	0.6	0	239.1
	Rib+CC	20.5	24.9	14.0	14.9	10.3	14.5	0.7	127.1	294.7
14	Rib	17.2	23.4	32.0	50.0	7.3	12.8	2.0	504.0	817.3
	Rib+CC	16.8	41.5	20.7	56.7	6.8	29.0	1.5	1941.5	2080.6
15	Rib	25.9	26.0	13.7	15.9	16.7	16.7	0.5	0	320.9
	Rib+CC	31.2	31.3	21.5	21.9	23.2	23.2	0.4	0	553.5

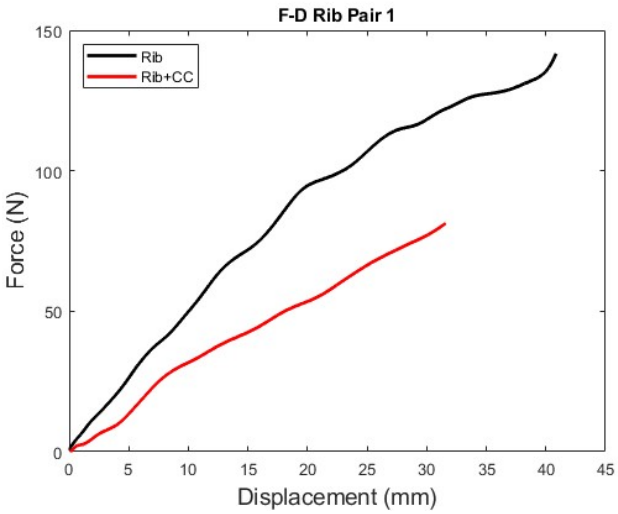

Figure C1. Pair 1 F-D Curves

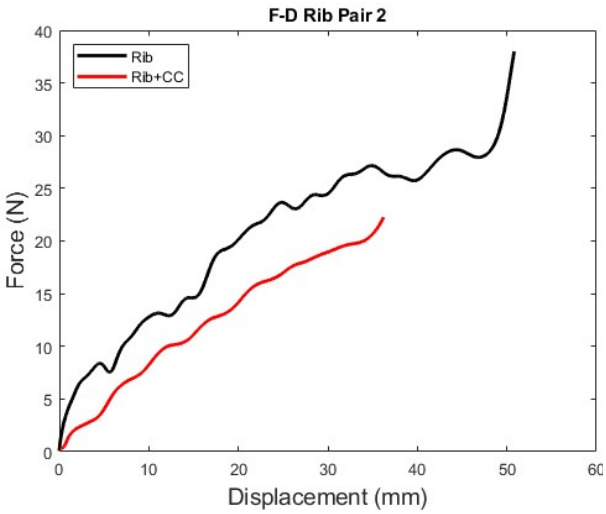

Figure C2. Pair 2 F-D Curves

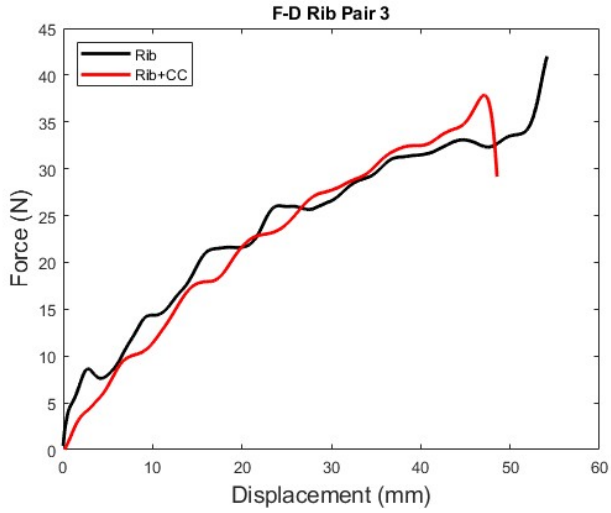

Figure C3. Pair 3 F-D Curves

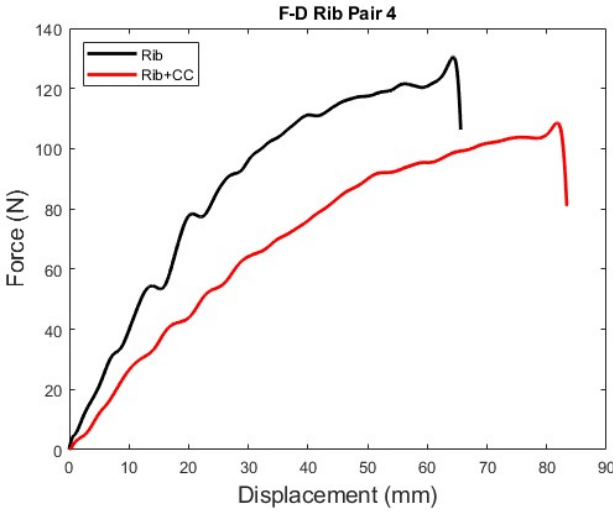

Figure C4. Pair 4 F-D Curves

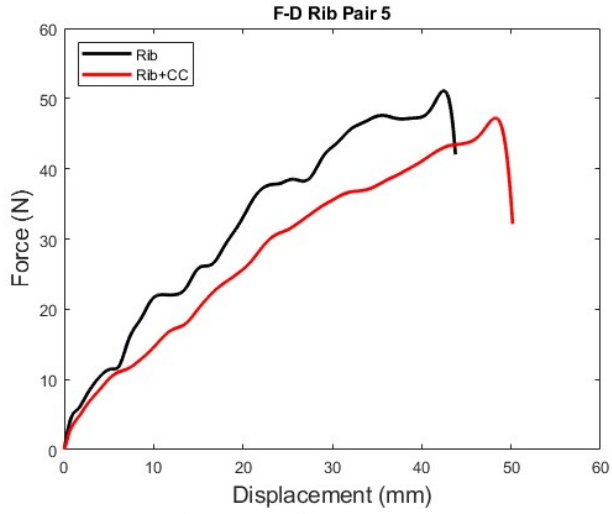

Figure C5. Pair 5 F-D Curves

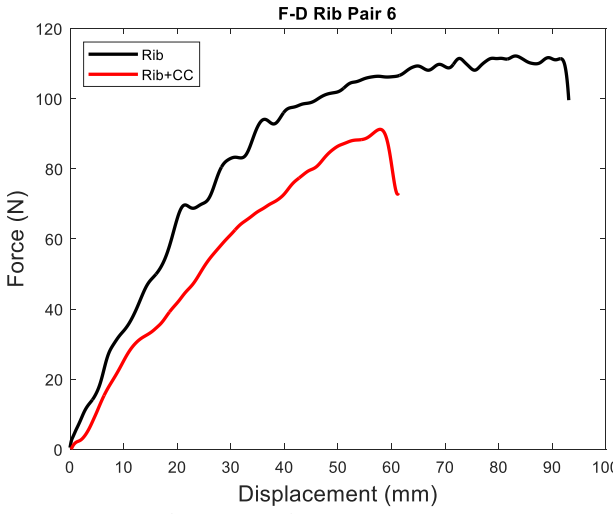

Figure C6. Pair 6 F-D Curves

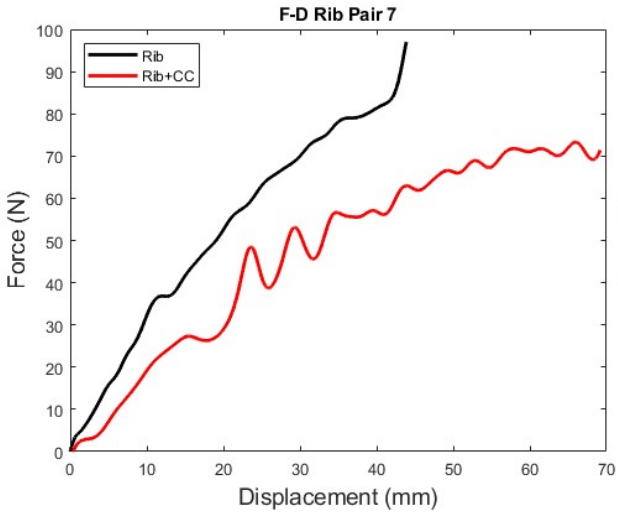

Figure C7. Pair 7 F-D Curves

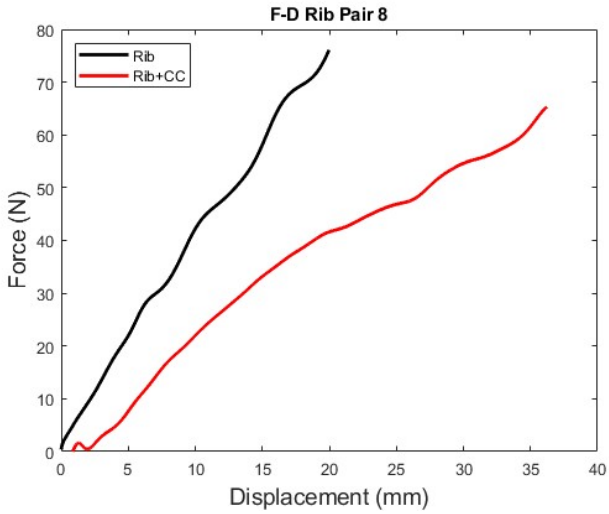

Figure C8. Pair 8 F-D Curves

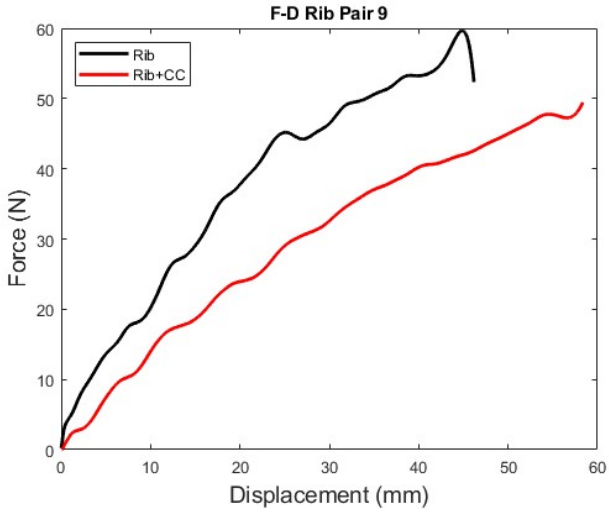

Figure C9. Pair 9 F-D Curves

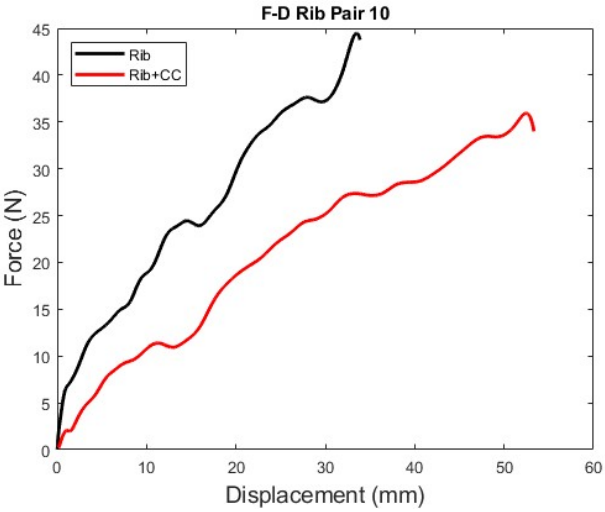

Figure C10. Pair 10 F-D Curves

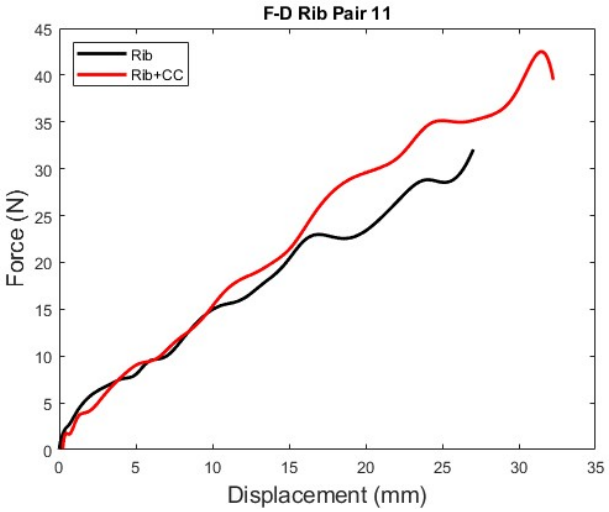

Figure C11. Pair 11 F-D Curves

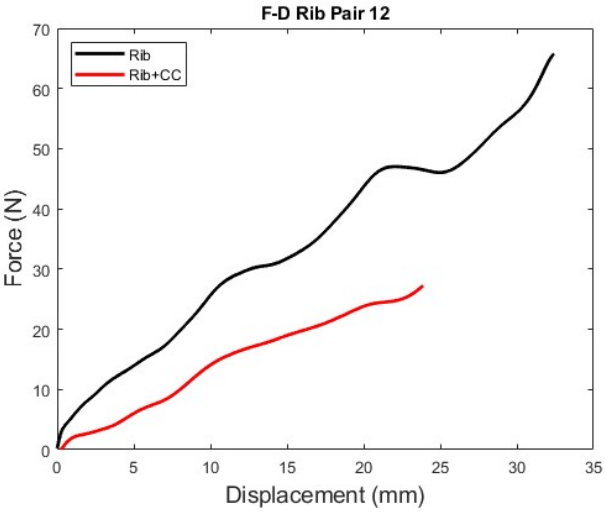

Figure C12. Pair 12 F-D Curves

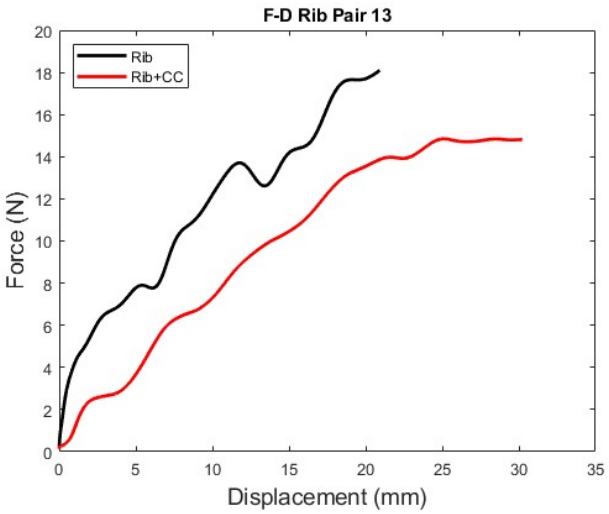

Figure C13. Pair 13 F-D Curves

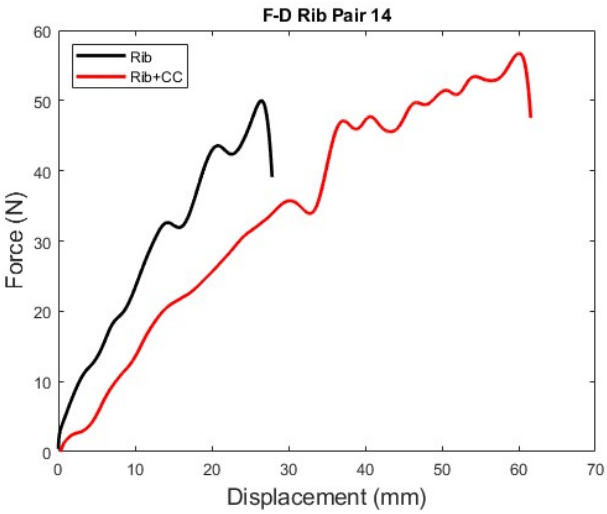

Figure C14. Pair 14 F-D Curves

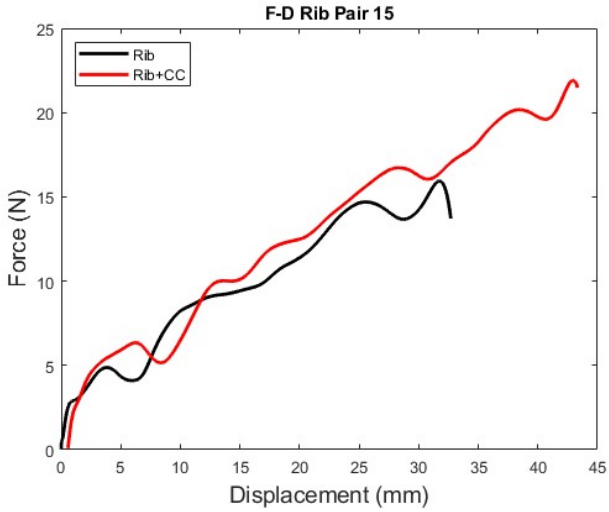

Figure C15. Pair 15 F-D Curves

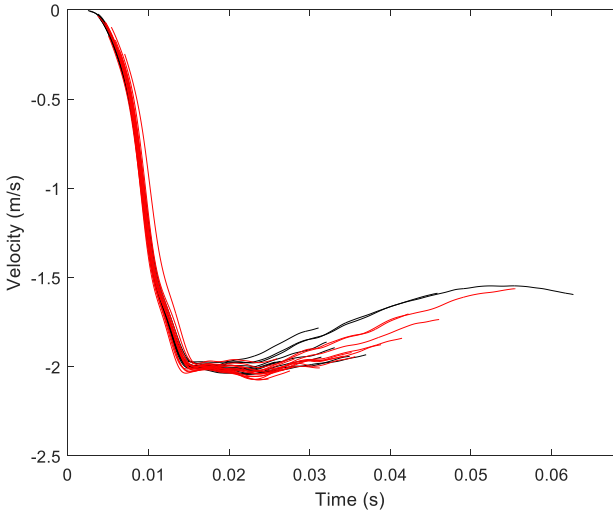

Figure C16. Velocity time histories for all ribs (black) and rib+CCs (red) illustrating repeatability of input.

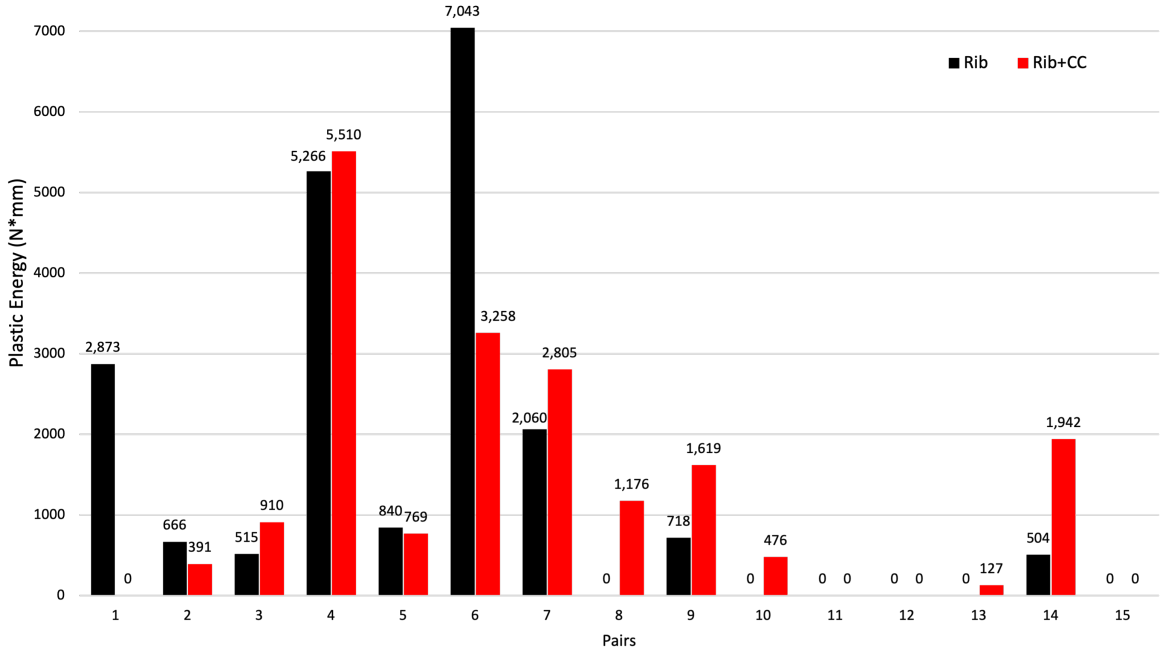

Figure C17. Plastic energy comparisons within pairs

Appendix D. Rotational pot data

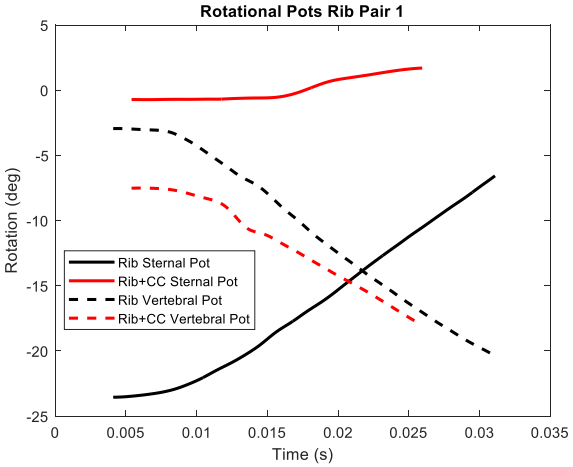

Figure D1. Pair 1 Pot Rotations

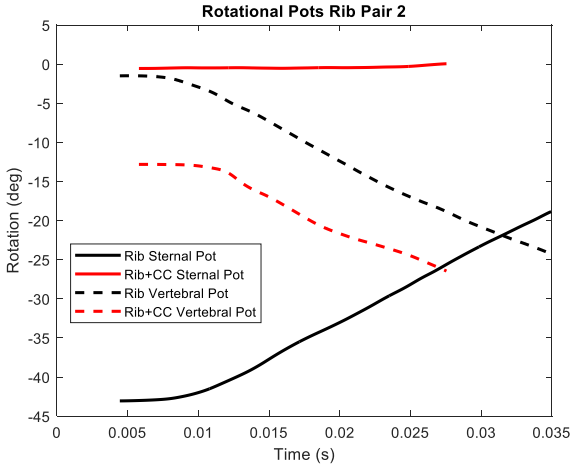

Figure D2. Pair 2 Pot Rotations

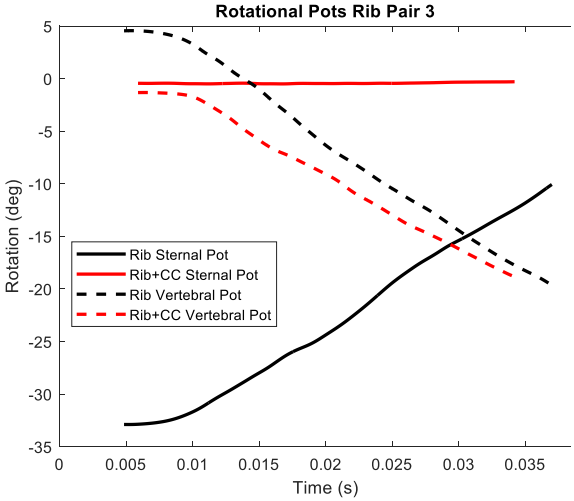

Figure D3. Pair 3 Pot Rotations

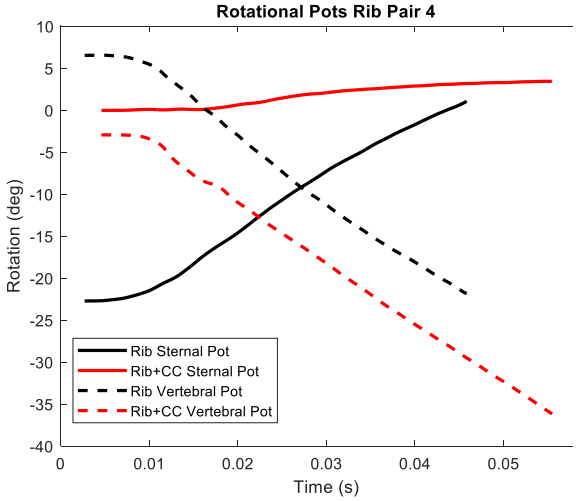

Figure D4. Pair 4 Pot Rotations

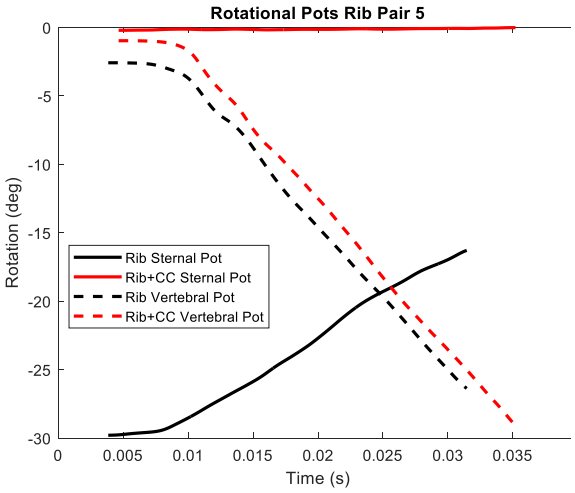

Figure D5. Pair 5 Pot Rotations

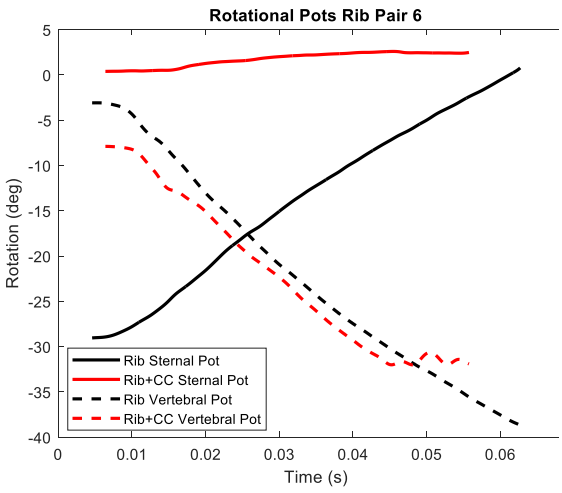

Figure D6. Pair 6 Pot Rotations

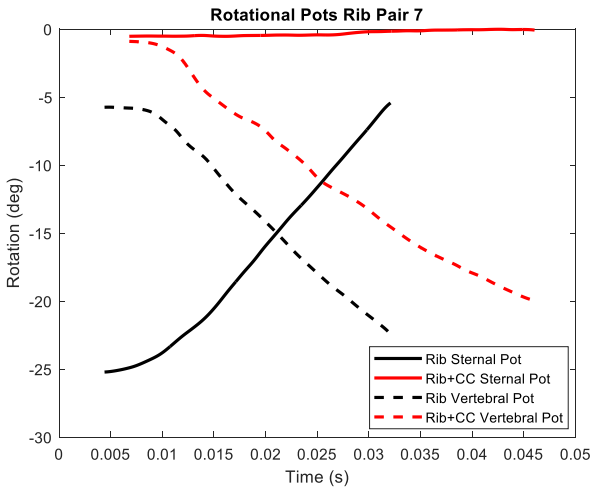

Figure D7. Pair 7 Pot Rotations

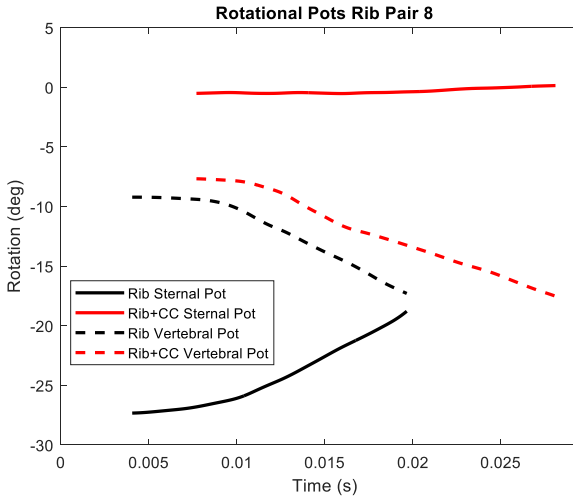

Figure D8. Pair 8 Pot Rotations

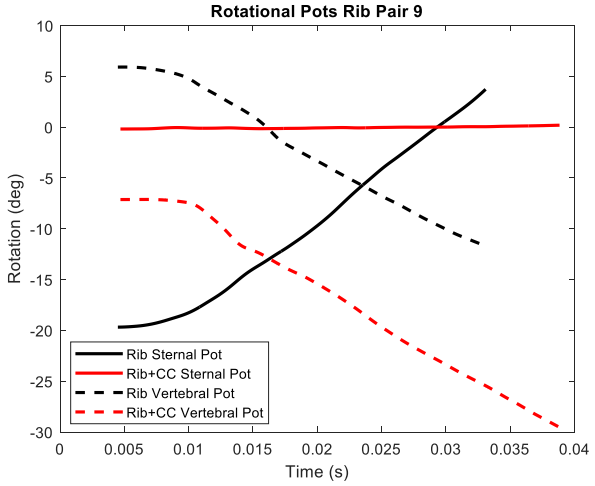

Figure D9. Pair 9 Pot Rotations

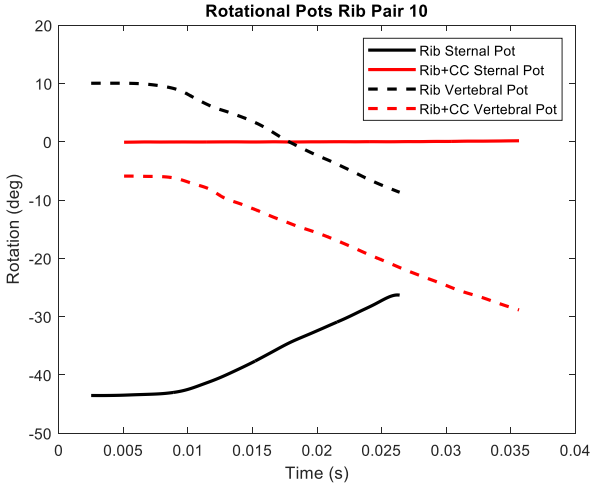

Figure D10. Pair 10 Pot Rotations

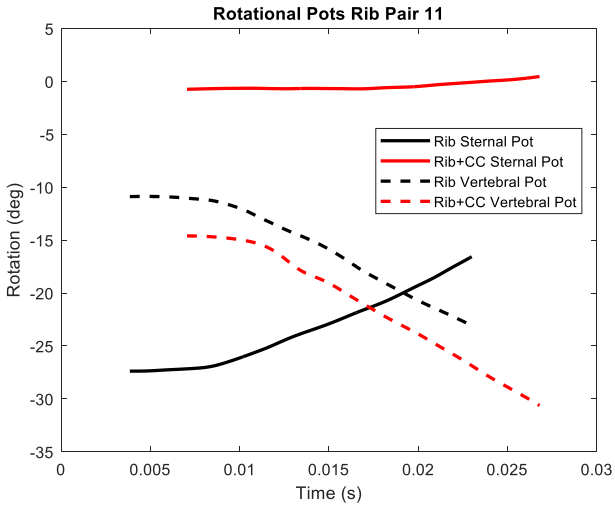

Figure D11. Pair 11 Pot Rotations

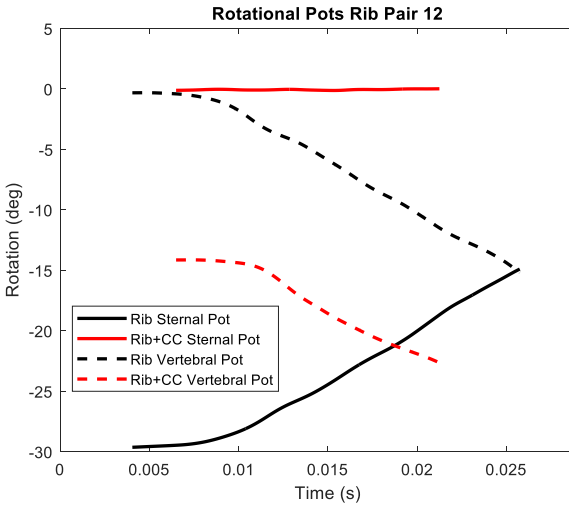

Figure D12. Pair 12 Pot Rotations

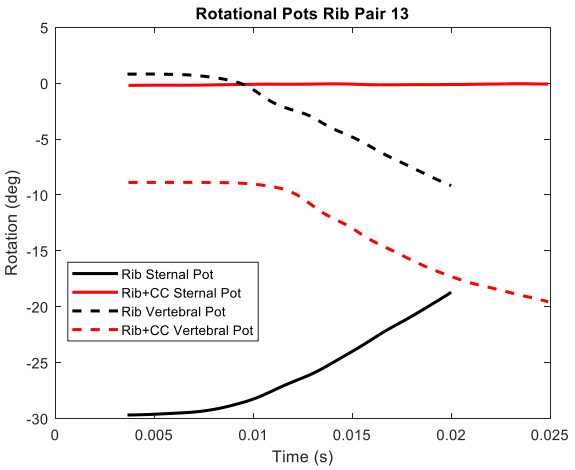

Figure D13. Pair 13 Pot Rotations

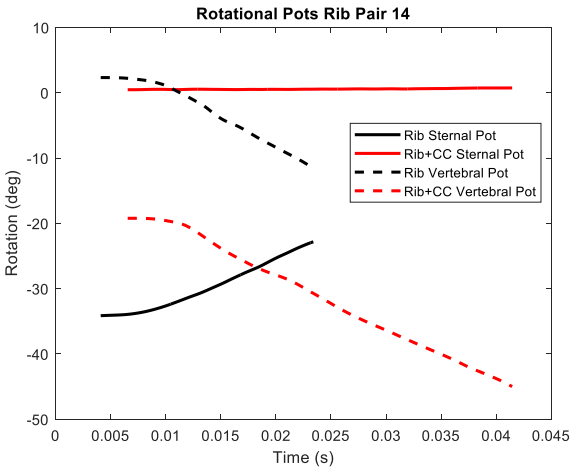

Figure D14. Pair 14 Pot Rotations

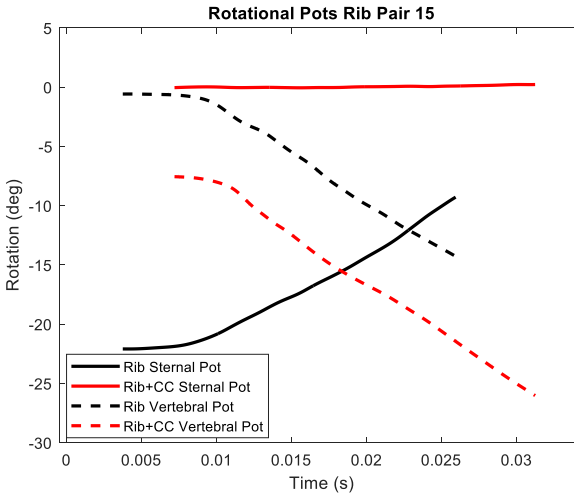

Figure D15. Pair 15 Pot Rotations

Appendix E. Strain data

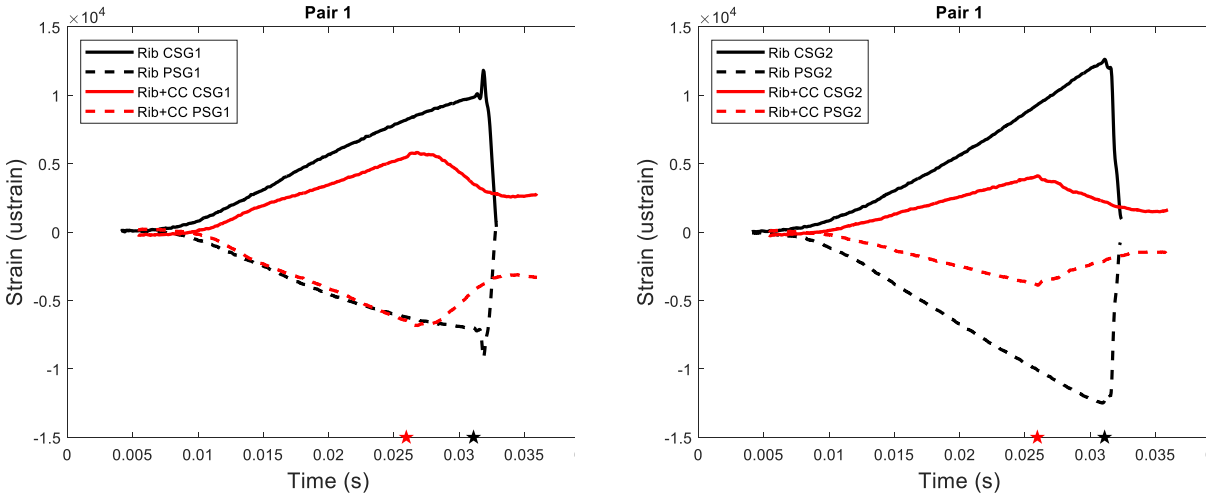

Figure E1. Pair 1 SG1 (left) and SG2 (right) strain-time histories. Stars indicate failure time for rib (black) and rib+CC (red).

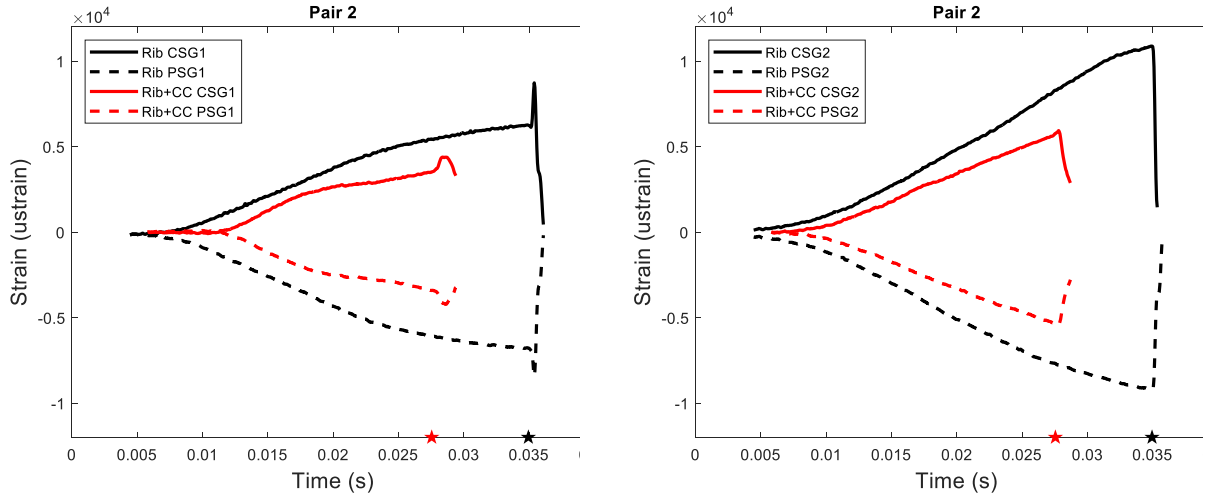

Figure E2. Pair 2 SG1 (left) and SG2 (right) strain-time histories. Stars indicate failure time for rib (black) and rib+CC (red).

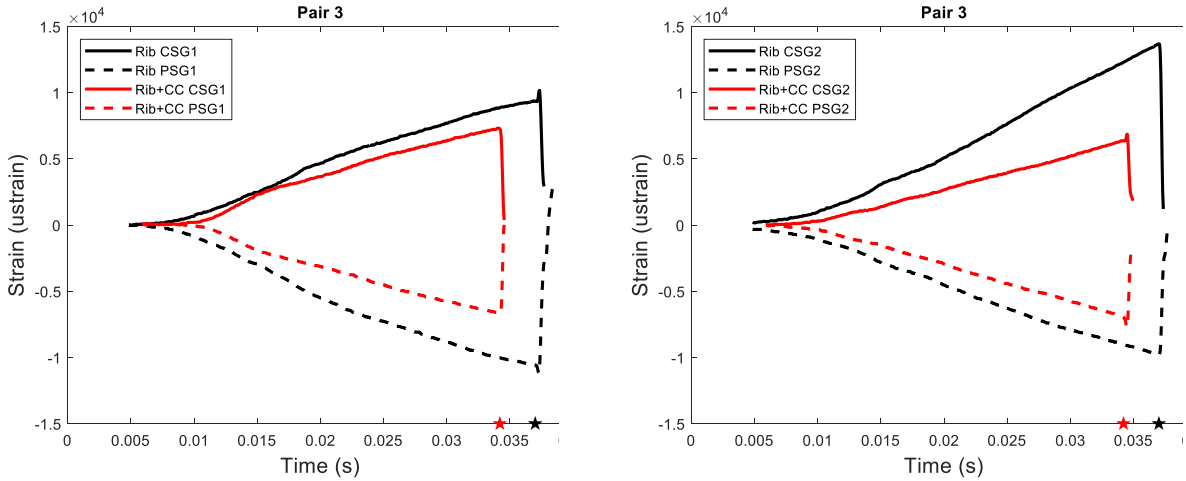

Figure E3. Pair 3 SG1 (left) and SG2 (right) strain-time histories. Stars indicate failure time for rib (black) and rib+CC (red).

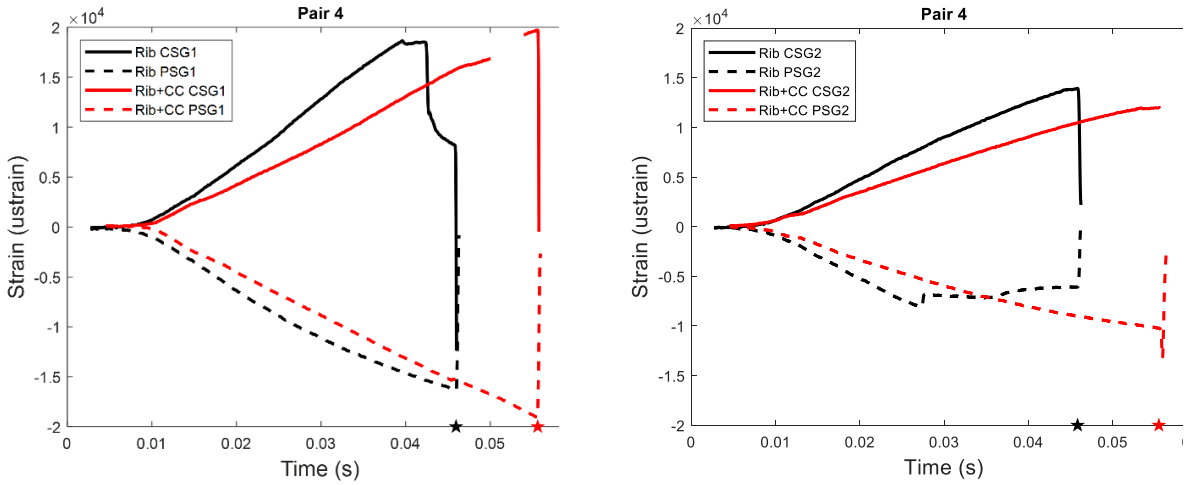

Figure E4. Pair 4 SG1 (left) and SG2 (right) strain-time histories. Stars indicate failure time for rib (black) and rib+CC (red).

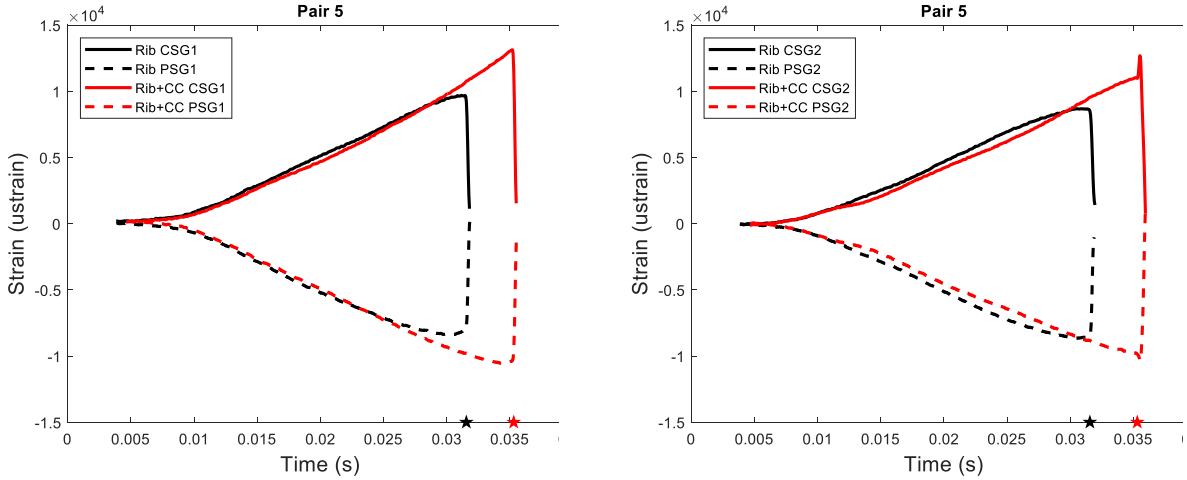

Figure E5. Pair 5 SG1 (left) and SG2 (right) strain-time histories. Stars indicate failure time for rib (black) and rib+CC (red).

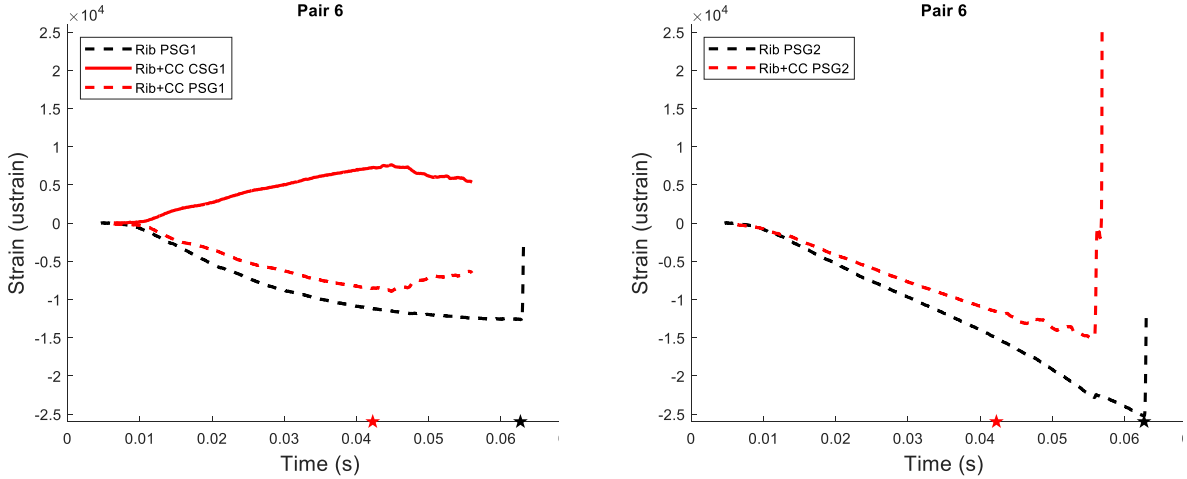

Figure E6. Pair 6 SG1 (left) and SG2 (right) strain-time histories. Stars indicate failure time for rib (black) and rib+CC (red).

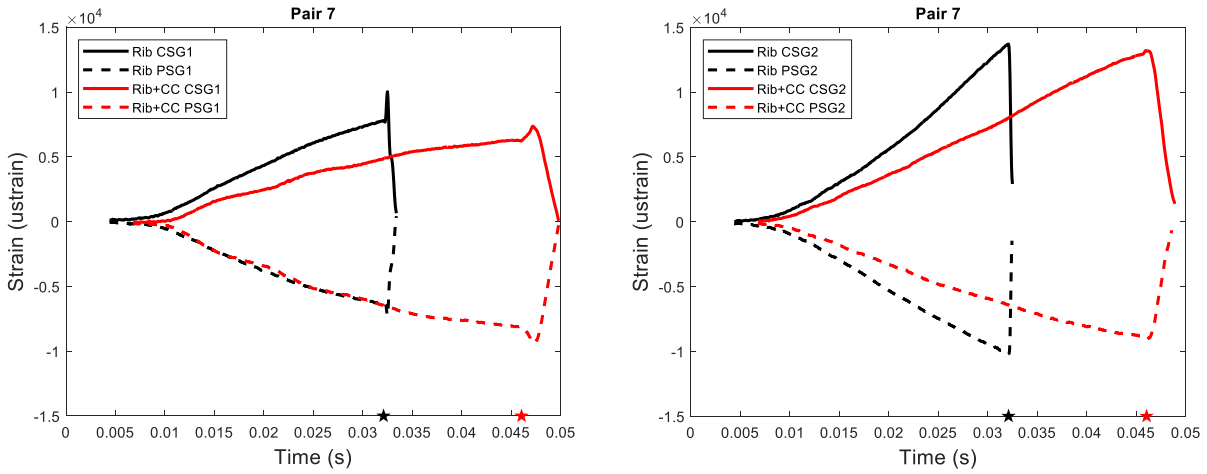

Figure E7. Pair 7 SG1 (left) and SG2 (right) strain-time histories. Stars indicate failure time for rib (black) and rib+CC (red).

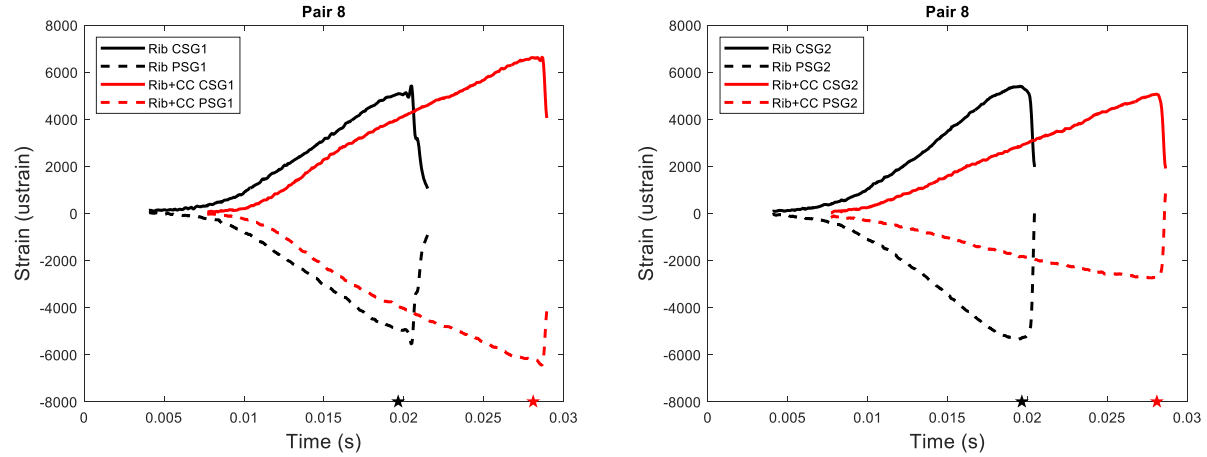

Figure E8. Pair 8 SG1 (left) and SG2 (right) strain-time histories. Stars indicate failure time for rib (black) and rib+CC (red).

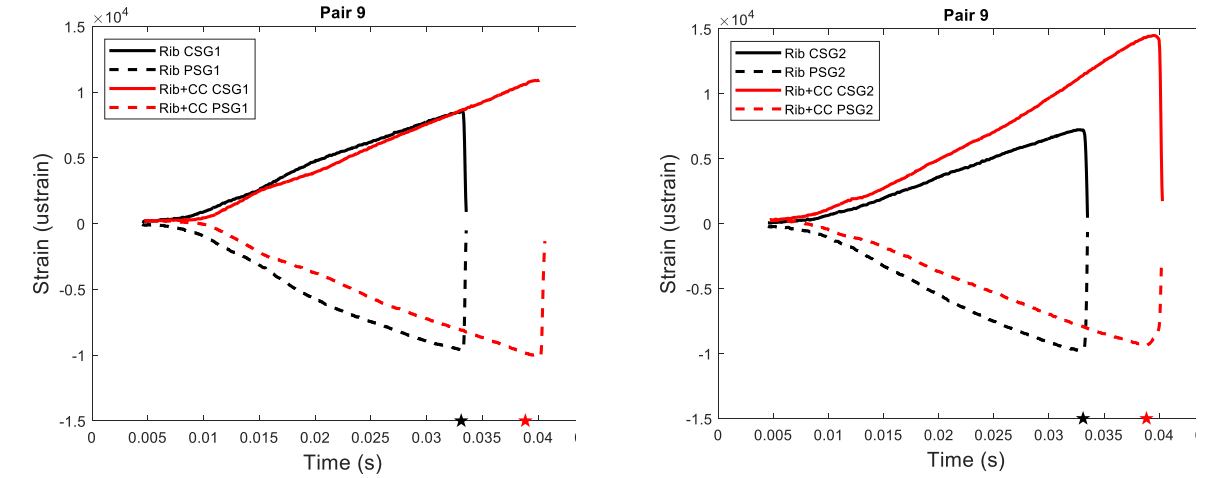

Figure E9. Pair 9 SG1 (left) and SG2 (right) strain-time histories. Stars indicate failure time for rib (black) and rib+CC (red).

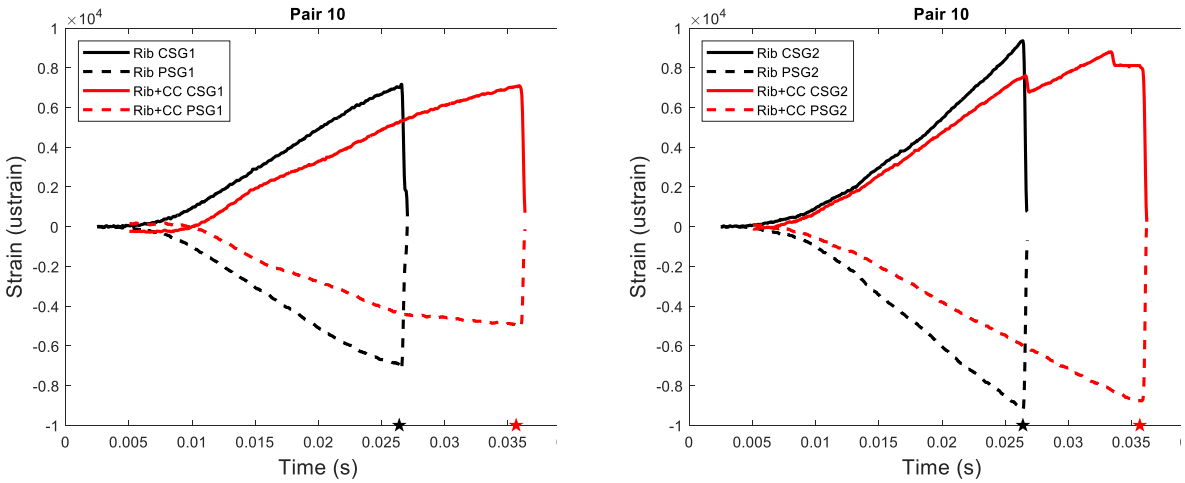

Figure E10. Pair 10 SG1 (left) and SG2 (right) strain-time histories. Stars indicate failure time for rib (black) and rib+CC (red)

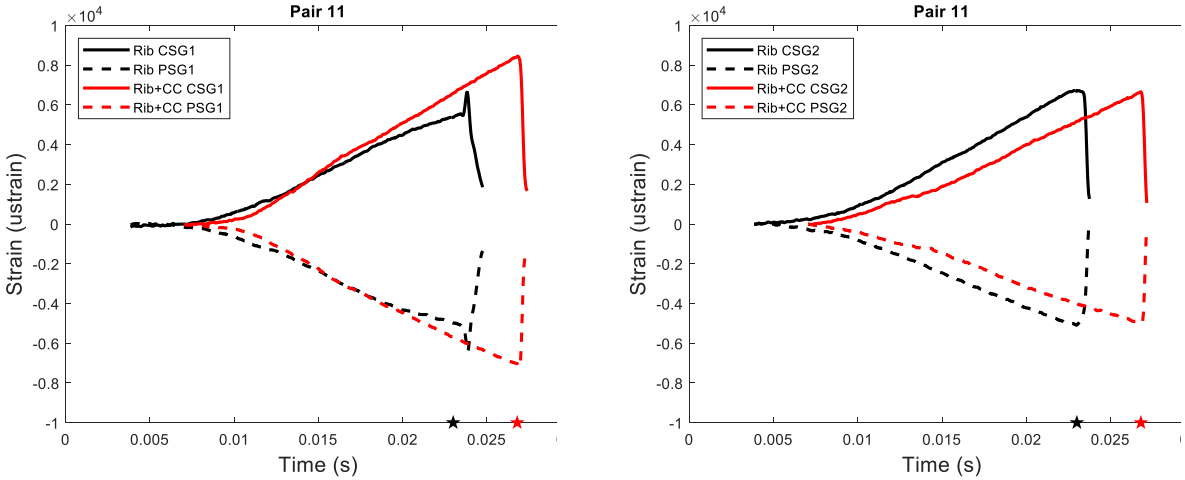

Figure E11. Pair 11 SG1 (left) and SG2 (right) strain-time histories. Stars indicate failure time for rib (black) and rib+CC (red)

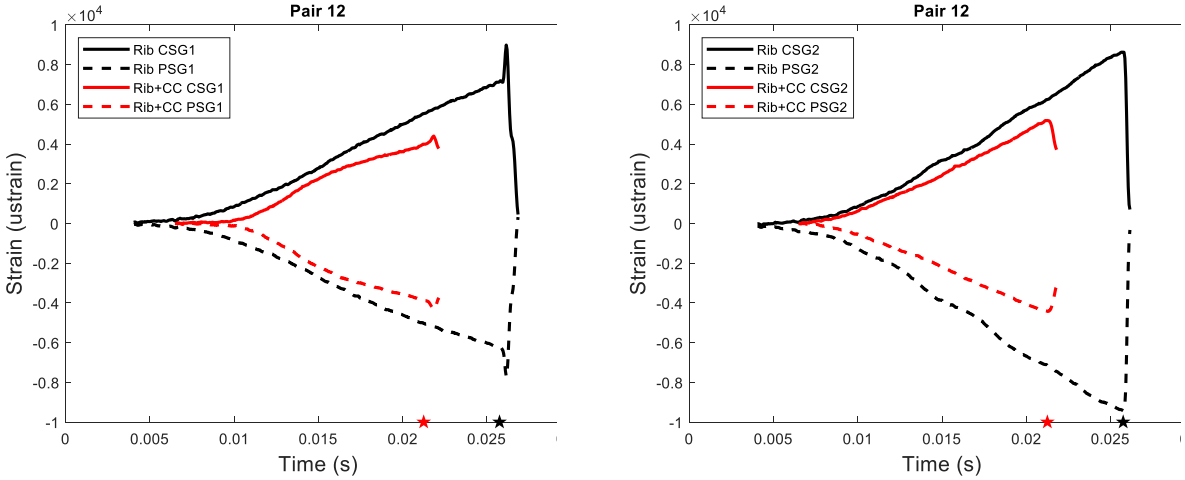

Figure E12. Pair 12 SG1 (left) and SG2 (right) strain-time histories. Stars indicate failure time for rib (black) and rib+CC (red)

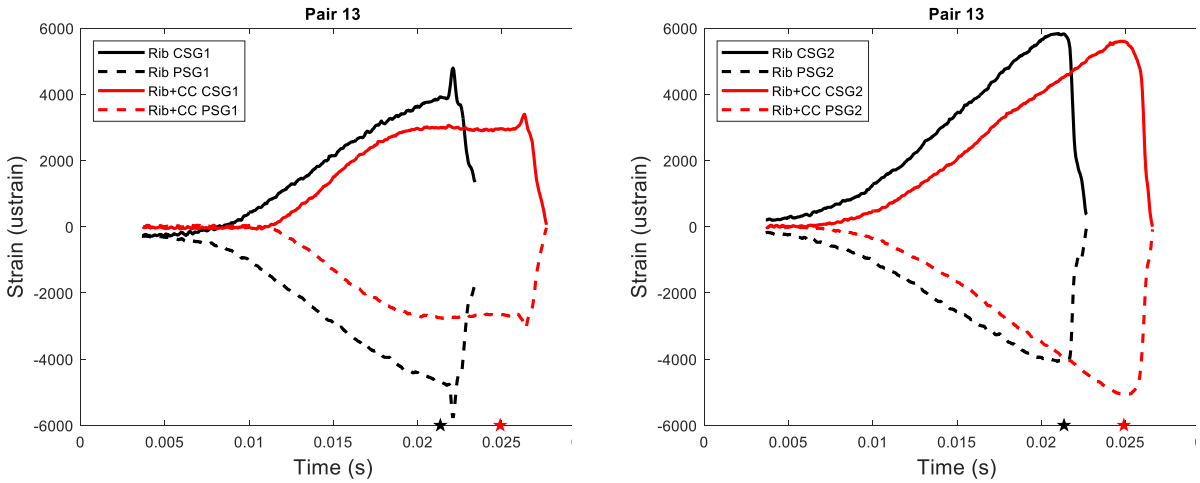

Figure E13. Pair 13 SG1 (left) and SG2 (right) strain-time histories. Stars indicate failure time for rib (black) and rib+CC (red)

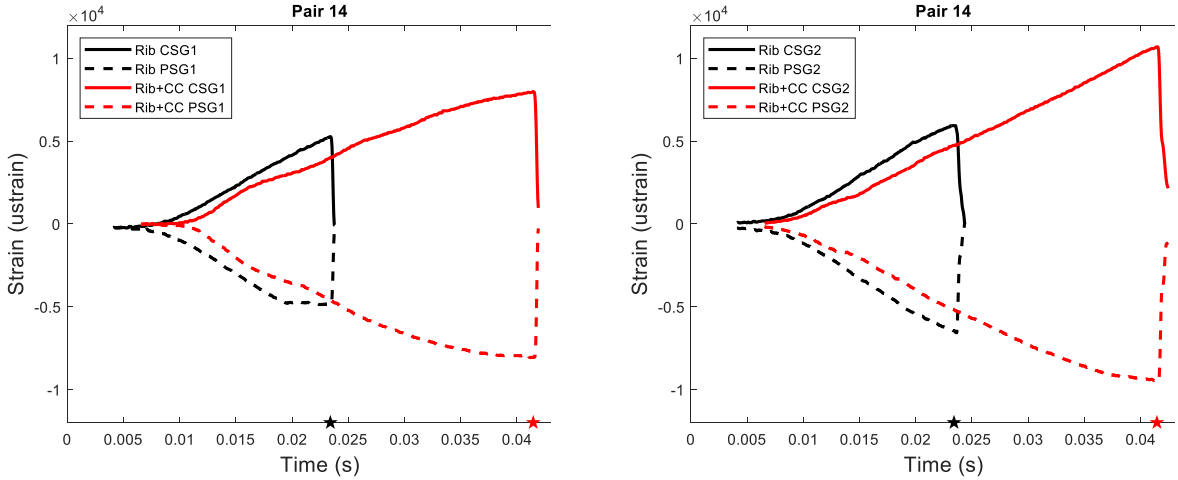

Figure E14. Pair 14 SG1 (left) and SG2 (right) strain-time histories. Stars indicate failure time for rib (black) and rib+CC (red)

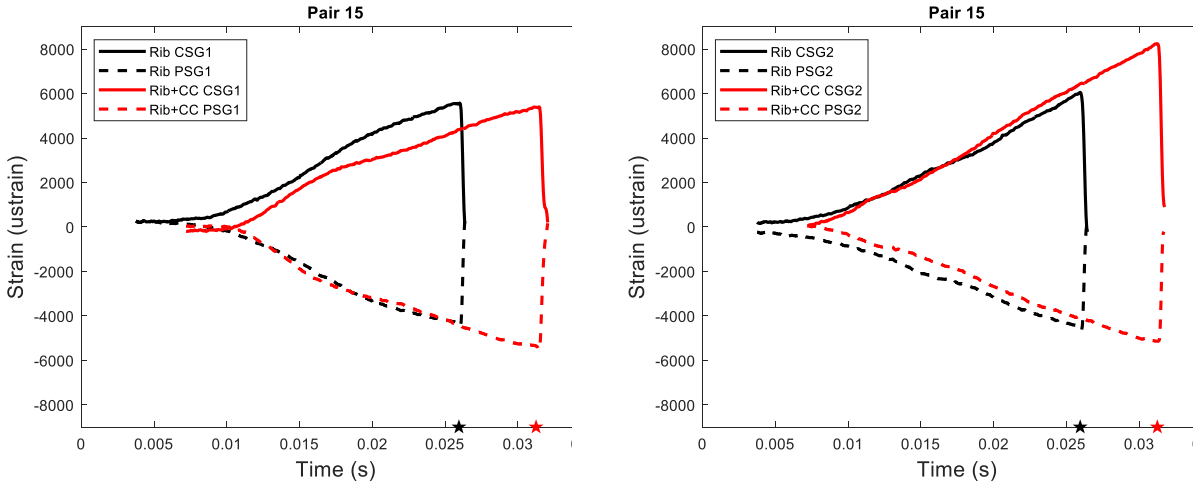

Figure E15. Pair 15 SG1 (left) and SG2 (right) strain-time histories. Stars indicate failure time for rib (black) and rib+CC (red)

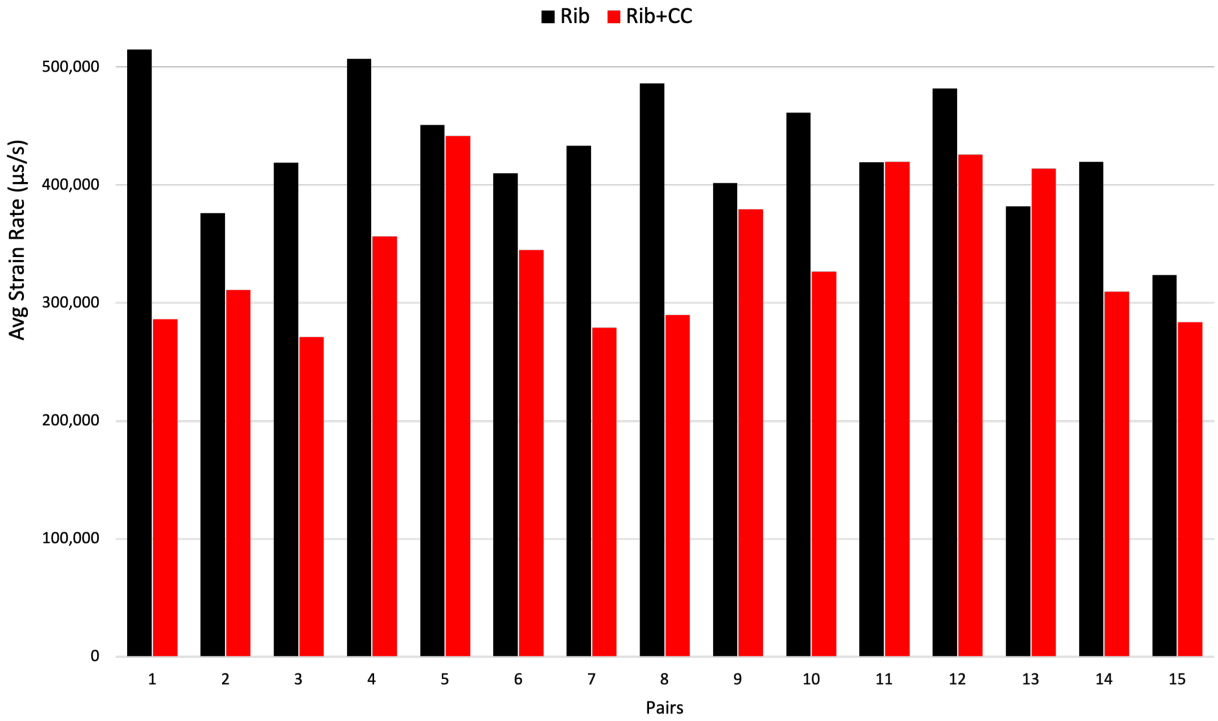

Figure E16. Average strain rate comparisons within pairs

Table E1. Strain Data for all 5th Rib Pairs

Pair ID	Rib Condition	CSG1 (με)		CSG2 (με)		PSG1 (με)		PSG2 (με)	
		Yield	Peak	Yield	Peak	Yield	Peak	Yield	Peak
1	Rib	4274	11834	4135	12639	-3461	-9163	-5066	-12487
	Rib+CC	5493	5826	4128	4128	-6439	-6826	-3870	-3887
2	Rib	4500	6263	5907	10876	-5098	-8408	-5976	-9192
	Rib+CC	1415	4385	1934	5936	-1299	-4227	-1834	-5454
3	Rib	7379	10177	9798	13688	-8501	-11173	-7629	-9790
	Rib+CC	3117	7326	2121	6870	-2651	-6678	-2355	-7710
4	Rib	4459	18668	3497	13931	-4738	-16372	-3884	-8115
	Rib+CC	3464	19720	2979	12003	-3698	-19044	-2859	-13177
5	Rib	6016	9689	5618	8686	-5950	-8389	-6020	-8648
	Rib+CC	7418	13141	6502	12695	-7508	-10552	-6610	-10351
6	Rib	*	*	*	*	-5875	-12833	-5932	-25257
	Rib+CC	1878	7279	*	*	-2454	-8561	-2544	-11805
7	Rib	2867	7797	3376	13711	-2482	-7250	-3339	-10212
	Rib+CC	2702	7356	4044	13208	-3783	-9388	-3664	-9068
8	Rib	5087	5407	5390	5402	-4867	-5551	-5280	-5346
	Rib+CC	1962	6634	1409	5061	-1946	-6451	-921	-2742
9	Rib	6526	8590	5440	7236	-7721	-9660	-7888	-9773
	Rib+CC	2718	10903	3072	14499	-2523	-10100	-2093	-9370
10	Rib	7012	7166	9366	9366	-6940	-7208	-9212	-9212
	Rib+CC	5726	7102	7168	8810	-4472	-5036	-6545	-8771
11	Rib	5370	6638	6687	6721	-4988	-6390	-5105	-5105
	Rib+CC	8448	8456	6666	6666	-7023	-7188	-4940	-4973
12	Rib	7137	8986	8625	8625	-6262	-7707	-9423	-9423
	Rib+CC	3993	4404	5187	5187	-3838	-4304	-4411	-4428
13	Rib	3647	4794	5649	5832	-4397	-5774	-3929	-4077
	Rib+CC	2996	3399	4211	5603	-2696	-3058	-3594	-5072
14	Rib	3137	5265	3794	5929	-3966	-4889	-4210	-6623
	Rib+CC	2374	7993	2511	10697	-2788	-8076	-2783	-9496
15	Rib	5557	5573	6057	6057	-4345	-4452	-4541	-4641
	Rib+CC	5386	5403	8242	8242	-5344	-5521	-5140	-5140

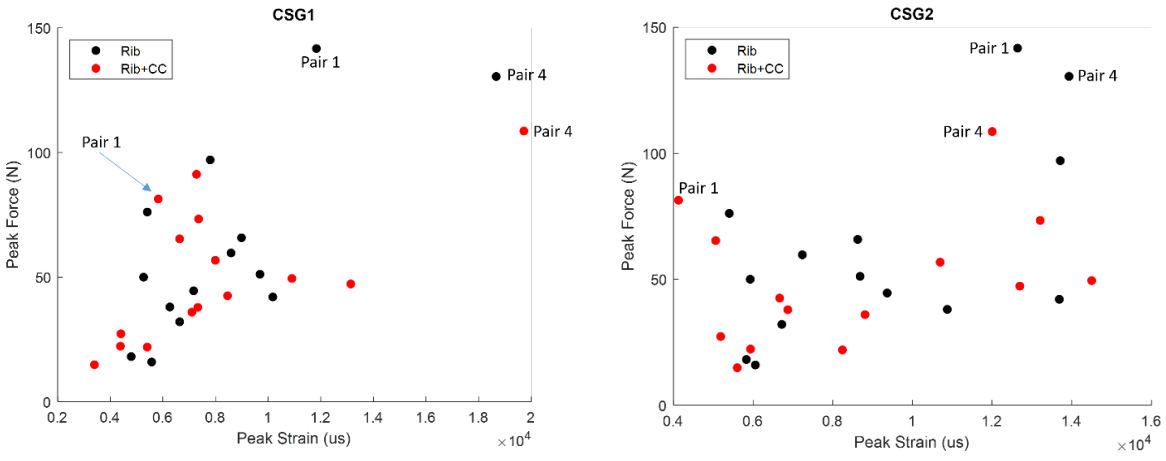

Figure E17. Peak strain versus peak force for all 15 pairs for CSG1 (left) and CSG2 (right) strain gages

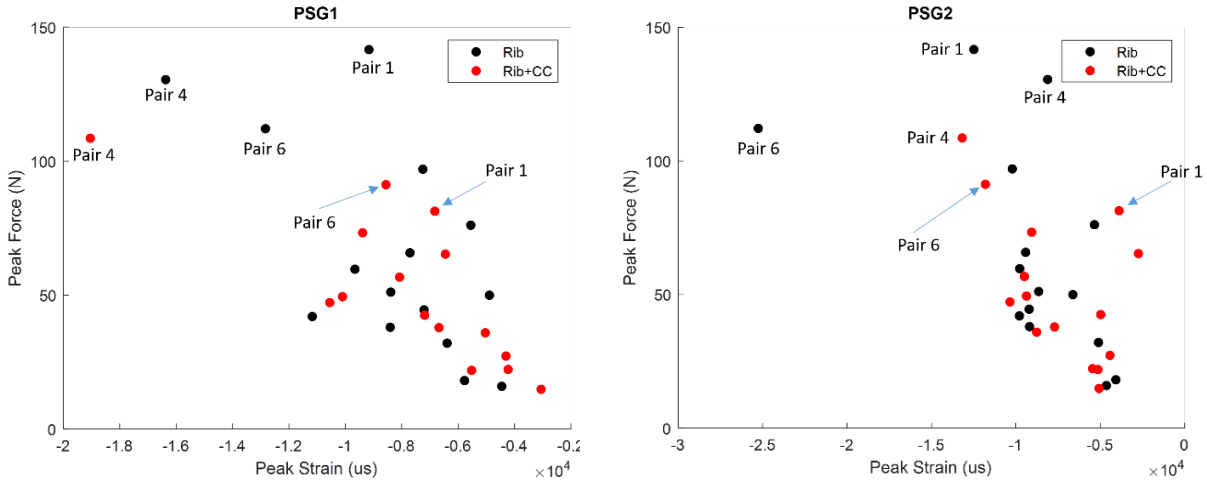

Figure E18. Peak strain versus peak force for all 15 pairs for PSG1 (left) and PSG2 (right) strain gages

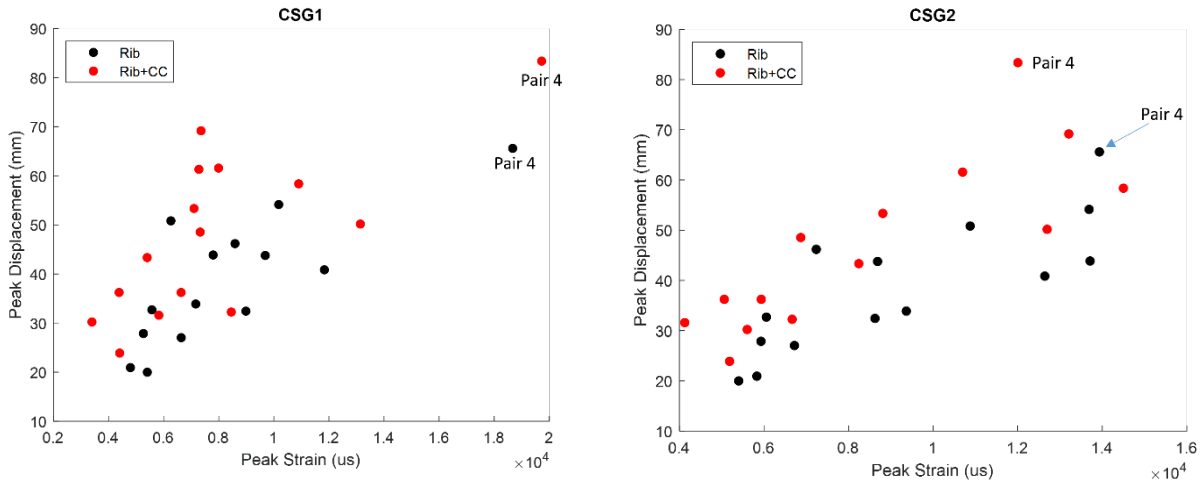

Figure E19. Peak strain versus peak displacement for all 15 pairs for CSG1 (left) and CSG2 (right) strain gages

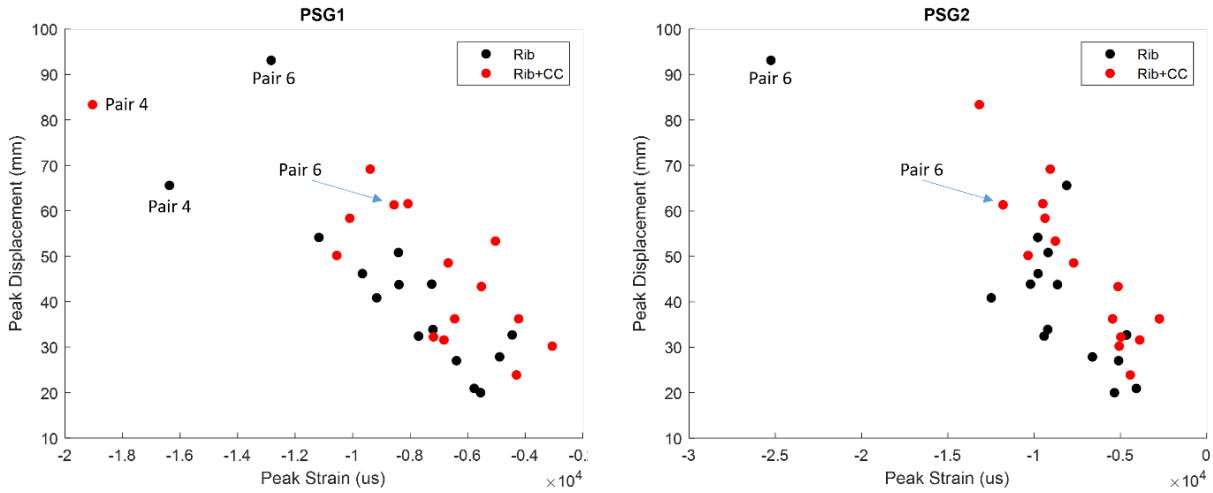

Figure E20. Peak strain versus peak displacement for all 15 pairs for PSG1 (left) and PSG2 (right) strain gages

Appendix F. Post-test Radiographs

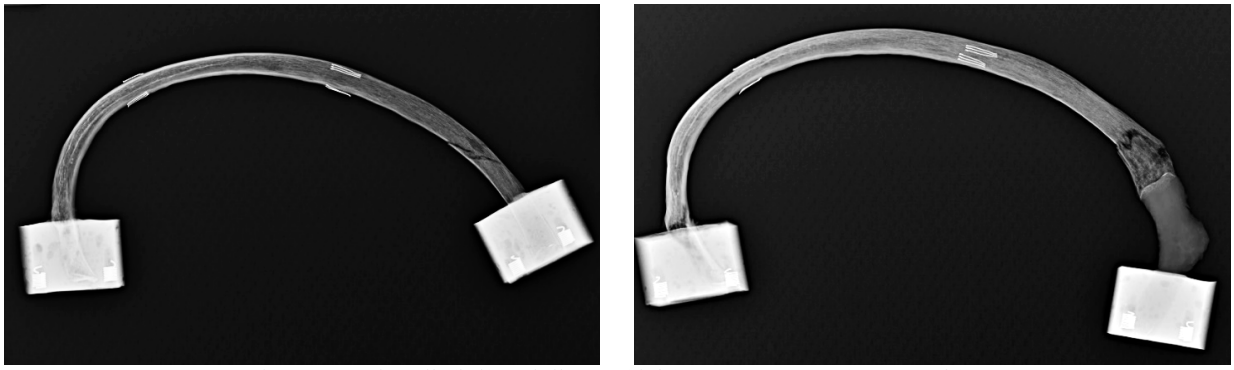

Figure F1. Pair 1 rib (left) and rib+CC (right) post-test x-rays (not to scale)

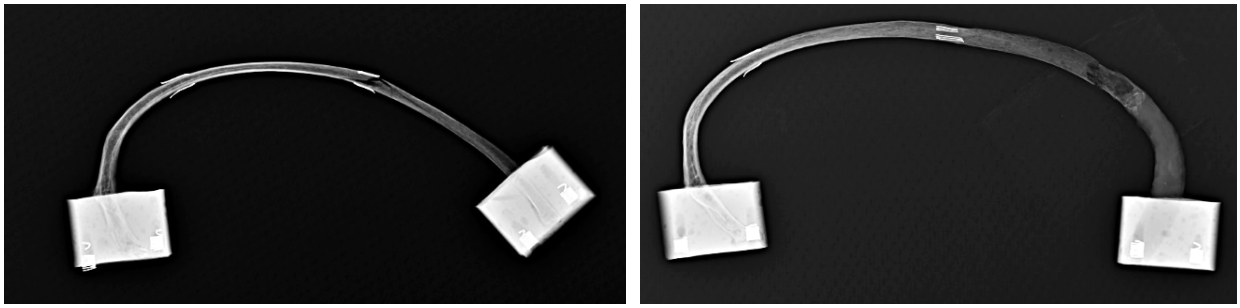

Figure F2. Pair 2 rib (left) and rib+CC (right) post-test x-rays (not to scale)

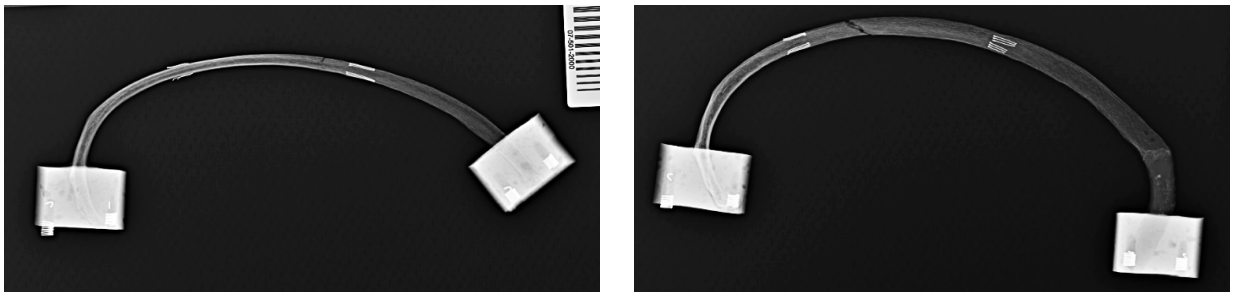

Figure F3. Pair 3 rib (left) and rib+CC (right) post-test x-rays (not to scale)

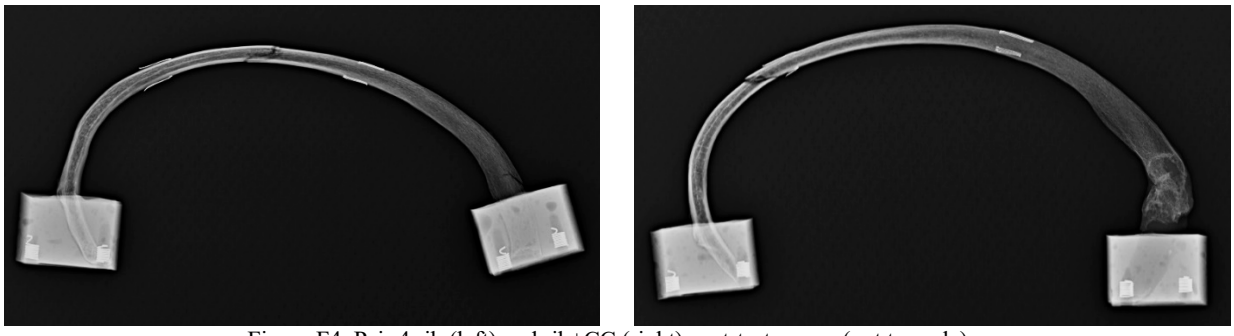

Figure F4. Pair 4 rib (left) and rib+CC (right) post-test x-rays (not to scale)

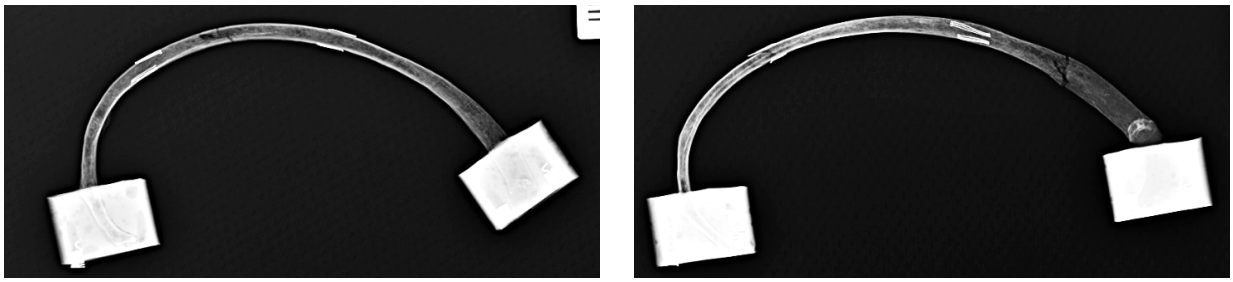

Figure F5. Pair 5 rib (left) and rib+CC (right) post-test x-rays (not to scale)

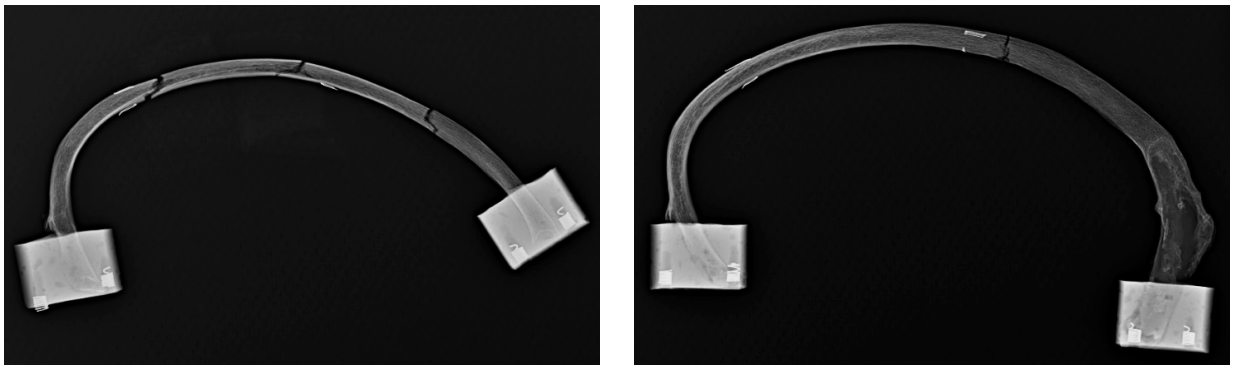

Figure F6. Pair 6 rib (left) and rib+CC (right) post-test x-rays (not to scale)

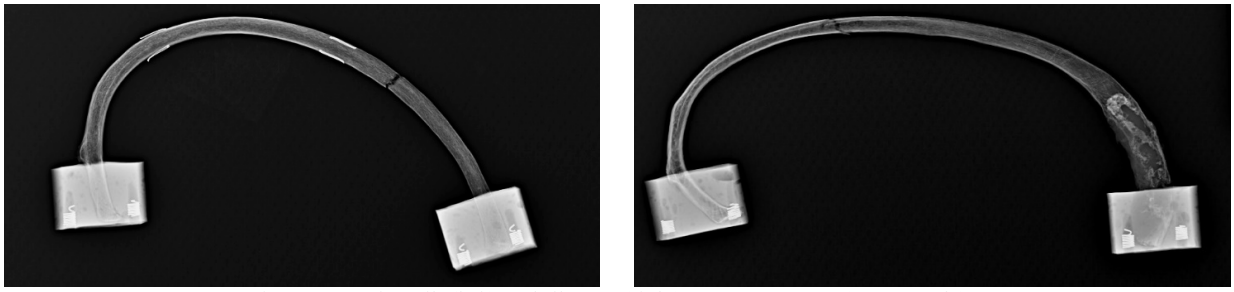

Figure F7. Pair 7 rib (left) and rib+CC (right) post-test x-rays (not to scale)

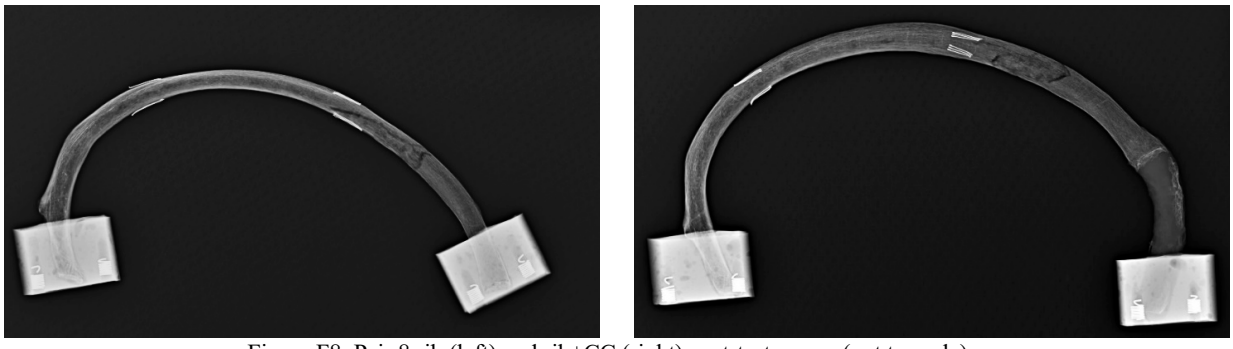

Figure F8. Pair 8 rib (left) and rib+CC (right) post-test x-rays (not to scale)

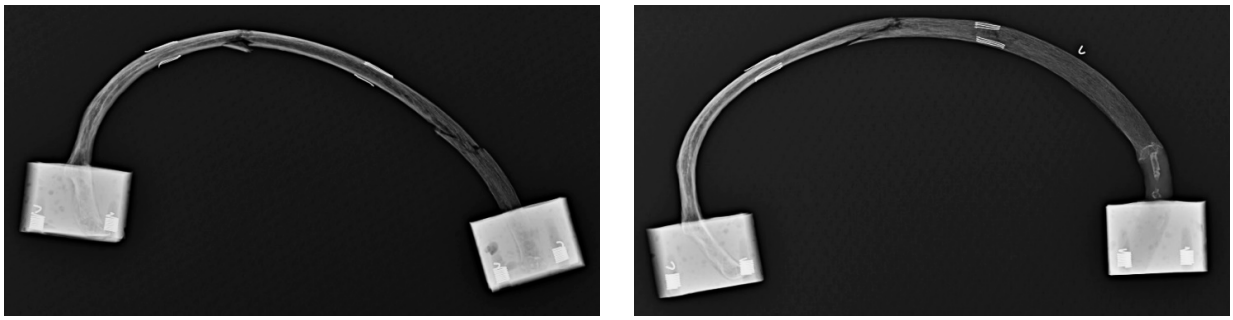

Figure F9. Pair 9 rib (left) and rib+CC (right) post-test x-rays (not to scale)

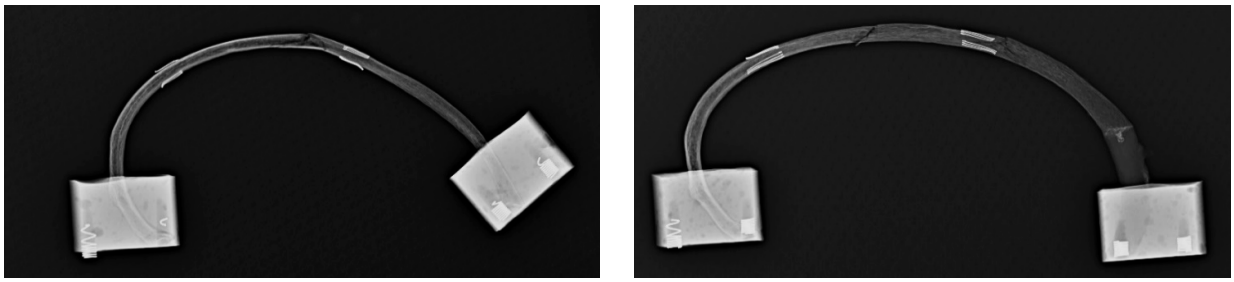

Figure F10. Pair 10 rib (left) and rib+CC (right) post-test x-rays (not to scale)

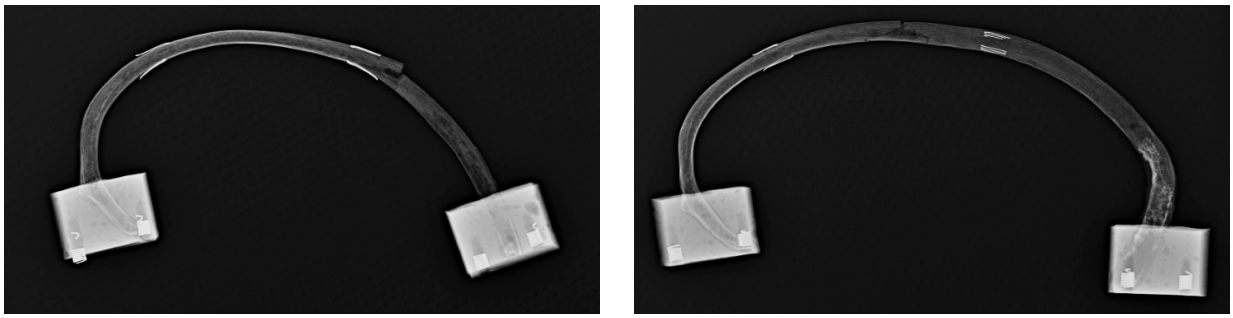

Figure F11. Pair 11 rib (left) and rib+CC (right) post-test x-rays (not to scale)

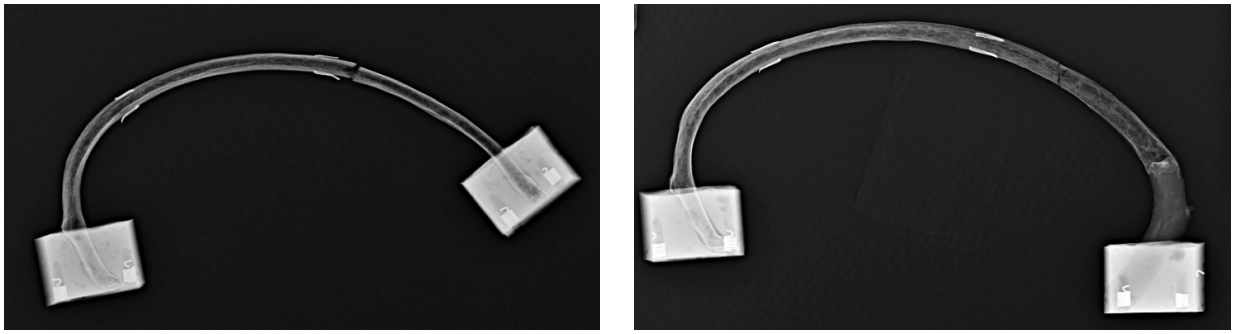

Figure F12. Pair 12 rib (left) and rib+CC (right) post-test x-rays (not to scale)

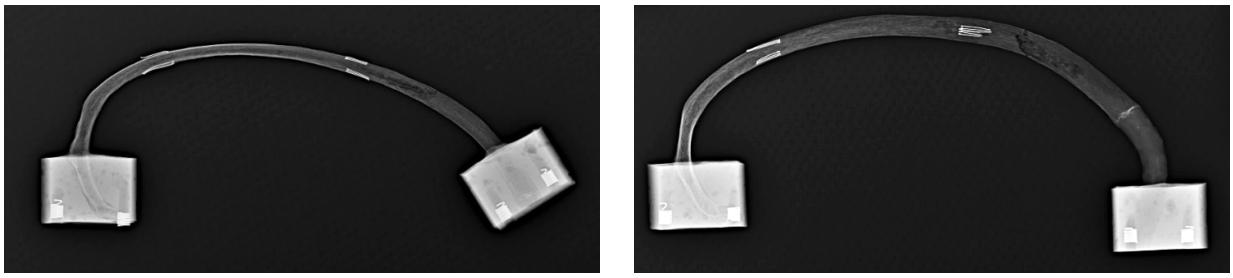

Figure F13. Pair 13 rib (left) and rib+CC (right) post-test x-rays (not to scale)

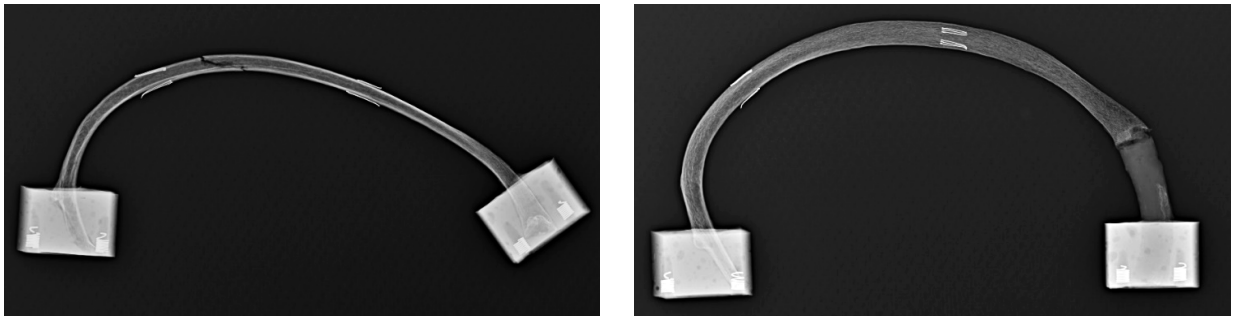

Figure F14. Pair 14 rib (left) and rib+CC (right) post-test x-rays (not to scale)

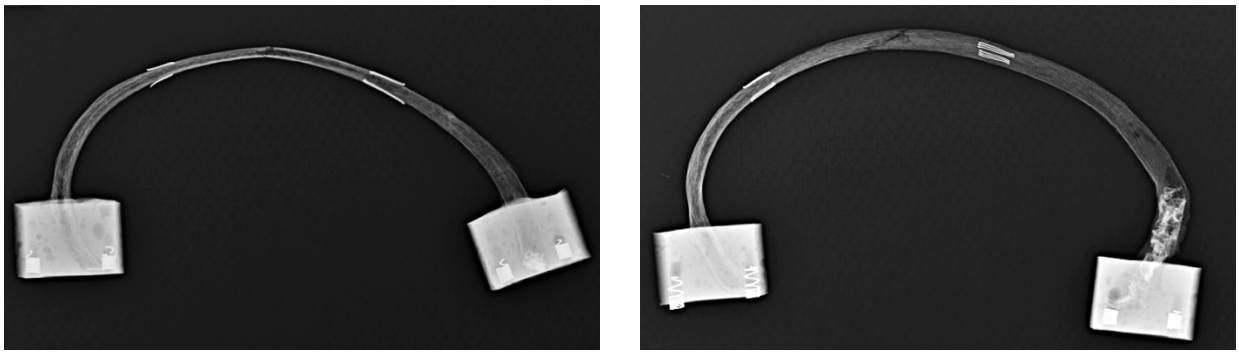

Figure F15. Pair 15 rib (left) and rib+CC (right) post-test x-rays (not to scale)